THE ROLE AND REGULATION OF AN ACTOMYOSIN COMPLEX IN MEMBRANE REMODELING DURING REGULATED EXOCYTOSIS IN A LIVE RODENT MODEL SYSTEM

by

OLEG MILBERG

A dissertation submitted to the

Graduate School-New Brunswick

Rutgers, The State University of New Jersey

In partial fulfillment of the requirements

For the degree of

Doctor of Philosophy

Graduate Program in Chemical & Biochemical Engineering.

Written under the direction of

Roberto Weigert

And approved by:

_____

_____

_____

_____

New Brunswick, New Jersey

October, 2015

ABSTRACT OF THE DISSERTATION

The Role and Regulation of an Actomyosin Complex in Membrane Remodeling During Regulated Exocytosis in a Live Rodent Model System

By OLEG MILBERG

Dissertation Director:

Dr. Roberto Weigert

Our lab has developed a subcellular imaging technique based on intravital microscopy (IVM) to study the highly conserved process of regulated exocytosis, as it occurs in live rodents, using the submandibular salivary glands (SSGs) as a model system for exocrine secretion. Previous work, mainly done on rats and commercially available transgenic and wild-type mice, determined that an actomyosin complex, composed of F-actin and nonmuscle myosin II (NMII) isoforms A and B (NMIIA and NMIIB, respectively), forms around single secretory granules that have fused with the apical plasma membrane (APM) following β-adrenergic stimulation of regulated exocytosis. This complex is required to promote the full integration of the granules into the APM, and although the role of F-actin in regulating granule integration was established, the roles and regulation of NMIIA and NMIIB in this process were not determined, and therefore, they are the main topics discussed in this thesis.

To this end, a series of tools, which includes 1) NMII floxed mice, 2) transgenic and knock-in mice, 3) transgene delivery and expression by viral and non-viral means, and 4) various pharmacological inhibition approaches, were developed. This thesis work

shows that: 1) both NMII isoforms are required for granule integration to occur, with NMIIA regulating the dynamics of the fusion pore and NMIIB stabilizing the granules and providing the necessary force for their gradual integration; 2) both NMII isoforms are recruited onto the granules in an F-actin independent manner and subsequently activated by the phosphorylation of their regulatory light chains by myosin light chain kinase (MLCK); and 3) MLCK is recruited through the GTPase Septin 2, and possibly other members of the septin family (Septins 6, 7 and 9) in an F-actin dependent manner. Live imaging by IVM provided further details on the kinetics and dynamics of actomyosin complex assembly and function, which lead to a mechanistic model of actomyosin activity in membrane remodeling during regulated exocytosis in the SSGs. This work is the first to describe how the actomyosin complex functions in a live rodent during a normal physiological process.

ACKNOWLEDGEMENTS

Here, I would like to thank several people who have played a major part in supporting me during my time in graduate school, as I pursued my interest in scientific research and have come to the completion of my PhD. Without them, I wouldn't be where I am today.

Namely, I would like to thank my committee: Drs. Barth Grant, Julie Donaldson, Stavroula Sofou, Charlie Roth and Martin Yarmush. Your support and insight during the past several years has been very helpful in guiding me in the right direction, as I progressed through graduate school. In particular, I also appreciate how quickly my emails were responded to. It has really made communicating over long distances less of a challenge.

Next, I would like to thank my research advisor, Dr. Roberto Weigert. By working in your lab, I have gained a great understanding of how to independently conduct biomedical research; including how to ask insightful questions, develop projects that stem from an initial curiosity and how to search for the answers to those questions. In addition, I've had the opportunity to work with many great people in your lab and within the OPCB branch who have been helpful in teaching me new techniques that I've applied in my research.

Lastly, I'd like to thank my friends and family for their great support over these years.

TABLE OF CONTENTS

LIST OF TABLES

LIST OF ILLUSTRATIONS

INTRODUCTION

Intracellular membranes involved in protein trafficking undergo continuous changes in their shape and composition. This remodeling is carried out by a combination of mechanical forces exerted by proteins directly onto the membranes, and modifications in the compositions of the lipid bilayers. The modifications are generated by lipid-modifying enzymes, or selective modulation of lipids by vesicular or non-vesicular transport. In recent years, efforts to unravel the molecular machinery controlling membrane remodeling during clathrin-mediated endocytosis have led to the identification of an integrated cascade of molecular events, including those involved in phospholipid metabolism [1], sensing, generating and maintaining curvature by BAR domain containing proteins [2], the assembly of a clathrin coat [3], fission factors, such as the small GTPase dynamin and associated cofactors [4], and the actin cytoskeleton [5].

On the other hand, membrane remodeling during regulated exocytosis has not been investigated in such great detail. In this thesis, I look at two main aspects related to membrane remodeling during regulated exocytosis: 1) how the structural and mechanical components of the actin cytoskeleton regulate the integration of fused secretory vesicles into the plasma membrane during regulated exocytosis in the exocrine glands of live rodents, and 2) how the mechanical activity of the actin cytoskeleton is regulated during this process. By addressing these aspects we will gain a better understanding of 1) the biophysical and biological aspects of membrane remodeling and protein secretion, as they occur in live animals, and 2) how the actin cytoskeleton functions *in vivo*, which has largely been unexplored and is different from how it functions in *in vitro* and *ex vivo* model

systems.

This introduction will begin with an overview of regulated exocytosis and the actin cytoskeleton. I will then introduce the submandibular salivary glands (SSGs) as an exocrine gland model system to study the actin cytoskeleton during regulated exocytosis, using a set of unique techniques that were developed in our lab for this purpose, and are based on intravital microscopy (IVM). Lastly, the main hypotheses of this thesis will be discussed in detail, focusing on understanding the roles and regulation of two essential mechanoenzymes and their interactions with F-actin during protein secretion.

1. Regulated exocytosis and its regulation by the actin cytoskeleton

1.1. Regulated exocytosis

Exocytosis is a fundamental process that every cell utilizes to deliver molecules (e.g. lipids, proteins, hormones) to the plasma membrane (PM) and the extracellular space by means of membranous carriers of different shapes and sizes (e.g., vesicles, tubules, or pleomorphic structures) [6]. There are two main types of exocytosis: 1) constitutive exocytosis, which occurs continuously in all cells in order to carry out basic cellular functions, including maintenance of the PM, and the release of some extracellular molecules (e.g., plasma proteins, antibodies, ECM components, etc.) [7]; and regulated exocytosis, which, on the other hand, occurs upon stimulation in specialized secretory cells for the purposes of carrying-out specific physiological and pathophysiological processes,

including wound healing, cancer cell metastasis, migration and invasion, neurotransmission, salivation, respiration, digestion, reproduction, and others [8-11].

1.1.1. Origin and delivery of secretory carriers to the plasma membrane

Proteins destined for secretion are synthesized in the ER, transported to the Golgi apparatus, modified and sorted into membranous carriers that are constitutively released from the trans-Golgi network and make their way to various intracellular destinations, including the cell periphery. Regulated exocytosis of the carriers can be initiated through stimulation of either heterotrimeric GTPases, such as G protein-coupled receptors (or GPCRs), tyrosine kinase receptors, or voltage-dependent calcium channels on the plasma membrane [12-14]. Stimulation may lead to two main signaling pathways: the first, which involves the generation of cAMP by adenylate cyclase-mediated conversion of ATP, and the second, which requires the opening of intracellular Ca^{2+} channels on the ER and/or at the PM. In several secretory systems, Ca^{2+} is the main trigger for exocytosis, whereas cAMP is usually, but not always, the assisting or regulating second messenger [15-17].

Once exocytosis is triggered, the membranous carriers undergo the following sequential steps: tethering/docking, priming, and fusion with the PM [8] (Fig. 1). This is then followed by one of three types of post-fusion modalities: full fusion, kiss-and run, or compound exocytosis [18-21]. During tethering, the membranous carriers become anchored to the PM at the sites of fusion by an evolutionarily conserved octameric protein complex called the exocyst [22, 23]. The exocyst also mediates the assembly of the SNARE (soluble NSF adaptor protein receptors, or SNAP receptors) proteins during the docking

step, which brings the membranous carriers closer to the PM [23]. Docking involves the interaction and partial assembly of the SNAREs into the *trans* state [24]. After that, carriers are primed into a readily-releasable state, as the SNAREs partially transition towards a *cis* confirmation, in order to promote rapid fusion with the PM [25].

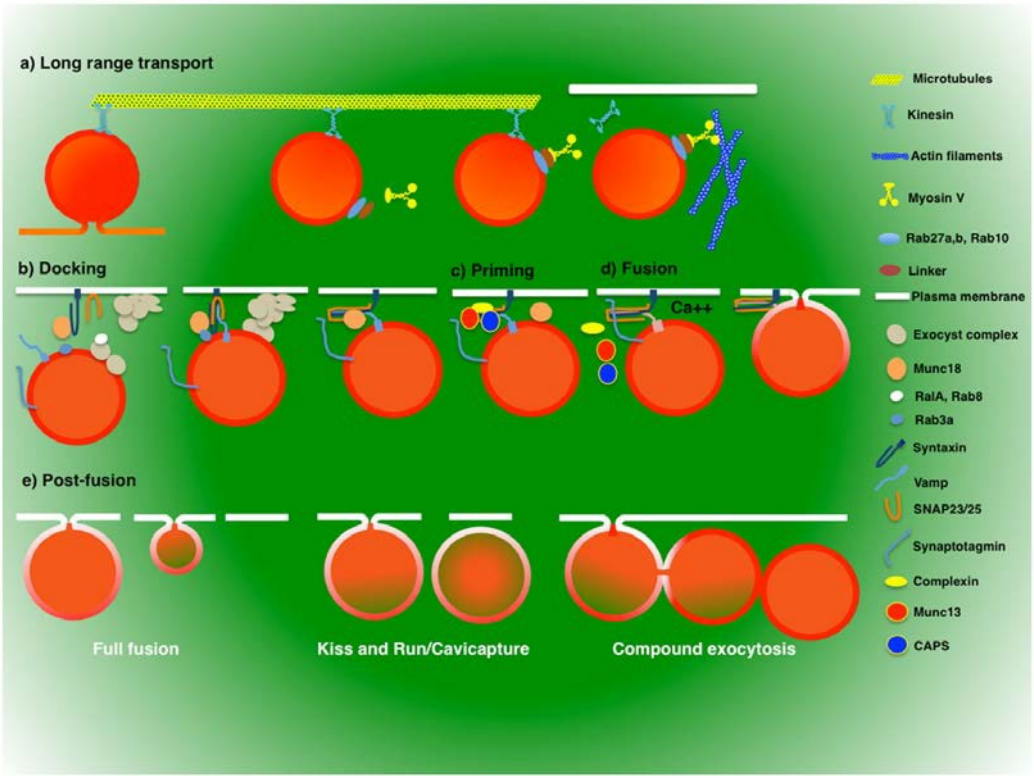

Figure 1. Steps during exocytosis. a) Secretory granules are transported the cell periphery on microtubules and are then guided to the PM by the cortical actin cytoskeleton. **b)** Upon stimulation of regulated exocytosis, secretory granules undergo tethering/docking, **c)** priming and **d)** fusion with PM, which is then followed by one of three post-fusion modalities: **e)** full fusion, kiss and run, or compound exocytosis. Illustration from, [8].

1.1.2. SNARE proteins mediate fusion events at the plasma membrane

SNAREs were originally identified as synaptic proteins that were the proteolytic targets for clostridial neurotoxins, which blocked neurotransmission [26]. Since then, multiple studies have determined that these proteins are essential components of all intracellular membrane pre- and post-fusion events, including secretory granule docking and priming [8, 18-23, 25-27].

SNAREs are classified according to either their localization, or the structure of their unique SNARE domain, which is essential for their activity. Specifically, they are classified as v-SNAREs (vesicular), if they are present on the transport intermediate, or t-SNAREs (target) if they are present on the target membranes [28]. In order to have a productive fusion, SNAREs have to form complexes in which four SNARE domains have to closely interact. Three of the SNARE domains have to be localized on the target membranes and they must contain a glutamine (Q SNAREs), whereas the remaining one has to be localized on the transport intermediate and must contain an arginine residue (R SNARE) [28].

During regulated exocytosis, one Q SNARE domain is provided by a member of the Syntaxin family of SNAREs (e.g. Syntaxin 2 or 3), whereas the other two domains are provided by one of the members of the SNAP family (SNAP-23 or SNAP-25) [28]. Members of the VAMP/Synaptobrevin family provide the R SNARE domain (VAMP2 or VAMP8) [28]. The initial interactions between the Q and the R domains occur between juxtaposing bilayers (*trans* conformation) at their N-terminal portions [29]. This interaction rapidly propagates towards the C-terminal ends of the SNARE domains

aligning them in a parallel bundle (zippering), which bring the membranes close enough to initiate the bilayer fusion [29] (Fig. 2). Once the membranes are fused, the SNARE complex is in an inactive state (*cis* conformation) and requires the action of the NSF/α-SNAP complex to reactivate it, so that it can be available for the next round of fusion [30].

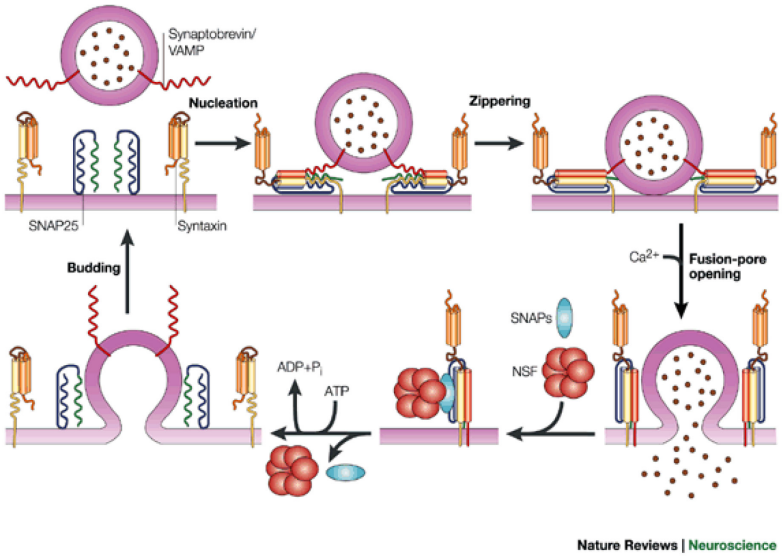

Figure 2. SNARE zippering, fusion, disassembly of the SNARE complex and compensatory endocytosis. The Q and R SNAREs during exocytosis come into contact with one another and undergo zippering in a *trans* conformation, to bring the granule and PM into close enough apposition for fusion to occur. As fusion occurs, the SNAREs switch to a *cis* conformation. Following fusion, they are regenerated by the NSF/α-SNAP complex and prepared for another round of fusion. Compensatory endocytosis then retrieves the excess membranes and proteins to maintain PM homeostasis. Illustration from, [31].

1.1.3. Fusion pore: formation and regulation

As fusion occurs between the bilayers of the carrier and the PM, it first goes through an initial hemi-fusion state, followed by a fully fused state that is defined by the formation of a small fusion pore about 1-2 nm in diameter, and in some studies it has even been reported to be as small as 0.5 nm or possibly smaller [32-34]. The fusion pore connects the lumen of the secretory carrier with the extracellular environment and permits cargo molecules to be fully released outside of the cell, and for the membranous carrier to integrate into the PM [35]. As the fusion pore forms, it flickers rapidly between an open and a closed state (full fusion and hemi-fusion, respectively) until it is either stabilized and maintained in an irreversible open state from which it may expand, or it closes, at which point integration of the carrier into the PM is halted [34-38] (Fig. 3). Furthermore, if the fusion pore closes, the carrier may detach from the PM (kiss-and run) [35]. As discussed later, this may be regulated by the actin cytoskeleton and its associated components [8, 39-45].

Little is known about the structure of the fusion pore and some studies suggest it to be purely protein-based (like an ion channel), or formed by lipids surrounded by a protein scaffold (such as an F-actin based scaffold) [36, 46]. The structure of the fusion pore may also be a combination of the two extremes. Interestingly**,** recent work has revealed that SNAREs, along with other exocytic machineries play an active role in the expansion and maintenance of the fusion pore and thus, the modality by which exocytosis occurs [45, 47] (Fig. 4).

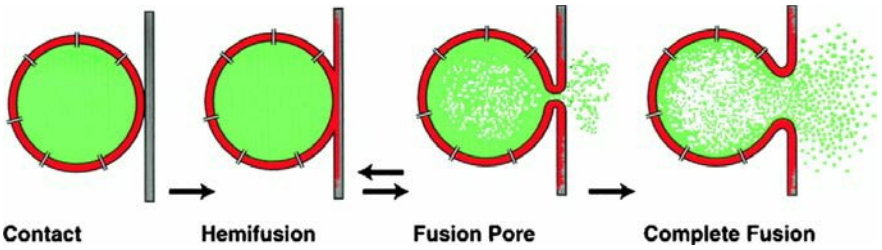

Figure 3. Fusion pore flickering between full- and hemi-fusion. Membranes of the granule and the PM come into contact during the fusion process. First, a hemi-fusion state occurs, followed by the opening of a small fusion pore. Flickering occurs between the hemi-fusion and fully fused state, until the fusion pore either closes (kiss and run), or expands to an irreversible state (leading to complete fusion). Illustration from, [38].

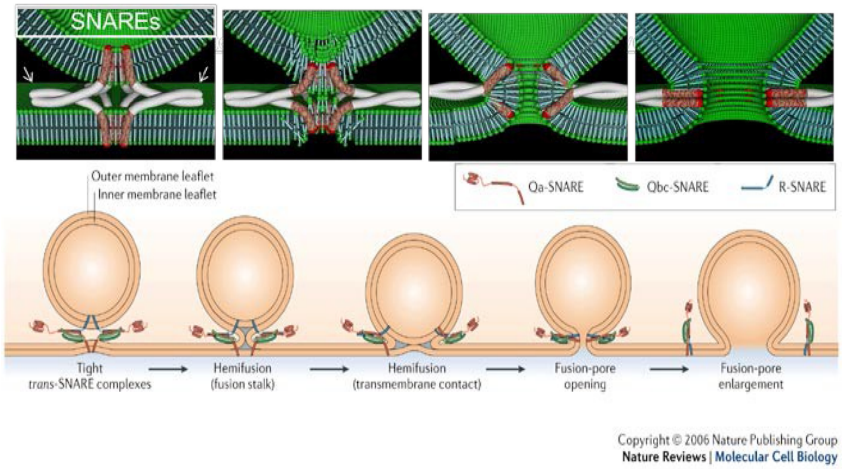

Figure 4. The fusion pore and its regulation by the SNARE complex. *trans*-SNARE complexes bring the membranes of the granule and the PM together as they transition to a *cis* conformation in order to drive full fusion. Along the way, they determine the modality of fusion, including the extent of fusion pore opening and expansion. Top illustration from, [48]. Bottom illustration from, [47].

1.1.4. Post-fusion modalities of regulated exocytosis

As previously mentioned, after fusion, exocytosis can proceed by three different modalities: 1) full fusion in which the individual secretory vesicles integrate into the PM and release their cargo into the extracellular space one at a time; 2) compound exocytosis, in which secretory vesicles at the cell periphery fuse on top of already fused vesicles, forming strings of fused membranes; and finally, 3) kiss-and-run exocytosis, in which the fusion pore of a fused vesicle closes, leading to its detachment from the PM, followed by its subsequent trafficking into the cell. During kiss-and-run, lumenal cargo proteins are believed to be only partially released, and the majority of the lipids and transmembrane proteins in the vesicles do not to integrate into the PM [19, 21].

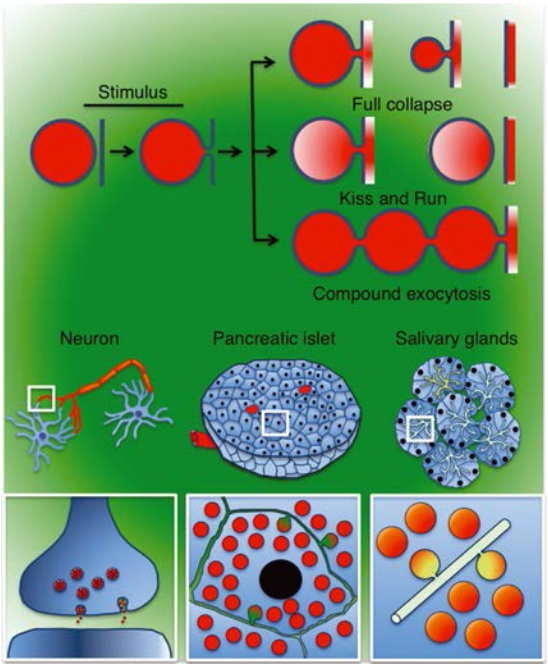

Figure 5. Post-fusion modalities of exocytosis differ among the secretory organs depending on their physiological needs and biophysical properties. Following a stimulus, secretory granules can undergo one of three different types of exocytosis: 1) full

collapse (or integration) with the apical plasma membrane (APM), 2) kiss and run, or 3) compound exocytosis. Full fusion involves full release of cargo proteins, while cargo proteins are only partially released in a quantal manner during kiss and run. As mentioned previously, the post-fusion modality is regulated by the SNAREs and associated machinery that is responsible for maintaining and expanding the fusion pore. The regulation of this process, and thus the modality of regulated exocytosis differs among the various secretory organs, including neurons (left), endocrine (middle) and exocrine (right) organs. Illustration from, [49].

The modality of exocytosis depends on the secretory organ in which it's occurring, and hence on its physiological needs [8, 49] (Fig. 5). In essence, the morphological and biophysical properties of the membranes of the secretory vesicles and the PM in each secretory tissue, the nature of their cargo molecules, and the external influences on the cells are believed to define the modality of exocytosis. For example, neurons have to rapidly transmit signals throughout the whole body by releasing neurotransmitters from their axon terminals into the synaptic clefts through which the molecules travel to reach the post-synaptic neurons; they primarily contain small vesicles and granules that range in size from ~50-200 nm in diameter, which exocytose on the order of hundreds of milliseconds [8]. In endocrine cells, molecules destined for secretion are released at the basolateral PM into the extracellular space, and diffuse through the stroma to reach the bloodstream; secretory carriers are larger in diameter (300-500 nm) and complete exocytosis in a matter of a few seconds [8]. Finally, in exocrine glands, molecules are secreted at specialized domains of the PM, usually at the apical poles, into a fluid mixture that flows through a ductal system

to the outside of the body [8]. The exocrine glands contain large secretory vesicles (1-5 µm in diameter) termed secretory granules, which contain large macromolecular complexes and the duration of exocytosis is on the order of tens of seconds to minutes [8] (Fig. 6). Interestingly, much of the same molecular machinery (i.e. SNARE proteins and the actin cytoskeleton) is conserved among all of these processes [8, 50].

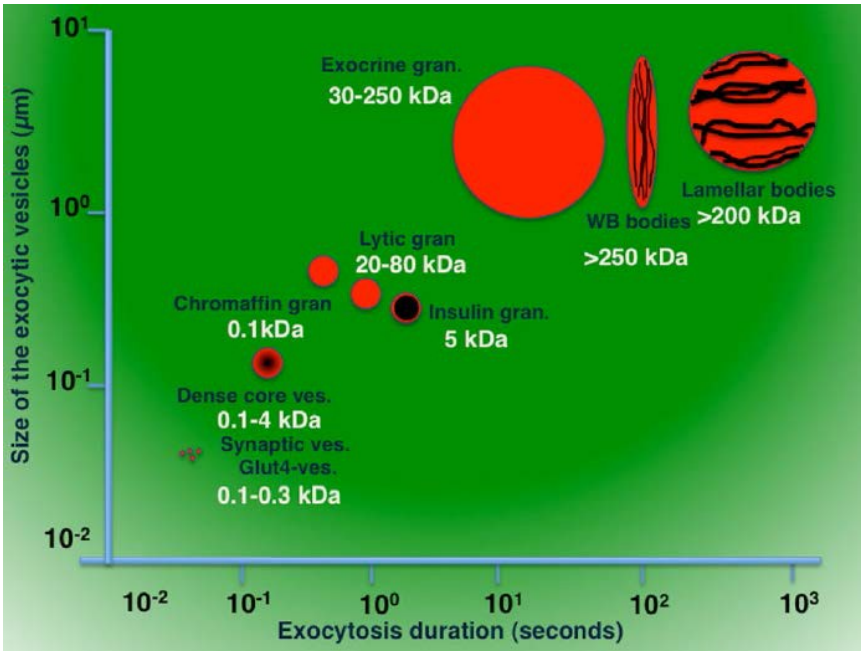

Figure 6. Correlation between secretory vesicle size and duration of exocytosis. Secretory vesicles (and granules) range in diameter from 50 nm to 2-3 µm, which roughly correlates with the molecular weights of their cargo molecules (0.1 kDa to great than 200kDa). This is inversely correlated with the duration of exocytosis, which occurs as required in each secretory organ. Interestingly, much of the same machinery, including the SNAREs, is involved in regulating exocytosis in all the various secretory organs. Illustration from, [8].

Finally, since PM homeostasis has to be maintained, the membranes of the secretory granules need to be retrieved. Indeed, it was shown that right after the integration of the granular membrane, a process called compensatory endocytosis is immediately activated [51]. It has been estimated that 50-75 small endocytic vesicles (100-200 nm in diameter) are used to retrieve the membrane of an individual granule [52-54]. The molecular machinery regulating this process is still poorly understood.

1.2. The role of the actin cytoskeleton in regulated exocytosis

The actin cytoskeleton, and its associated machinery, has been extensively studied during the process of regulated exocytosis. It is known that in endocrine and neuroendocrine cells F-actin acts as a functional barrier to prevent the premature fusion of the exocytic vesicles, but it may also play other roles in regulating the post-fusion integration of the vesicles into the PM [55-57]. In exocrine cells, its role has been shown to be far more complex. Numerous studies using the exocrine pancreas, lacrimal and salivary glands have indicated that the actin cytoskeleton can play two distinct regulatory roles: 1) acting as a barrier and 2) promoting the post-fusion integration of the secretory granules into the PM, as further discussed [8, 13, 58].

In addition, two actin-based motor proteins, non-muscle myosin II isoforms A and B (NMIIA and NMIIB, respectively), have been found to associate with F-actin on the fused secretory granules in the SSGs of live rodents; thus, suggesting that mechanical activity through the application of force by an actomyosin contractile complex is required for secretory granule exocytosis [13]. Interestingly, pharmacological inhibition of NMII

motor activity by Blebbistatin resulted in a change in the morphology of the secretory granules post-fusion, and a small delay in the kinetics of integration into the APMs of a small sub-population of the fused granules [13]. This partial effect could have been the result of a low effective concentration of the inhibitor in the acinar cells due to either poor tissue penetration of the drug, or to its rapid cellular (e.g. through ABC transporters) and tissue (e.g. through the lymphatic system) clearance. Thus, further experimentation is required in order to determine the roles of NMIIA and NMIIB during secretory granule exocytosis in the salivary glands. It should be noted that an actomyosin complex was also observed to be recruited around fused secretory granules in the acinar cells of the exocrine pancreas and the lacrimal glands *in vivo* (unpublished results); indicating that the actomyosin complex plays a more universal role in the exocrine glands.

2. Experimental model systems to study regulated exocytosis

In vitro, *ex vivo* and *in vivo* model systems have been used to study regulated exocytosis and the actin cytoskeleton in a variety of cell types. Each of these systems has their own advantages and disadvantages, including the number of experimental techniques available to study exocytosis, and how comparable the results are between the model systems. Regulated exocytosis has been reported to occur by different modalities depending on the model system, and this also translates to differences in how the actin cytoskeleton is regulated and regulates exocytosis. Clearly, the ultimate question is, how is the actin cytoskeleton regulated and how does it regulate protein secretion in a

physiologically relevant environment? Here we compare the different types of model systems used to study regulated exocytosis and discuss the advantages of using a live rodent model system.

2.1. *In vitro* and *ex vivo* model systems

Exocytosis has been primarily studied in two-dimensional (2D) cell cultures *in vitro*, and in a variety of *ex vivo* preparations. Endocrine, neuroendocrine, and neuronal cells, such as, chromaffin cells, PC12 cells, immune cells, pancreatic beta cells, endothelial cells, and primary cultured hippocampal neurons have been used to investigate the secretion of a wide variety of molecules *in vitro* [59-65]. Studies of exocrine secretion have relied primarily on acinar, ductal or lobule preparations derived from explanted organs (*ex vivo*) via mechanical and/or enzymatic procedures [59, 66-71]. Among them, the most widely used are preparations from the salivary glands, pancreas, and lacrimal glands.

Precise control over experimental conditions, the availability of established pharmacological and genetic manipulation techniques, as well as a wide range of assays based on electron and light microscopy, immunological inhibition, electrophysiology and biochemistry confer great advantages to studying regulated exocytosis in established *in vitro* and *ex vivo* model systems. However, there are several concerns regarding how translatable the results from these model systems are to how cells function in the body. 2D cell cultures lack three-dimensional (3D) architecture and interactions with other cells, the extracellular matrix (ECM), and with many associated signaling molecules. Furthermore, many of these cells lose their polarity, specialization, and membrane organization when

isolated from their native tissues; and this is well correlated with significant differences in their protein and gene expression profiles, secretion amounts and metabolic states when compared to how they occur *in vivo* [49, 72]. In addition, *ex vivo* preparations lack the continuous contributions from signaling molecules, which come from the vasculature and the nervous system, and have been shown to influence how cells respond to excitatory stimuli [8, 49].

As examples, secretory granules in the exocrine pancreas and the SSGs were seen to integrate by compound exocytosis in *ex vivo* experiments, sometimes with contradicting results [73, 74]. Notably, it has been clearly shown that only single granule exocytosis occurs *in vivo*, in at least the pancreas and the salivary glands of live rodents [13, 49]. Furthermore, other experiments have shown that, in the SSGs, stimulation of the β–adrenergic receptor triggers regulated exocytosis *in vivo*, while the muscarinic receptor is strictly involved in water secretion. This is in contrast to findings in *ex vivo* model systems where both the muscarinic and β–adrenergic receptors have been found to trigger exocytosis: a discrepancy that may be attributed to differences in gene expression and the perturbation of the signaling pathways [75-77]. Consistent with this hypothesis, denervation of salivary tissues has been reported to produce alterations in the exocytic capacity and morphology of the secretory apparatus in several studies [13, 49].

2.2. *In vivo* exocrine model system: Submandibular salivary glands of live rodents

As a result of these differences between *in vivo* and reductionist model systems, we began to study the roles and regulation of the actin cytoskeleton during regulated

exocytosis *in vivo*, using the SSGs of live rodents as a model of exocrine secretion. The salivary glands are exocrine organs that secrete saliva into the oral cavity. Saliva is a hypotonic mixture of water, electrolytes (sodium, potassium, calcium, chloride, magnesium, bicarbonate, phosphate), and proteins (digestive enzymes, immunoglobulins, antimicrobial peptides, mucosal glycoproteins) of importance to oral health, digestion, and tissue repair [78]. Mammals have three major salivary glands: the parotid, which secretes digestive enzymes (e.g. amylase); the submandibular, which secretes antimicrobial molecules (e.g. peroxidases, lysozyme) and mucins; and the sublingual, which secretes mucins (Fig. 7). In addition, the minor salivary glands are distributed on the gingival and anterior hard palate and throughout the submucosa of the oral cavity, and the majority of them secrete mucins, with the exception of Von Ebner's glands, which are serous in nature (e.g., secreting IgA) [78].

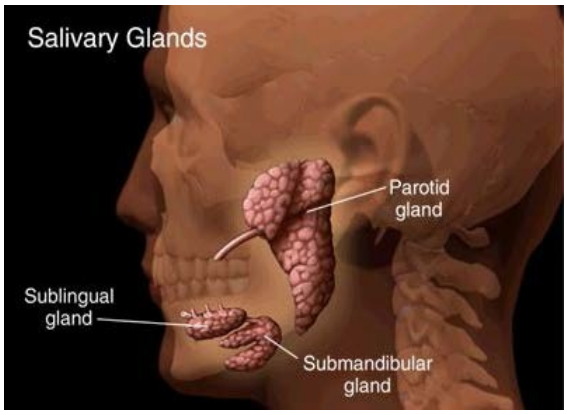

Figure 7. The major salivary glands. Locations of the major salivary glands described above are depicted on the image of a human head. We specifically focus on studying the role of the actin cytoskeleton during the regulated exocytosis of secretory granules in the submandibular salivary glands in live rodents, which are also located by the ventral neck area in front of the trachea. Image from, http://www.oral-cancer.info/?cat=1.

2.2.1. Anatomy of the submandibular salivary glands

In rodents, there are two SSGs that are located directly underneath the ventral neck area, one on each side of the trachea. Each gland consists of an overall surrounding collagen capsule (~15μm thick) and beneath it a serious of lobules. Each lobule contains smaller lobules composed of multiple acinar structures and a ductal system that connects them to the main excretory duct, called Wharton's Duct, which opens directly to the oral cavity underneath the tongue (Fig. 8 and 9).

In the rodent SSGs, the acini are the major protein and water secretory units of the glands, whereas the ducts secrete primarily electrolytes and, in a subset of specialized cells (granular convoluted tubules), also proteins [76]. Each acinus consists of 9-10 acinar epithelial cells arranged in a spherical cluster. Each acinar cell possesses serous or mucous protein-containing large membranous carriers, called secretory granules (~1.5μm in diameter), which are packed at the APM [13, 49]. The vasculature and the nervous system are in contact with the basolateral sides of the acinar cells, to which myoepithelial cells are also attached [78].

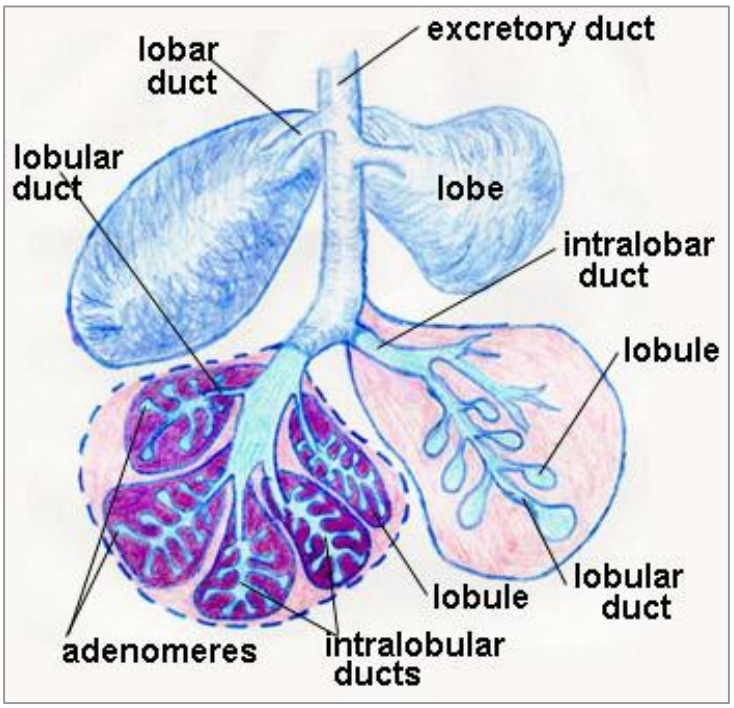

Figure 8. Structure of the submandibular salivary glands located beneath a collagen capsule. Within a collagen capsule, multiple lobes are attached to the main excretory duct. Within each lobe are lobules and a ductal system. Located within each lobule, the adenomeres contain the acini, which are the main secretory unit of the salivary glands. Each acini is composed of multiple (9-10) acinar cells. The secretions from the acinar cells flow through the ductal system and out into the oral cavity through the main excretory duct, called Wharton's Duct. Illustration from, http://www.snipview.com/q/Adenomere.

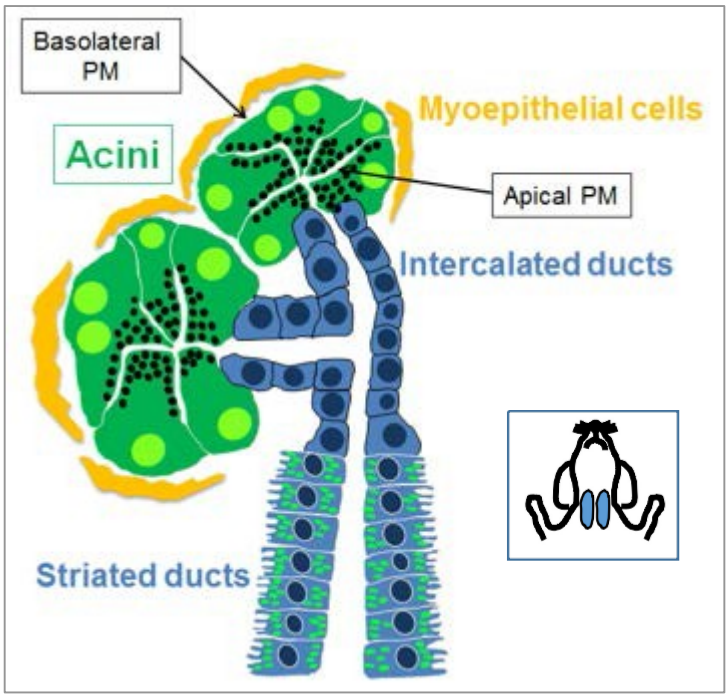

Figure 9. The structure of the functional units in each lobe of the SSGs. This includes the acini, surrounding myoepithelial cells, and the intralobular ducts, which lead to the main excretory duct (Wharton's Duct). The secretory granules are packed at the APM of each acinar cell and during regulated exocytosis their contents are secreted into the canaliculi, which are composed of the APMs of adjacent acinar cells, and are connected to the ducts. Bottom right: sketch of mouse SSGs (blue).

2.2.2. Physiology of the submandibular salivary glands

The SSGs are entirely regulated by the nervous system and upon stimulation of the appropriate G protein-coupled receptor (GPCR) on the basolateral side, the secretory granules undergo regulated exocytosis by fusing with the APM and releasing their contents into the canaliculi (~0.3-0.4 μm in diameter), which are formed by the APMs of adjacent cells, and are directly connected to the ductal system (Fig. 9). Under resting conditions, basal levels of water and protein secretion occur, and some of the proteins are secreted through a constitutive pathway that does not involve the large secretory granules [78, 79]; on the other hand, the majority of granules undergo regulated exocytosis. The acinar cells are also responsible for transcellular water and chloride (Cl-) secretion into the canaliculi which are the driving force for the paracellular sodium (Na+) and water secretion [78].

In vivo, the parasympathetic and sympathetic nerves of the autonomic nervous system stimulate salivation in complementary ways. Parasympathetic stimulation of the muscarinic receptor by either acetylcholine or vasoactive intestinal peptide promotes increased blood flow to the salivary glands and water and electrolyte secretion. However, the resulting saliva is low in protein content, as the parasympathetic nervous system has a minor effect on protein secretion from the acinar cells [80]. On the other hand, sympathetic stimulation of the β-adrenergic receptor by norepinephrine (also known as adrenaline), which induces vasoconstriction, is fully responsible for the stimulation of the exocytosis of proteins, and it plays a minor role in water and electrolyte secretion [80]. Notably, direct stimulation of the nerves has been shown to cause increases in salivary secretions over basal conditions [81].

Direct stimulation of the β-adrenergic receptor by a subcutaneous injection of Isoproterenol (ISOP, which is structurally similar to adrenaline) is used as a complementary method to stimulate regulated exocytosis *in vivo* [13]. The activation of the β-adrenergic receptor leads to an intracellular increase in cAMP and the activation of several of its downstream targets for regulated exocytosis, and the activation of some ion channels [82]. Interestingly, in the salivary glands the increase of intracellular Ca^{2+} *per se* is not sufficient to elicit regulated exocytosis, suggesting that, contrary to other systems, secretory granules are not in a primed state at the PM [83]. Thus, the muscarinic receptor is not involved in regulated exocytosis *in vivo* – only the β–adrenergic receptor is.

3. Intravital microscopy to study regulated exocytosis in the SSGs of live rodents

The limitations seen in *in vitro* and *ex vivo* studies are being overcome by IVM, which encompasses a series of light microscopy-based techniques, such as wide-field fluorescence, laser scanning confocal, multiphoton, and spinning disk microscopy [84] (Table 1), which are used to image several biological processes in live animals including tissue dynamics, cell migration, immune response, and synaptic plasticity [85-88]. Recently, IVM has been extended to image the dynamics of subcellular structures in live rodents, providing also quantitative data on the processes of interest [89-92]. This has been accomplished by the development of specific surgical techniques and organ holders that have enabled considerable reduction in motion artifacts due to the heartbeat and respiration, which are the major challenges in performing subcellular imaging *in vivo* [84] (Fig. 10).

Techniques	Excitation	Light source	Detection	Advantages
Widefield	Single photon	Mercury lamp UV/Visible	CCD	Fast acquisition Limited depth Low costs
Confocal	Single photon	CW laser UV/Visible	PMT	Limited depth High spatial resolution
Spinning disk	Single photon	CW laser UV/Visible	CCD	Limited depth Fast acquisition Low photodamage and photobleaching
Multiphoton	Two/three photons	Tunable lasers NIR/IR	PMT	Extended depth Endogenous fluorescence No off-focus emissions
Second and third harmonic generation	Two/three photons	Tunable lasers NIR/IR	PMT	No energy absorption Imaging collagen, myosins, myelin, and lipids
Fluorescence lifetime imaging microscopy (FLIM)	Single/ Two-photon	CW laser Tunable lasers	PMT	Extended depth Information on the tissue environment
Coherent anti-Stokes Raman Scattering (CARS) microscopy	Single photon	Tunable lasers NIR/IR	PMT	Imaging myelin, lipids

Table 1. Imaging techniques used for intravital microscopy.

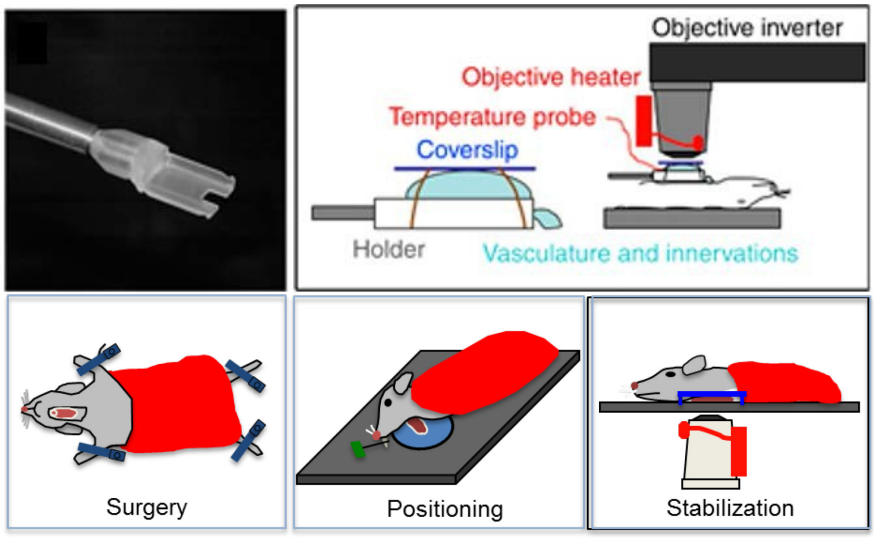

Figure 10. Development of tools and stabilization methods for live rodent intravital imaging of the SSGs. Initially, gland holders were developed that allowed the SSG of a rodent to be externally stabilized for imaging in the upright position (top image) [91]. In order to simplify the technique and be able to add pharmacological inhibitors directly to the gland while imaging, methods were developed for positioning, stabilizing and imaging the rodent in the inverted setting (bottom image).

The first successful attempt to visualize membrane trafficking events was achieved in the kidney of live rats by using two-photon microscopy where the endocytosis of fluid-phase markers, such as dextrans, or the receptor-mediated uptake of folate, albumin, and the aminoglycoside gentamicin were followed in the proximal tubuli [93]. Recently, the salivary glands have proven to be a suitable organ to study the dynamics of membrane trafficking by using either two-photon or confocal microscopy. Systemically injected dextrans, BSA, and transferrin were observed to rapidly internalize into the stromal cells surrounding the salivary gland epithelium in a process dependent on the actin cytoskeleton [91, 94]. Moreover, the trafficking of these molecules through the endo-lysosomal system was documented, providing interesting insights on early endosomal fusion. As for regulated exocytosis, IVM has been a powerful tool to investigate the molecular machinery driving the process in various organs. In the SSGs, the use of selected transgenic mice expressing either soluble GFP (GFP mouse) or a membrane-targeted (Tandem Tomato) peptide (mTomato mouse) has permitted the characterization of the dynamics of exocytosis of the secretory granules after fusion with the plasma membrane, providing novel insights on this process [13] (Fig. 11).

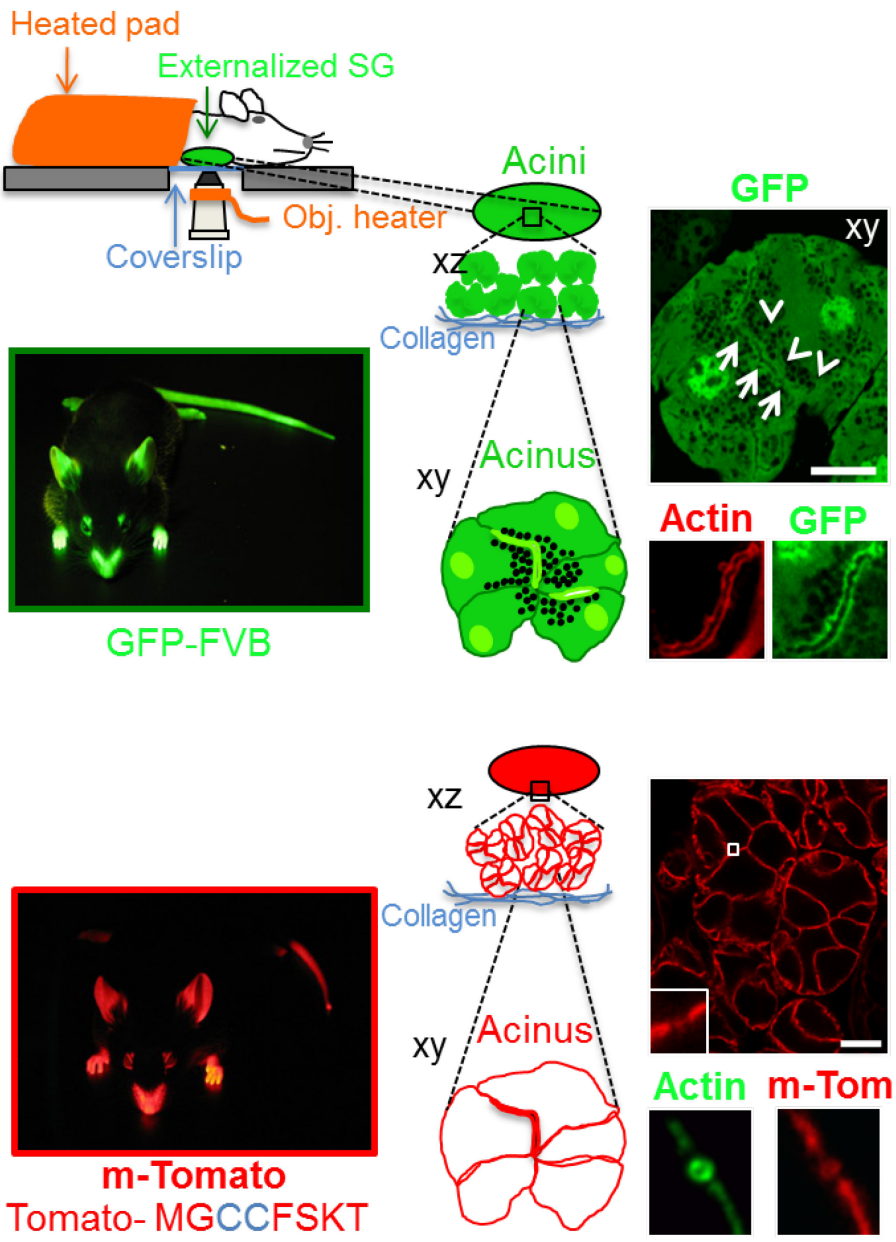

Figure 11. Mouse models used to characterize regulated exocytosis in the SSGs of live rodents. Cytosolic GFP is excluded from the secretory granules in the GFP-FVB mice (top mouse). The granules, seen as black dots, are packed at the APMs of two adjacent acinar cells (arrows), whose nuclei are bright green. F-actin (stained by Phalloidin 594, red) is specifically lining the APMs of both cells, and in the middle are the canaliculi. An increase in GFP signal is also seen in that region. This mouse was used to characterize the overall

kinetics of regulated exocytosis in the SSGs. In the m-Tomato mouse (bottom image), the entire PM is outlined with a Tandem Tomato probe. A cross-sectional view of the APM and canaliculi stained by Phalloidin 488 (green) is seen. When secretory granules fuse with the APMs, the m-Tomato probe diffuses into their limiting membranes. This mouse strain was used to understand the dynamics and kinetics of individual fused secretory granules. Figure from, [13].

The submandibular salivary glands are ideal for IVM because they are easily accessible through surgery, and they are located in the neck area where motion artifacts are reduced when compared to other areas, such as the body cavity. Furthermore, the process of regulated exocytosis in the acinar cells can be easily imaged with confocal or two-photon microscopy since the cells are located 10-15 μm below the surface of the glands and possess large, easy to visualize secretory granules that are packed at the APM where they undergo fusion and integration [13]. In addition, the apical and basolateral surfaces of the acinar cells can be directly and independently targeted through the Wharton's duct or the vasculature, respectively, with pharmacological agents, fluorescent probes, plasmids, viruses or peptides. Cannulation of the Wharton's duct is one technique that is particularly used to directly target the apical plasma membranes to study the process of regulated exocytosis without disturbing the architecture of the glands, which is important for preserving the biophysical aspects of the process [95] (Fig. 12). The techniques used to study regulated exocytosis on a subcellular level in the submandibular salivary glands of live rodents have been developed by our lab and as a part of my work are expanded upon in the methods section of this thesis [96, 97].

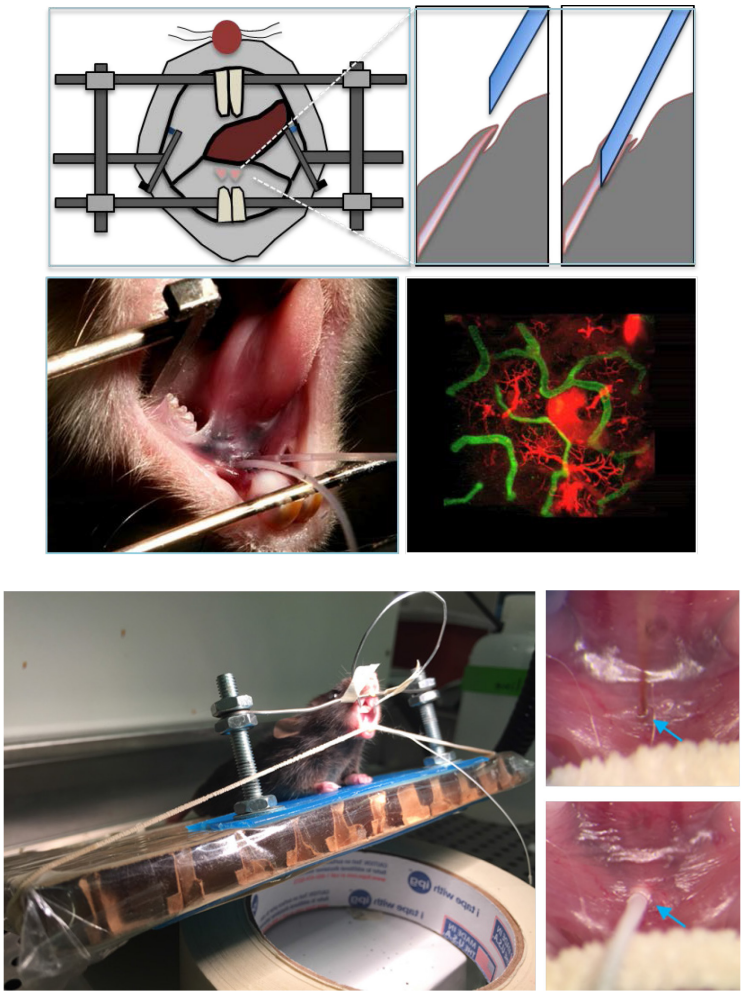

Figure 12. Delivery of agents by cannulation into Wharton's Duct. The mouth and tongue of the rodent were held in place away from the two openings to Wharton's Duct located underneath the tongue (top left). A cannula was carefully inserted into Wharton's Duct (top right). A photo of the procedure just described is shown in the bottom left image. Injection of red dextran into Wharton's Duct and green dextran through a tail vein (bottom right) showed that the apical and basolateral PMs are physically separated from one another. Figure from, [98]. Bottom left panel is a mouse set up with a cannula inserted and to the right is the process of cannulation of in mice, where first the opening of the duct is found using a small flexible metallic blunt-ended needle (top) and then the cannula is inserted as described in the text (bottom).

4. Main hypotheses

It has been suggested that exocytosis of the secretory granules in the SSGs occurs in a consistent manner from one animal to another. However, the machinery controlling the integration of the secretory granules after their fusion with the PM has not been fully elucidated. Recently, we have shown that in the SSGs of live rodents, an actomyosin complex, formed by F-actin and two isoforms of the actin motor non-muscle myosin II (NMIIA and NMIIB) is assembled onto the secretory granules upon their fusion with the APM [13]. In summary, it was determined that F-actin's role is to perform three functions that determine the post-fusion fate of the secretory granules: 1) facilitate the gradual integration of the granules into the APM, 2) stabilize the granules by counteracting the hydrostatic pressure in the canaliculi that is generated during the flow of saliva, and 3) prevent homotypic fusion between the granules from occurring [13] (Fig. 13).

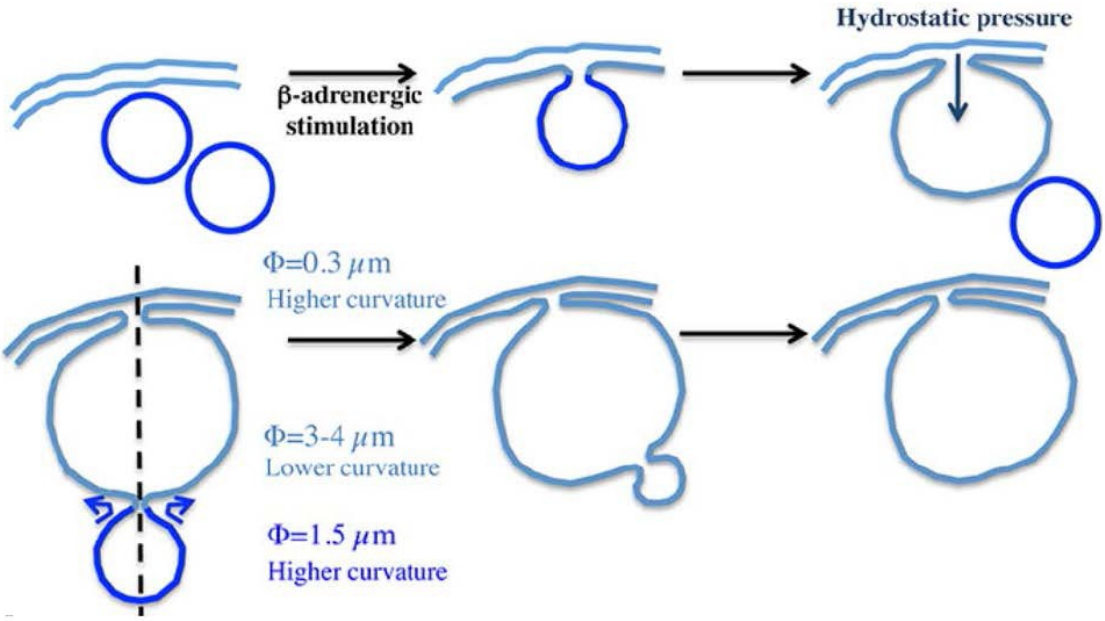

Figure 13. Disruption of F-actin (10 µm Cytochalasin D). Upon treatment with 10 µm Cytochalasin D, secretory granules (SCGs) fuse with the APM at a normal rate, but fail to integrate, and instead increase in size, forming large vacuoles. This process seems to be driven by the increase of the hydrostatic pressure inside the ductal system and the canaliculi. At the same time, the remaining SCGs start to fuse with the vacuoles and integrate at a rate comparable to that observed in control conditions. The driving force for this process may reside in the now favorable difference in curvature between the SCGs and the vacuole. Figure from, [13].

However, the roles and regulation of NMIIA and NMIIB during secretory granule integration have not been resolved, as previously mentioned. The first part of this thesis addresses if an F-actin scaffold is able to generate the necessary force to promote the integration of the fused secretory granules into the APM as NMII stabilizes the nascent filaments, or if the NMII isoforms are required to provide the contractile activity for

integration to occur. Furthermore, whether NMIIA and NMIIB have distinct roles and whether both are needed during the exocytic process, and how will be addressed. The second set of questions that will be answered in this thesis relate to the regulation of actomyosin contractile activity. More specifically, if NMIIA and NMIIB are the main mechanoenzymes responsible for actomyosin contractile activity, which kinase(s) activate the myosins, what regulates them and the myosins, and how?

Ultimately, by answering these questions I will be able to place the β-adrenergic signaling pathway in relation to a biophysical readout: that is, the kinetics and dynamics of remodeling of individual secretory granules during exocytosis. More specifically, these findings will shed light on the role that the actin cytoskeleton plays as a mechano- transductor complex which links cell signaling to membrane dynamics. In other words, once we understand the mechanical aspects of the system (i.e. the kinetics of secretory granule exocytosis and the roles each of the two myosins play during the process), any perturbations in the assembly and function of the actomyosin scaffold, or in the signaling pathway further upstream will be seen as changes in the kinetics of the process, or changes in the morphology of the fused secretory granules as they integrate into the APM of the acinar cells. Thus, the overall aim is to further establish a live rodent model system by which we can experimentally study the biophysics and cell biology of the β-adrenergic pathway, the actin cytoskeleton and regulated exocytosis *in vivo* – something that has not been done in the past. Ultimately, the direct medical applications of this research have relevance to drug discovery and testing in a number of different fields, including the cancer field, asthma, inflammation, the immune response and the circulatory system; as the β-adrenergic pathway, the actin cytoskeleton and

regulated exocytosis are at least, in part, involved in all of them.

4.1. NMIIA and NMIIB may play distinct roles in driving secretory granule integration into the apical plasma membranes of submandibular gland acinar cells in live rodents post-fusion

My hypothesis is that NMIIA and NMIIB drive secretory granule exocytosis in the SSGs and that their roles are inherently linked to differences in their biophysical properties. Here, I will first describe NMII structure and function, and then focus on the differences in the biophysical properties of the two isoforms. Next, I will discuss the structure, function and assembly of the F-actin scaffold around the secretory granules to give a perspective of how NMII would interact with it. Finally, I will elaborate my main working model in which NMIIA and NMIIB play distinct roles in the process of membrane integration by acting on two distinct processes during the integration of the secretory granules.

4.1.1. Non-muscle myosin II structure and function

Myosins are a large superfamily of molecular proteins that are present in all eukaryotic cells. Phylogenetic analysis has grouped the myosins into 19 separate classes [99, 100]. The conventional myosins from muscle and non-muscle cells form class II (the latter called NMII in this paper) [101]. While much progress has been made mostly on NMII (and also on myosins I and V, and more recently on myosins VI, VII and XV), very little is known regarding the function and localization of the remaining myosins. However,

it is believed that the biophysical properties differ widely between all the myosin classes and their isoforms [101]. In addition, most myosins can walk towards the barbed (plus) end of F-actin, while myosin VI and tail-less myosin IXb are pointed (minus) end directed [102, 103].

All myosins studied thus far, with exception of myosin 18A, share a common domain at their N-terminal heads by which they can bind and walk along F-actin, and hydrolyze ATP [104]. While Myosin 18A lacks actin-activated ATPase activity, it still has a C-terminal tail, which in general serves to anchor and position the myosins, and the myosins also possess a neck domain, which binds light chains or calmodulin by its IQ motif(s) [101, 104]. Furthermore, while the N-terminal heads are largely conserved among the myosins, their tail domains have wide variability in length and composition [101]. Different myosins can form two or more headed structures through interactions at their C-terminal tails. The tails can contain various motifs that may regulate this aspect of the myosins, including the GAP, FERM, PH, and SH3 domains [101].

Furthermore, based on their sequences, the myosin II class is further broken down into 1) sarcomeric myosins (in cardiac and striated muscle) and 2) vertebrate smooth and non-muscle myosins in mammals [101] (Fig. 14 and 15). Interestingly, sarcomeric myosins are constitutively active and their binding to F-actin is predominantly regulated by troponin-tropomyosin activity, which is regulated by Ca^{2+} [101]. On the other hand, vertebrate smooth muscle myosin and NMII activity is regulated through phosphorylation of their regulatory light chains (RLCs) [105, 106]. The amplitude of smooth muscle myosin II force production (and regulatory light chain phosphorylation) has been shown to be

dependent upon the balance between Ca^{2+} – and – calmodulin-activated myosin light chain kinase (MLCK) and type 1 myosin light chain phosphatase (MLCP) [101]. As will be discussed later, it is also believed that NMII activity (which is grouped into the same category as smooth muscle myosin II) is regulated in the same manner.

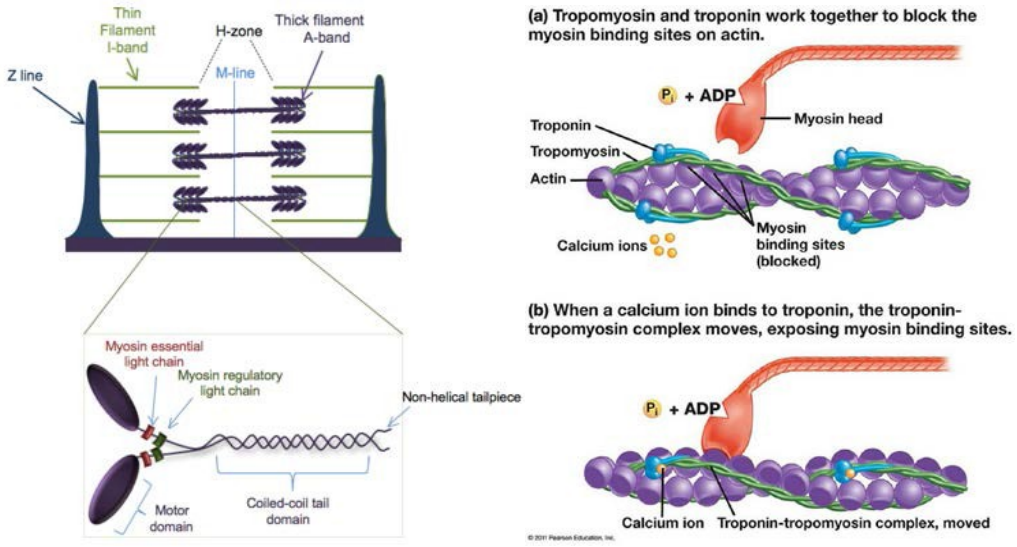

Figure 14. Sarcomeric muscle myosin II function. Sarcomeric muscle myosin II is constitutively active, and its binding to F-actin is regulated by troponin and tropomyosin, as depicted above, right panel. Panel on the left shows the myosin II distribution in the muscle, where the H-zone is composed of the myosins arranged as bipolar filaments, and their N-terminal heads can bind and move F-actin at the thin filament I-band to cause contraction. Below, is a larger image of a myosin II dimer that is within one of the bipolar filaments. Figures from, [107] and https://www.premedhq.com/troponin-and-tropomyosin.

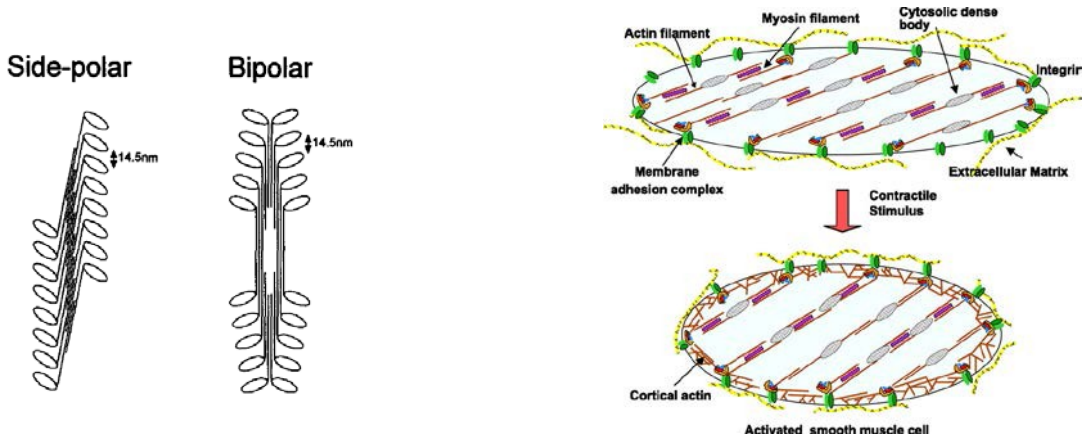

Figure 15. Contractile unit arrangement of smooth muscle myosin II. Smooth muscle myosins can form side-polar and bipolar filaments, while non-muscle myosin II can only form bipolar filaments. On the right is a representation of how contractile units of smooth muscle myosin II are distributed in smooth muscle cells. Images from, [108-110].

When it comes to their activities in cell, it is interesting to note that all eukaryotic cells express at least one myosin II gene [101]. Myosin II (both muscle and non-muscle) is unique in that it can form filaments through interactions to each other by their C-terminal coiled-coil α-helical tails (in this work described as bipolar NMII filaments) [101]. Smooth muscle myosin II can also form side polar filaments where the heads are packed closer in to the midline than they are in bipolar filaments [105] (Fig. 15). Myosin 18A has been particularly found to associate with NMII C-terminal tails and may serve as a regulatory element in their localization, bipolar filament formation and activity [104]. Furthermore, the phosphorylation of the myosin II heavy chains can also regulate filament formation and function, however it is not well understood how this occurs; although some evidence for it has been found for NMIIB, where phosphorylation has been shown to inhibit bipolar filament formation [111]. Overall, it is thought that the differences in the biophysical,

structural, and functional elements of the different myosins reflects how and where they are present in the body, and what processes they regulate in which cell types. In the remainder of this thesis, the focus is specifically on non-muscle myosin II as it relates to regulated exocytosis in the SSGs.

NMII isoforms are known to bind F-actin and to either stabilize it by cross-linking/bundling multiple filaments together, or to generate contractile structures in which filaments are moved via the NMII ATP-based motor activity [112] (Fig. 16). In addition, NMII motor activity may cause F-actin depolymerization, which can promote contractile activity [113]. In this manner, they are able to carry out major roles during different physiological processes, such as tissue development, generation and maintenance of polarity, wound healing, angiogenesis, immune function and synaptic network formation [114]. On a cellular level, they are involved in stress fiber reorganization during cell migration and cell shape changes, filopodia and lamelipodia maintenance during growth cone formation and axon guidance, cell adhesion dynamics, endo- and exo-cytosis, and cytokinesis [114]. In fact, NMII isoforms have been found to be regulators of nearly all cellular processes that require the spatiotemporal organization of cytoskeletal scaffolding and movement, and we expect them to play a similar role in promoting the integration of the secretory granules into the APMs in the SSGs.

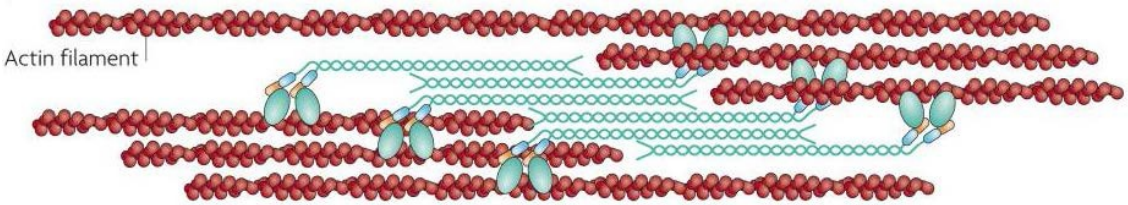

Figure 16. NMII bipolar filaments promote F-actin contraction. Figure from, [115]. NMII bipolar filaments (aqua color) interact with each other through their C-terminal coiled-coil tails, and each holoenzyme is bound to an actin filament by its N-terminal globular heads at the opposite end. Contraction of actin filaments occurs when the two globular motor heads of each holoenzyme walk in opposite directions along the actin filaments, causing them to slide towards one another.

NMII is a hetero-hexameric protein complex consisting of non-muscle myosin heavy chain (NMHC) dimers [109]. Each dimer is non-covalently associated with two myosin light chains: the regulatory and essential light chains (RLCs and ELCs, respectively) [114]. Each NMHC dimer with its associated light chains is a holoenzyme and the dimers can be either hetero-dimers (consisting of heavy chains from different NMII isoforms), or homo-dimers (where the heavy chains are of the same isoform) [116-120]. At the amino acid level, the NMHC is structurally and functionally characterized by an asymmetric modular organization, containing 1) a N-terminal motor/ATPase domain that binds to and walks along F-actin towards its plus-end, 2) an intermediate neck domain where the light chains bind, and 3) a C-terminal α-helical coiled-coil tail domain through which two or more NMII holoenzymes interact to form bipolar NMII filaments, as previously mentioned [114]. In worms, flies, and mammals, it is thought that RLC phosphorylation (at S19 and/or T18) causes NMII to unfold into its active 6S conformation,

triggers each holoenzyme to assemble into high order bipolar filaments, and activates the enzymatic (motor) activity of each holoenzyme in order to promote actomyosin-mediated contractile activity [114] (Fig. 17). The bipolar filaments can be either hetero-filaments, or homo-filaments depending on if they are composed of multiple myosin isoforms, or just one, respectively [116, 118-120] (Fig. 18).

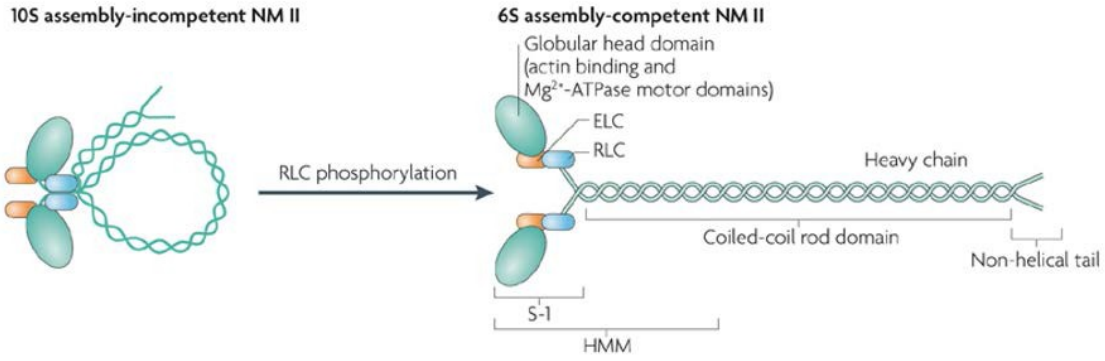

Figure 17. Phosphorylation of NMII RLCs is necessary for its activation. Phosphorylation of NMII RLCs at S19T18 by regulatory kinases causes its C-terminal coiled-coil tail to unfold from its N-terminal head; thus, allowing it to form bipolar filaments and for its motor/ATPase activity to function when the myosin is bound to F-actin. During activation, NMII goes from a 10S incompetent assembly to 6S competent assembly. Figure from, [115].

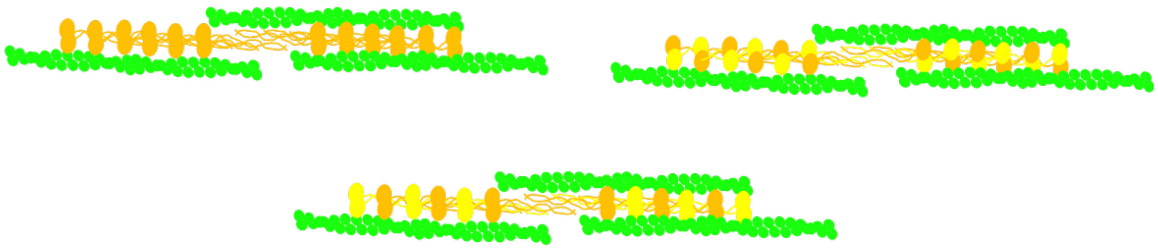

Figure 18. NMII isoforms can form hetero- and homo-bipolar filaments. Top right and bottom images are representations of two possible scenarios of how NMII can form bipolar hetero-filaments on F-actin; where each color represents a different NMII isoform. A NMII bipolar homo-filament is represented bound to F-actin filaments in the top left image. The formation of different types of filaments may confer a range of properties to the NMII units, thus allowing them to regulate a wide range of processes that would require slight differences in tension.

In mammals, there are three genes located on different chromosomes that encode for three different non-muscle heavy chain (NMHC) isoforms: Myh9 (NMIIA), Myh10 (NMIIB) and Myh14 (NMIIC) [114] (Fig. 19). Each NMHC is believed to associate with the same RLC in a given cell type. Furthermore, each isoform is 7.5 kilobases long, has multiple splice variants and altogether possess 60-80% amino acid sequence similarity (NMIIA and NMIIB are 89% identical at the amino acid level and 74% identical at the nucleotide level) and high structural/functional homology [114]. In the SSGs, only NMIIA and NMIIB were found to be associated with the secretory granules, and they will be the focus of the discussion from now on. Despite their similarities, differences in their functions are apparent during such processes as cell migration, wound healing, and angiogenesis, where they are not able to substitute for each other [121]. In addition, in some

cells only one isoform is used to perform a specific function, as shown for NMIIA that is specifically needed for normal maintenance of cell-cell adhesions and the normal localization of major junction proteins, such as E-cadherins, β-catenin and ZO-2 [115]. Furthermore, certain cells contain only one NMII isoform (e.g. platelets, lymphocytes, neutrophils, brush border enterocytes and granulocytes have only NMIIA, and neuronal tissue is mainly enriched in NMIIB) [115, 122, 123].

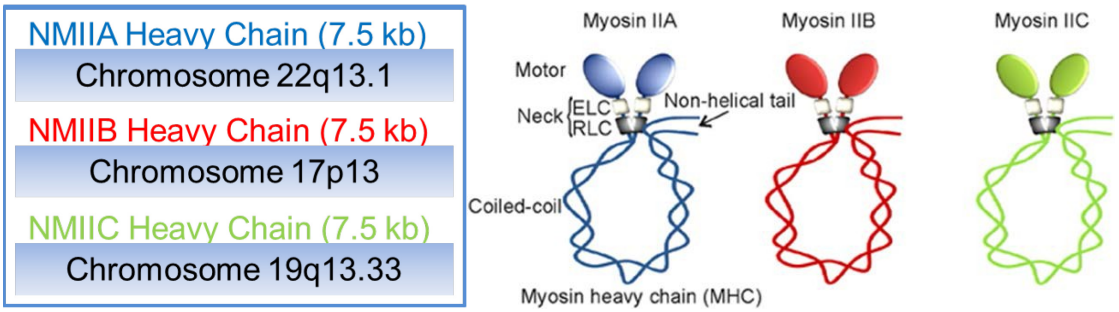

Figure 19. Similarities and differences between the NMI isoforms. NMIIA, NMIIB and NMIIC: All have high structural and functional homology, share the same type of regulation required to activate them. However, all three come from different chromosomes, designating them to be different genes. Figure on right from, [124].

On the other hand, there are processes where NMIIA and NMIIB are found to co-localize and work in unison to exert tension on F-actin (e.g., during cytokinesis), as either homo-filaments, hetero-filaments, or a combination of the two [119]. Furthermore, in processes where their functional motors are not necessary, there is evidence that both NMII isoforms are able to substitute for one another and play a role in cross-linking actin filaments without contracting them [115]. The commonalities and differences between all the mentioned roles of the myosins translates to the following: in order to understand the

roles each of the two isoforms play during a particular process, it is important to relate the differences in their biophysical properties and their regulation to the relative differences within the process they are attempting to regulate. Here, we apply this understanding to the roles of the two isoforms during regulated exocytosis in the SSGs of live rodents.

4.1.2. Biophysical differences between NMIIA and NMIIB

The difference in the kinetics and mechanical properties between the myosins is determined by two factors: 1) the duty ratio and 2) the kinetics of the power stroke during a step cycle [122, 125-127]. A step cycle consists of the entire process by which a myosin binds F-actin at a particular location and then comes off of the filament to take a step forward to rebind F-actin further up on the filament, until the process starts again (Fig. 20). The duty ratio is the fraction of time that its motor head is attached to the filament during the process; the higher the duty ratio, the more "processive" the myosin is considered to be. On the other hand, the power stroke is the mechanical act by which a forward step is taken by the myosin head; for NMII the displacement is 6.9 +/- 1.2 nm towards the plus-end of F-actin, producing 4-5 pN of force during each power stroke [128]. Interestingly, it has also been shown that NMIIB, when in bipolar filament form can translocate F-actin at an average rate of 48 +/- 2 nm/sec [128]. However, it should be noted that NMIIA and NMIIB translocate along F-actin at different rates and with different binding capacities.

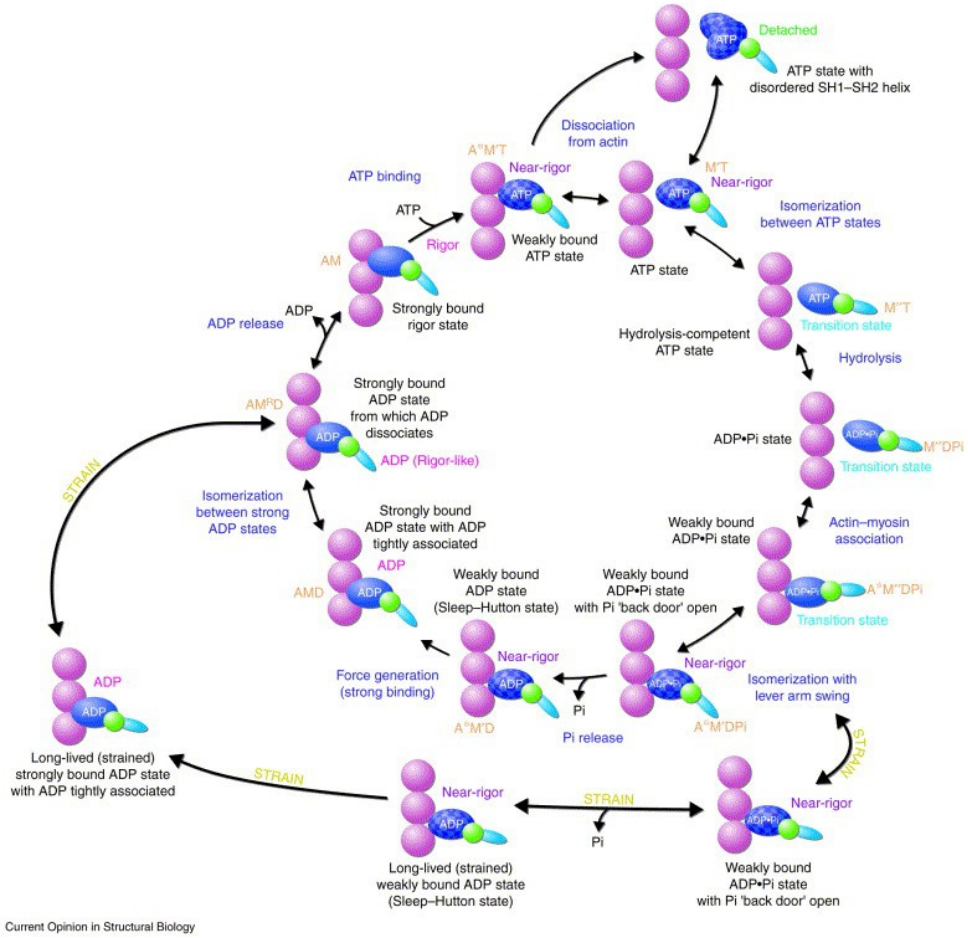

Figure 20. The step cycle of a myosin motor. In relation to NMII (all isoforms), in particular, the N-terminal globular head stays bound to F-actin until an ATP is brought into its ATPase motor domain. NMII takes a step forward towards the plus end of F-actin as the ATP is isomerized and hydrolyzed to ADP + P_i, at which point it rebinds F-actin further up on the filament. Only when ADP + P_i are released from the motor domain and a new ATP comes in, does the process begin again. The NMII isoforms differ in the rate of their ATPases (kinetics) and the fraction of time they stay bound to F-actin (duty ratio). Figure from, [125].

Biochemically, the step cycle for each isoform is determined by the rate of hydrolysis of ATP by the NMII motor domain and the time it takes until a new ATP molecule is ready to be hydrolyzed (i.e. the rate of ADP + P_i release). Upon ATP binding, the myosin head comes off the filament and a power stroke is initiated [125]. As the myosin head is displaced forward, ATP is isomerized and hydrolyzed to ADP + P_i, at which point it binds the filament at its new location. The time that it takes for the phosphate (P_i) and ADP to be released defines the duty ratio for a particular myosin. All myosin differ in their kinetics (ATPase rates) and duty ratios [129-131].

If during the power stroke the myosins are held stationary, by being anchored through their C-terminal tails (as would occur with the formation of NMII bipolar filaments), F-actin would be translocated across the NMII surface. The formation of bipolar filaments leads to the myosins being arranged like a single-, or double-headed bouquet of flowers, where the myosin heads are the flowers. A certain ratio of those heads at one end of the bouquet would be bound to an actin filament at any given time depending upon the stage in its step cycle [128]. Each end of the double-headed bouquet can also bind adjacent filaments and by walking in opposite directions, those filaments would be induced to slide towards each other; and in this manner the myosins can create contraction of an F-actin scaffold, causing what is known as actomyosin contraction [115] (Fig. 16). Furthermore, some studies have also shown that in the same manner, NMII motor activity can cause F-actin depolymerization (or actin filament shortening), which can induce actomyosin contractile activity [113].

The differences in the kinetics and mechanical properties between NMIIA and NMIIB become apparent when their motor/ATPase activities, and their processive

properties are measured. While both isoforms show second-order rate binding constants for ATP, the ratio of second-order ADP and ATP binding rate constants is approximately 20 for NMIIA and 10 for NMIIB. NMIIA propels F-actin two to three times faster than NMIIB (i.e. it takes a power stroke two to three times faster than NMIIB) and thus causes a higher rate of contraction of actin filaments [114]. In addition, the duty ratio of NMIIB is about 25%, which is significantly higher than that of NMIIA, and NMIIB can move in both directions on actin filaments at stall (i.e. when the force on the associated F-actin is higher than the force that NMIIB can produce to counteract it) [128, 132, 133]. For this reason, NMIIB is believed to be better suited for stabilizing and regulating slow changing cytoskeletal tension in one direction, while NMIIA is better suited for regulating much more dynamic processes that would require relatively fast reorganization and don't require as much force to stabilize [128, 132, 133] (Table 2). Thick bipolar myosin filaments can also possess a combination of both properties, and this may be dependent upon the relative concentrations of the NMIIA and NMIIB isoforms present; although, this may occur to a limited extent, since the difference in biophysical properties between the two isoforms may cause them to interfere with one another. Altogether, these properties make the NMII isoforms applicable to a wide range of processes where the degree of mechanical tension needs to be regulated.

NMIIA properties	NMIIB properties
Low duty ratio, highly dynamic	Highly processive
ATPase is 2-3 times greater than that of NMIIB	May walk towards minus-end of F-actin upon overloading force, without readily falling off
Best suited for lower tension, but more dynamic processes	Best suited for stabilization and slower dynamics

Table 2. Biophysical properties of NMIIA and NMIIB

4.1.3. F-actin: Structure, function and assembly

While it has been measured that a single NMII can generate 4-5 pN of force, in order to know in which direction this force is being applied we would need to know the orientation of the actin filaments that make up the F-actin scaffold around a granule. We know that a randomly assembled scaffold patterned with NMII *in vitro* will contract into a ball. Furthermore, in cells, F-actin assembly is highly coordinated and directed, and carried out by a multitude of actin binding proteins (ABP) and regulatory proteins [134, 135]; as a result, F-actin networks can be built by cells in order to carry out specific tasks as efficiently as possible.

Actin is an evolutionarily highly conserved 42 kDa monomeric ATP-binding protein that consists of 375 amino acids arranged into two structurally related domains, which can be further subdivided into subdomains 1 to 4 [136]. An actin monomer (called G-actin, or globular-actin) is flat and can fit into a rectangular prism with dimensions of

55Å x 55 Å x 35 Å [136]. Two clefts are formed in between the subdomains: the upper cleft is formed between subdomains 2 and 4, and the lower cleft is formed between subdomains 1 and 3, and each of these has specific roles. The upper cleft binds a nucleotide (ATP) and an associated divalent cation (Mg^{2+}), while the lower cleft (also called the target binding cleft) is lined predominantly by hydrophobic residues that provide the major binding site for most ABPs and it also mediates contacts between adjacent G-actin subunits [136]. Multiple G-actin subunits can polymerize to form a linear actin filament, called filamentous or fibrous actin (also known as F-actin). As F-actin forms, each subunit becomes flatter and allows for more extensive contacts between adjacent subunits, which together with their helical nature, promote filament formation [136-138] (Fig. 21).

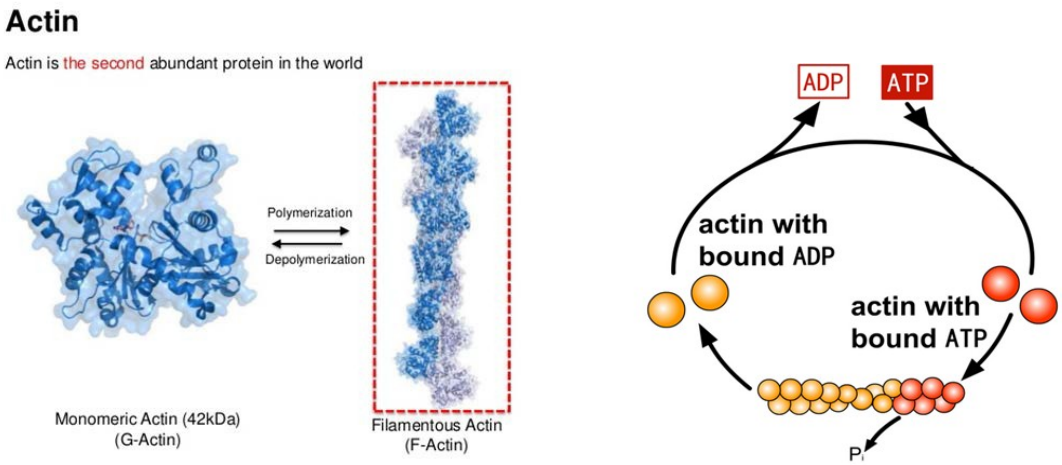

Figure 21. F-actin formation and dynamics. Single G-actin monomers assemble one by one into a helical filament structure called F-actin (left image), in a process called polymerization. During the process, G-actin monomers bind ATP, which allows them to polymerize into an F-actin filament at the plus-end, and in so doing they hydrolyze ATP to ADP, which induces their depolymerization back to G-actin monomer from the minus-end

(right image). New monomer that arrange at plus-end, soon end up being closer to the minus-end as more monomer polymerize to the plus-end and other depolymerize from the minus-end. The process is called treadmilling. Images from, http://cc.scu.edu.cn/G2S/Template/View.aspx?courseType=1&courseId=17&topMenuId=113305&menuType=1&action=view&type=&name=&linkpageID=113700 and http://www.slideshare.net/suknamgoong/cell-bio7.

The regulation of the actin cytoskeleton *in vitro* is different from its regulation in cells. *In vitro*, G-actin and F-actin exist in dynamic equilibrium: G-actin monomers spontaneously polymerize to the fast-growing barbed (plus) end of F-actin, while other monomers depolymerize from the pointed (minus) end on the other side of the filament. At steady-state, this process is called treadmilling [139]. It occurs as the stable ATP-actin monomers are spontaneously added to the plus-end of F-actin, and polymerization induces ATP hydrolysis in the filament, causing the less stable ADP-actin monomers to dissociate faster from the minus-end than they otherwise would [139] (Fig. 21).

In cells, however, since spontaneous F-actin assembly is kinetically unfavorable, actin-binding proteins called nucleating factors are necessary to start the process and other ABPs function in filament branching, elongation, capping/uncapping, severing, cross-linking, depolymerization, and monomer sequestration [135, 136, 140] (Fig. 22). Thus, cells generate specific actin cytoskeleton networks by either nucleating actin monomers *de novo*, or by generating free barbed ends to serve as templates for polymerization, which they achieve by severing or uncapping existing filaments [136, 140]. They then stabilize the filaments by capping the barbed and pointed ends to prevent treadmilling activities, and

cross-linking the filaments [136, 140]. In addition, it has been recently found that F-actin can be cross-linked into curved bundles to form F-actin rings through their interactions with septin GTPases, which are another component of the cytoskeleton and will be described later [141]. Altogether, ABPs act to determine the direction, rate, timing and stability of F-actin assembly that allows it to be versatile in its ability to generate force, assemble into structural scaffolds, and act as motor tracks for proteins to reach specific destinations [136, 142-144].

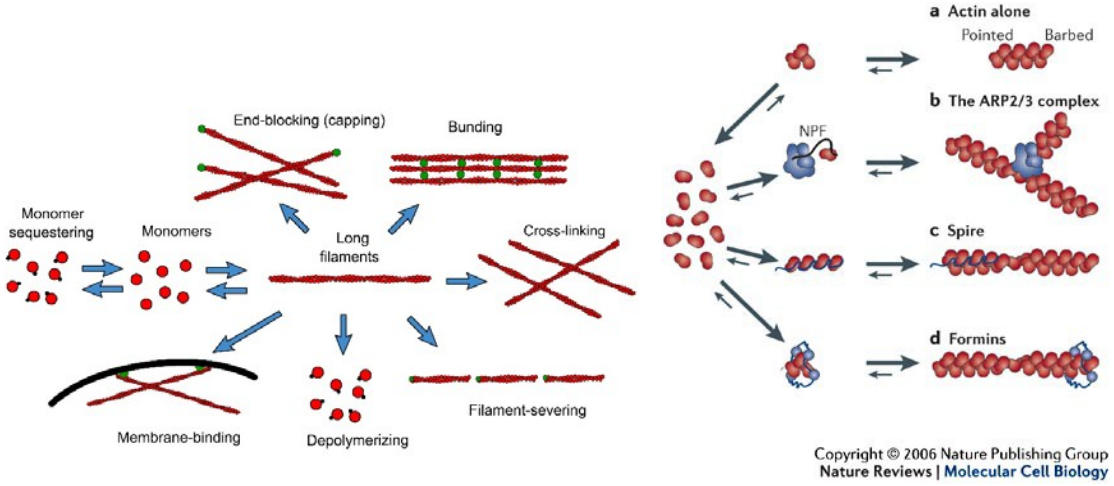

Figure 22. Polymerization of F-actin into different structural organizations and its regulation by various actin binding proteins (ABPs). F-actin can be polymerized and depolymerized from and to G-actin monomers into linear, branched, or curved (not shown) structures, as necessary. This is regulated by a plethora of ABPs, which play various roles in the process, including G-actin monomer sequestration, bundling, capping, severing, polymerization and depolymerization, promoting membrane binding, etc. (left figure). Some of the more prevalent ABPs involved in F-actin polymerization *de novo* in cells are ARP2/3 (branched filaments), Spire, and Formins (right figure). Figures from, [145].

Thus, during exocytosis in the SSGs, the structure of the F-actin scaffold may be specifically designed around the secretory granules so that the least amount of energy is required by the cells in order to carry-out the exocytic process in a timely manner. Furthermore, the various ABPs which regulate the assembly of F-actin networks *in vivo*, may also regulate how, where and when different F-actin interacting molecules, such as NMII, associate with it. In general, F-actin has a NMII binding site every 2.7 nm and furthermore, it should be noted that its polarity is not apparent by simply looking at any filament: the polarity (i.e. the barbed and pointed ends) of F-actin was determined (and appeared) when filaments were densely patterned with myosin s1 fragments (which are just mostly the head portions of NMII) [146-148] (Fig. 17). As mentioned previously, it has been measured that NMII takes a step towards the plus-end of F-actin that is 6.9 +/- 1.2 nm; however, how NMII is dispersed along F-actin during actomyosin assembly is not clear. Yet, it is sufficient to say that *in vivo* actomyosin assembly is a highly regulated and coordinated event that is designed around the process it is meant to regulate, and to gain a better understanding of the regulation of its assembly and function *in vivo* during secretory granule exocytosis in the SSGs is one of the major goals of this thesis.

4.1.4. NMIIA and NMIIB may regulate different aspects of the same process

During regulated exocytosis in the SSGs, I expect that an F-actin scaffold is built around a newly fused secretory granule to regulate two specific and distinct events: 1) the stabilization and gradual application of forces to promote the integration of the secretory granule into the APM, and 2) the coordinated maintenance and expansion of the fusion

pore, as granule integration occurs. I envision that two different forces are applied onto the granules: the first, at the neck of the granule, which drives the APM centrifugally with respect to the fusion pore; the second which acts tangentially to the granular membranes and pushes them towards the APM (Fig. 23).

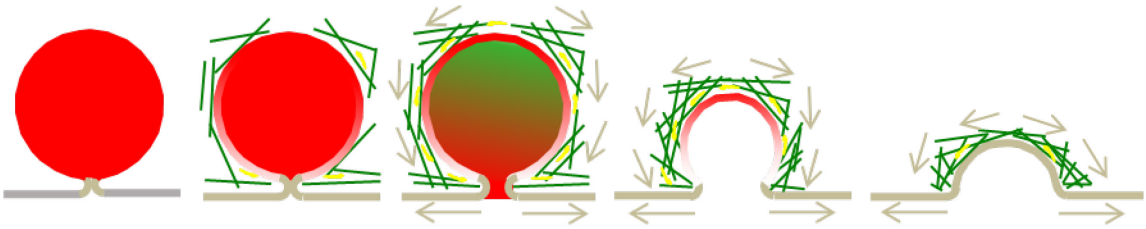

Figure 23. Secretory granule exocytosis post-fusion may require an open fusion pore and a compressive force to push the granules into the APM. An F-actin scaffold may be built around the secretory granules post-fusion in order to stabilize them and promote their gradual integration into the APM. I envision to areas where distinct force would need to be applied: at the neck area to maintain and possibly expand the fusion pore, and around the granules outside of the neck area in order to drive granular membranes into the APM.

As described previously, the fusion pore is formed when the SNAREs bring the membranes of the granule and the APM together, to first create hemi-fusion and then complete fusion, which connects the granule lumen to the extracellular environment. The fusion pore that forms initially has been measured to have a conductance of 80 pS and estimated to be 1 nm in diameter in synaptic vesicles [34, 149]. The expansion phase of the fusion pore, in general, is initially characterized by large (hundred-fold) fluctuations in pore conductance, designating its rapid opening and closing (rapidly going between hemi-fusion and complete fusion) until it reaches one of two fates: 1) irreversible expansion

(where it reaches a diameter of at least 20 nm in synaptic vesicles), or 2) complete closure (followed by possible detachment of the granule from the site of fusion) [34, 149, 150]. This pore flickering can last up to several seconds or more - the larger the granule, the longer the flickering may be [37]. Furthermore, the expansion of the fusion pore is regulated in a precise manner by some intracellular factors or a scaffold, and the actin cytoskeleton is a good candidate for the role; as shown by the fact that there is particular evidence that F-actin is mechanistically coupled with the SNARE machinery, which is involved in regulating the fusion pore [40, 42, 151-158].

Evidence for the actin cytoskeleton regulating the fusion pore has been previously reported in the adrenal chromaffin cells, where NMII activation and F-actin reorganization regulate the expansion of the fusion pore and the mode of quantal exocytosis [159]. Furthermore, in the exocrine pancreas, a similar exocrine gland model system to the SSGs, NMIIA was found to be responsible for the maintenance of the fusion pore [40]. In line with this, the high dynamic nature of the fusion pore may require a highly dynamic F-actin scaffold, and a highly dynamic myosin motor, such as the NMIIA isoform. My hypothesis is that NMIIA is the motor responsible for regulating the fusion pore in the SSGs.

Moreover, from a kinetic standpoint, it is difficult to imagine NMIIB to be involved in regulating the fusion pore. Indeed, NMIIB is a very slow, yet robust myosin motor that would be best suited for stabilizing tension and providing a gradual force. This would suggest that NMIIB may play a role on the granular membrane outside the neck area (Fig. 24). Its role could be to stabilize the granule against the hydrostatic pressure from the flow of saliva through the canaliculi, and promote the otherwise unfavorable integration of the large granules (~1.5µm) into the much narrower canaliculi at the APM, (0.3µm).

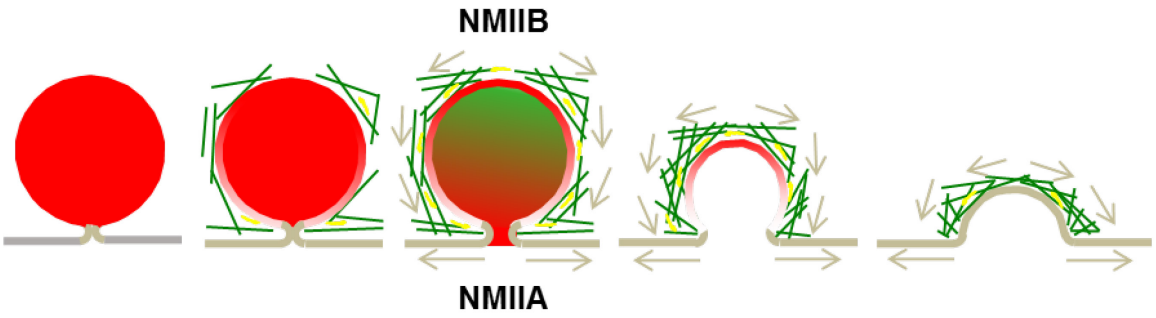

Figure 24. NMIIA and NMIIB may regulate different aspects of secretory granule integration. Post-fusion, secretory granules integration in the SSGs is regulated by an actomyosin complex, which provides the necessary force to maintain an open fusion pore, and drive the granules into the APMs. During this process we envision that the more dynamic NMII (isoform A) is responsible for maintaining the highly dynamic fusion pore, while the other (NMII isoform B) promotes granule stabilization and drives the granular membranes into the APM to cause complete integration.

Overall this hypothesis would imply that 1) NMIIA and NMIIB would most likely show regions of distinct localization around the granule; and, therefore they 2) would form homofilaments on separate F-actin microscaffolds, which may or may not be linked in some way. One continuous microscaffold would be tethered to the membrane of the granule, while the other would be associated with the fusion pore machinery. Evidence of a myosin being associated with the fusion machinery comes from myosin V, where an association between the tail of its heavy chain and synaptobrevin II in the exocytic fusion complex in synaptic vesicles has been demonstrated [160]. While myosin V may also be present at the fusion pore in the SSGs, it is likely that it may play a lesser complementary role to that of NMIIA, and at a different step in the exocytic process.

4.2. Actomyosin contractile activity during regulated exocytosis is regulated by the activation of NMII through phosphorylation of its regulatory lightchains

The second set of questions that I want to address in this thesis deals with the mechanism of recruitment of both NMII isoforms onto the secretory granules and the activation of the machinery leading to the formation of active contractile filaments. It has been found that the recruitment of the NMII isoforms on cellular membranes is dependent upon the interactions between their C-terminal coiled-coil tails and specific recruiting molecules. Indeed, when the C-terminal tails are rearranged or mutated, the isoforms are mislocalized and don't function properly [161]. Among these molecules: F-actin, which may act either directly or indirectly [162], Septin 2 and IQGAP [163, 164] may be the recruiting molecules in the SSGs.

As for the regulation of the formation of contractile filaments, I will check whether after the recruitment onto the secretory granules, NMIIA and NMIIB undergo phosphorylation. Indeed, both mono- and di-phosphorylation of their RLCs have been shown to be sufficient for bipolar myosin filament assembly and ATPase activity in other systems [114]. Specifically, di-phosphorylation has been shown to significantly enhance ATPase activity and produce more tension during the contraction of the actomyosin complex. Furthermore, the level of RLC phosphorylation has been seen to vary throughout the course of some processes, such as during cytokinesis and analogously it is expected to also vary during the exocytic process [165]. I want to determine whether NMIIA or NMIIB are phosphorylated during exocytosis, how this process is regulated and in turn, how it regulates the integration of the granular membranes. The levels of NMII phosphorylation

can be regulated by activation of one or more RLC kinases (such as Rho kinase (ROCK), citron kinase, myotonic dystrophy kinase-related Cdc-42-binding kinase (MRCK), protein kinase C (PKC), myosin light chain kinase (MLCK), or others), or myosin light chain phosphatase (MLCP) [114]. Therefore, I will identify the kinase(s) involved in this process and I expect that they must also be activated and recruited onto the granules in a similar manner as NMII.

4.2.1. Septin GTPases may regulate actomyosin contractile activity through the recruitment of activating kinases

The septin GTPases may play multiple roles in the regulation of actomyosin contractile activity, including promoting the activation of NMII, scaffolding the actomyosin complex, and bundling F-actin around the secretory granules. To date, 13 individual septin genes have been found in mammals and they are currently being extensively studied [166]. Interestingly, specific combinations of individual septin monomers can come together to form rings, homo- and hetero-filaments, and gauzes that are nonpolar to regulate a number of different processes [167] (Fig. 25). Filament formation is promoted during the hydrolysis of GTP to varying degrees by each septin monomer [168-170]. Once in filament or higher order formation, some individual septin monomers continue to hydrolyze the GTP to GDP, while others, such as Septin 6, may just hold onto their GTP without hydrolyzing it at all [171]. In addition, it has been shown that once a GDP is replaced by a GTP, the tight septin-septin interface formed during filament formation is significantly weakened [168, 171].

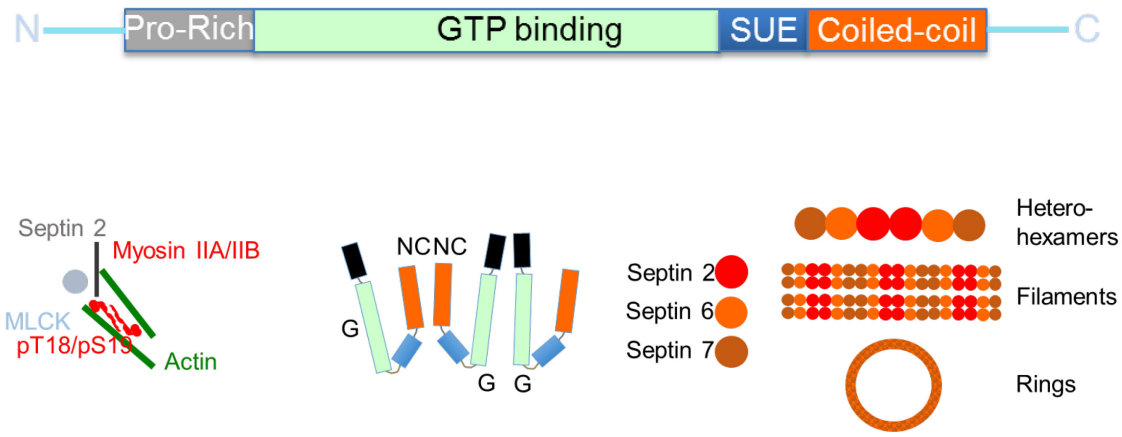

Figure 25. Structure and function of septin GTPases. All 13 septin GTPase monomers are composed of common regions, and septin specific elements (e.g. the SUE, Septin Unique Element, and the lengths of the carboxy-terminal and amino-terminal regions differ between septin monomers) that differentiate each one from the other (top figure). Septin monomers can assemble as homo- and hetero-filaments that are nonpolar in their arrangements, which can be further structured into higher order assemblies, such as rings and gauzes (bottom right images). One particular heterofilament that has been crystalized is composed of Septins 2, 6 and 7. Septin 2, in particular has been found to be important in the recruitment and activation of NMII during cytokinesis (bottom left image).

In general, it is unclear exactly how septins carry-out their functions, yet it appears to be linked to their varying rates of GTP hydrolysis and replacement, the variable regions within their sequences, and their cycling between the monomeric state and higher order structures. Septins have never been shown to function as individual monomers, but only as filaments and higher order structures, and because of this, they are collectively known as the fourth component of the cytoskeleton: Actin and tubulin monomers also hydrolyze nucleotides as they assemble into filaments and disassemble from them [172-175]. However, the difference appears to be that, unlike F-actin and microtubules, which exhibit polarity and are considered to be homogeneous in function, specific individual septin monomers can regulate specific functions when assembled into filaments or higher order structures. Furthermore, cells appear to pick and choose which septin monomers they need in a filament in order to regulate the different molecules involved in carrying out a particular process.

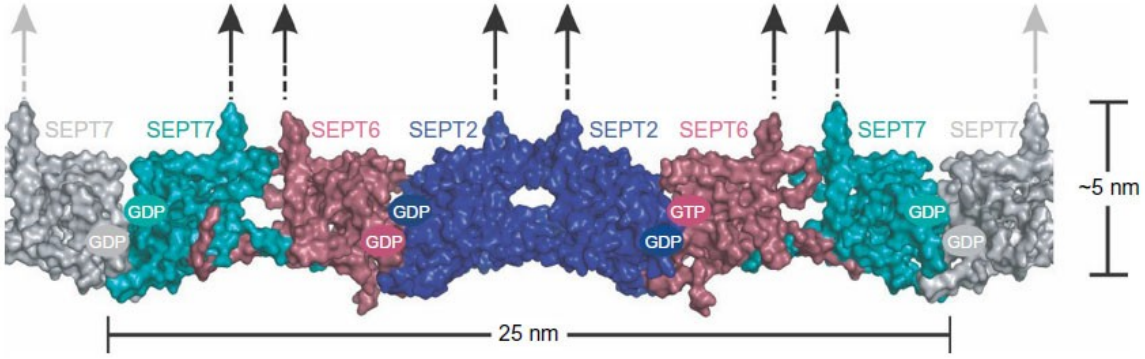

Figure 26. Structure of the Septin 2-6-7 complex. One septin heterofilament is the Septin 2-6-7 complex, which is an arrangement of Septins 2-6-7-7-6-2 in repeating hexameric nonpolar, order. Septin 6 is the only septin known to bind, but not hydrolyze GTP. Furthermore, not all septin monomers can interact to form homofilaments, although Septin

2 can. This structure has been crystallized, although it may have other septins in between to create various structural arrangement depending on the needs of the process it is involved in. Figure from, [176].

One septin heterofilament, which has been crystallized, consists of Septins 2, 6, and 7 arranged repeatedly in a linear, nonpolar fashion [176] (Fig. 26). Septin 2, as part of the 2-6-7 complex, but not Septins 6 or 7, has been specifically found to recruit NMII and promote its activation during cytokinesis [177]. In another study, Septin 7 has independently been found to compartmentalize cortical actomyosin, involving NMII, during cell movement [178]. In addition, homologous septins in yeast have been found to induce and possibly regulate higher order myosin filament formation [179]. Based on this, my working hypothesis is that the Septin 2-6-7 complex may scaffold F-actin and NMII in order to regulate actomyosin contractile activity, which may drive the post-fusion integration of the secretory granules into the APMs of the acinar cells during regulated exocytosis in the submandibular salivary glands of live rodents. Thus, in general, the septins may also serve as the link between β-adrenergic signaling, and actomyosin activity.

MATERIALS AND METHODS

1. Microscopy

1.1. Confocal microscopy

Intravital imaging (IVM) and immunofluorescent imaging were performed by a point-scanning IX81 inverted confocal microscope equipped with a Fluoview 1000 scanning head (Olympus America Inc.). All images were acquired using a Plan Apo 60x N.A. 1.42 oil immersion objective (Olympus America Inc.). All fluorophores were imaged using the appropriate lasers at low laser powers, as required by their excitation spectra (i.e. 405 nm, 488 nm, 561 nm or 633 nm laser). Fluorophores with slightly overlapping emission ranges were imaged using the "sequential" scanning mode to avoid bleed-through. Based on previous work [13], the optimal starting focal plane for imaging of the acinar cells in the SSGs was set at ~15 μm below the surface of the gland, as determined by visualization of the collagen capsule that surrounded the acinar cells. For IVM specifically, the acquisition speed was ~0.765 sec/frame and the pinhole was optimally set to 0.9 μm. Z-stacks were acquired at 0.25 or 0.50 μm apart going deeper into the section or tissue. During acquisition, any X, Y or Z-axis drifts were manually corrected.

1.2. Multiphoton, multifocal structured illumination microscopy (multiphoton-MSIM)

A modified Olympus IX-71 widefield microscope was used to perform multifocal, multiphoton illumination on the SSGs in the GFP-NMIIA knock-in mice, which were a gift from Dr. Robert Adelstein (NHLBI, NIH) and both the imaging set up and the mice were described elsewhere [180]. The imaging system was entirely user designed and built on top of the backbone of a widefield microscope, and equipped to have a 3W tunable multiphoton Ti:sapphire laser (Coherent Inc.) for excitation, and a chrome-masked microlens array (Thorlabs Inc.) for multifocal beam production [181]. Prior to imaging, the GFP-NMIIA mice were fixed by cardiac perfusion, the glands were excised, sliced in half and placed in an imaging chamber with the sliced side facing the cover slip. 1X PBS maintained at pH 7.4 throughout the experiment was added to the chamber. The super-resolution images were acquired using a UPlanSApo 60x/1.20-W PSF-grade objective (Olympus America Inc.) and a #1.5 cover slip, into an Andor iXon Ultra EMCCD camera. Only secretory granules fused at the APM within an acinar cell were chosen for imaging. Specifically, the granules were selected at an angle where both the fusion pore and the region of the granule directly opposite the fusion pore could be acquired in a single frame. Z-stacks of the granules were acquired at a distance of 0.25 μm from each other. Following deconvolution, the resolution was determined to be ~155nm/pixel.

2. Animal use, preparation, development and intravital imaging

All experiments using rodents were approved by the Animal Care and Use Committee (ACUC) and the National Institute of Dental and Craniofacial Research (NIDCR) at the National Institutes of Health (NIH, Bethesda, MD). Male rats (Sprague-Dawley, purchased from Taconic), used for transfection and IVM, weighed 150-250 grams. Mice used for IVM, viral transfection and immunostaining weighed 20–40 grams. All animals were brought from the vivarium into the lab at least two days before the experiments, fed chow and water *ad libitum*. Following experimentation, each rodent was properly euthanized according to Standard Operating Procedures (SOPs).

Immunofluorescent staining and IVM was performed using a variety of transgenic, knock-in, floxed and wild-type mice. Wild-type C57 Black 6 (C57BL/6J) and Friend Virus B-type (FVB) mice were purchased from the Jackson Laboratory and were used to perform indirect immunofluorescence. FVB mice expressing GFP (GFP mice) and C57BL/6 reporter mice expressing the membrane-targeted Tandem Tomato protein (m-Tomato mice) [182] were purchased from the Jackson Laboratory and were used to determine the dynamics of secretory granule exocytosis in the acinar cells, as described previously [97]. Note, that in the m-Tomato reporter mice, the m-Tomato sequences are floxed and followed by a membrane-targeted GFP construct (mGFP). The expression of Cre-recombinase leads to the excision of the m-Tomato sequence and the expression of mGFP. In other words, after Cre expression in the cells, the red cells turn green at their plasma membranes.

The actomyosin complex recruited around the secretory granules was studied using a series of transgenic and knock-in mice expressing either fluorescently-tagged NMII

isoforms or an F-actin marker. GFP-NMIIA and GFP-NMIIB knock-in mice were a gift from Dr. Robert Adelstein (NHLBI, NIH), and were previously described [161]. Transgenic mice expressing the F-actin probe LifeAct tagged with either GFP or RFP were a gift from Dr. Roland Wedlich-Soldner (University of Münster, Germany) and were described previously [183, 184]. To study the functions of the NMII isoforms, mice floxed for NMIIA ($IIA^{fl/fl}$), NMIIB ($IIB^{fl/fl}$), and NMIIA and NMIIB ($IIA/IIB^{fl/fl}$) were obtained from Dr. Adelstein [185, 186]. In addition to the described mice, in order to study the kinetics and regulation of the secretory granules and associated molecules by IVM, the following mice were crossed (Table 3): m-Tomato/GFP, m-Tomato/GFP-LifeAct, GFP- NMIIA/RFP-LifeAct, GFP-NMIIB/RFP-LifeAct, m-Tomato/NMIIA floxed, m- Tomato/NMIIB floxed and m-Tomato/NMIIAB floxed. All the mice were bred so that the m-Tomato and the NMII genes were homozygous, and the LifeAct genes were heterozygous prior to experimentation. All mouse crosses were compared to their controls and verified to have no apparent differences in function.

Mice crossed	Resulting mice
(m-Tomato mice$^{+/+}$) x (GFP mice$^{+/+}$)	m-Tomato/GFP
(m-Tomato mice$^{+/+}$) x (GFP-LifeAct$^{+/-}$)	m-Tomato/GFP-LifeAct
(GFP-NMIIA$^{+/+}$) x (RFP -LifeAct$^{+/-}$)	GFP-NMIIA/RFP-LifeAct
(GFP-NMIIB$^{+/+}$) x (RFP-LifeAct$^{+/-}$)	GFP-NMIIB/RFP-LifeAct
(IIA$^{fl/fl}$) x (m-Tomato mice$^{+/+}$)	IIA$^{mT/mGFPfl/fl}$
(IIA$^{fl/fl}$) x (m-Tomato mice$^{+/+}$)	IIB$^{mT/mGFPfl/fl}$
(IIA/IIB$^{fl/fl}$) x (m-Tomato mice$^{+/+}$)	IIA/IIB$^{mT/mGFPfl/fl}$

Table 3. Crossed mice generated to study the assembly and function of the actomyosin complex during regulated exocytosis in the SSGs.

PCR genotyping was used to verify the genotypes of all the crossed mice. With exception of the first generation, which was verified by PCR, m-Tomato transgenes and all the other fluorescent marker proteins were verified using a genotyping flashlight (NIGHTSEA, Dual Fluorescent Protein Flashlight) and the brightest pups were chosen following each breeding cycle for further breeding or experiments, while the rest were euthanized according to SOPs. The floxed mice had to be genotyped every breeding cycle until all genes were verified homozygous, and therefore they were only bred to other homozygous mice of the same types. The LifeAct mice were bred only to wild types C57 mice of the original background.

In order to perform genotyping by PCR, a tail clip (about 1 cm in length) was taken from each mouse (preferably from ones that were 2-3 weeks old) using sterile scissors and placed into new autoclaved Eppendorf tubes. Each mouse was also clipped either at its ears

or toes to generate a code where it could be identified and linked to its own tail clip in a given Eppendorf tube; and the tubes were numerically and alphabetically labeled, as well. All records were kept in an Excel spreadsheet.

To isolate DNA from the tail clips, 600 µl of TNES (pH 7.8) was made and added along with 35 µl of Proteinase K (10 mg/ml) to each Eppendorf tube. Each tube was incubated overnight at 55^{O}C and the next morning the tube were centrifuged at 13,000 rpm for 10-15 minutes and the supernatant in each tube was carefully transferred to fresh autoclaved tubes, respectively. An equal volume of isopropanol (2-propane) was added to each tube to precipitate the DNA under a gentle vortex. The DNA was then centrifuged at 13,000 rpm for 5 minutes, the supernatant was discarded, and the DNA was then washed with ice cold 70% EtOH, allowed to dry to an extent and resuspended in DEPC treated water (Quality Biological Inc.). The DNA for each mouse was then genotyped by PCR, as described elsewhere for each mouse [161, 180, 185, 187].

For all the experiments, rodents were anesthetized by an intraperitoneal (IP) injection of a mixture of ketamine (100 mg/kg) and xylazine (20 mg/kg). After anesthesia each animal was laid flat on its back on a heated pad and the SSGs were carefully exposed, as previously described [97]. The animal was then carefully placed on the microscope stage, and the head and body of the animal was properly restrained to minimize the motion artifacts in the neck area due to heartbeat and respiration. Importantly, care was taken to ensure that the SSGs would be well positioned for imaging, as the animal laid on its side.

The SSGs were then gently extended and carefully laid flat on top of a cover slip mounted on the stage above the objective, which was heated by an objective heater (Bioptechs). The SSGs were immobilized using lens paper soaked in a carbomer-940-based

gel (Snowdrift Farms) and sometimes additionally stabilized with an added piece of plastic gently taped in place on top of the gland. Particular care was taken to make sure that the nerves and Wharton's Duct that were exposed with the gland were not damaged, and that the blood flow was not significantly reduced or halted as a consequence of excessive pressures applied to the gland during either the externalization or the immobilization procedures. This was assessed by visually looking under the microscope for any morphological changes, which would occur in the acinar cells immediately upon any external damage, and at the flow of erythrocytes through the vessels around the acini. All secretagogues were injected subcutaneously (SC) into the dorsal side of the animal and proper animal temperature was maintained to avoid biological complications during the experiment. Additional doses of anesthetic were provided after 45 minutes from the initial injection, as needed. A general flowchart of experimental procedures can be found in Fig. 27. All the experiments reported in this thesis were repeated a minimum of three times.

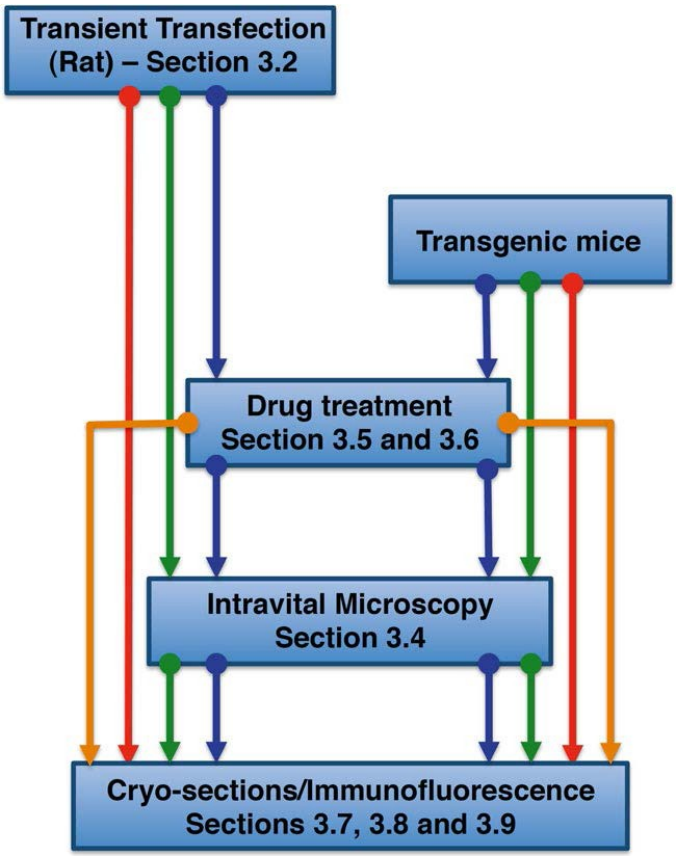

Figure 27. General flow chart of procedures for probing the roles and regulation of the actomyosin complex during regulated exocytosis in the SSGs of live rodents (for mice and rats). Rats were transiently transfected by means of cannulation with the appropriate plasmids, as described. Mice expressing the described transgenes were either imaged directly, or in the case of the floxed mice were first transfected with Cre-GFP by an adenovirus, which was delivered by cannulation and injection into Wharton's Duct. Mice were also treated by pharmacological inhibitors delivered by means of cannulation, or by bathing of the glands in the drugs. Imaging was performed during drug treatment, and subsequently the mice were either fixed by cardiac perfusion, or the glands were frozen and processed for immunocytochemistry. If imaging was not performed, the mice were just processed for immunostaining following drug treatment [96].

3. Acinar cell transfection: *in vivo* transfection and adenovirus generation

The acinar cells of rat SSGs are prone to uptake and expression of DNA plasmids when delivered by means of an *in vivo* transfection reagent (e.g. a cationic polymer-DNA mixture) or by adenovirus. In mice SSGs, only plasmids delivered by an adenovirus have proven to be effective. The protocol for *in vivo* transfection using a transfection reagent has been described elsewhere [188].

An adenovirus, serotype 5 that was able to express nuclear Cre-GFP was generated and delivered to the acinar cells of the NMII floxed and m-Tomato mice described earlier. The adenovirus plasmid was developed using the ViraPower Adenoviral Expression System, which utilizes the Gateway cloning technology (Life Technologies). During the creation of the plasmid, forward and reverse primers were synthesized to amplify just the Cre-GFP region from the pCAG-Cre:GFP plasmid (Addgene, plasmid #13776) for the subsequent BP and LR reaction with the ViraPower plasmid, as described elsewhere [189]. The plasmid was amplified in EB5α cells and purified by a CompactPrep Plasmid Maxi Kit (QIAGEN) to a high DNA concentration. In order to check the efficacy of the viral preparation, the plasmid encoding the Cre-GFP expressing adenovirus was transfected into HEK-293 cells to see if nuclear GFP was expressed 24-48 hours after transfection.

The plasmid was subsequently digested by a Pac1 endonuclease (New England Biolabs) and transfected into HEK-293a cells at 70-80% confluency in a 6-well plate using the Turbofect transfection reagent (Life Technologies) for adenovirus production. Two to three days later, the cells were trypsinized and replated on a 10 cm petri dish and allowed to grow until a 90% cytopathic effect was visible and most of the cells had detached from

the petri dish; at which point the cells and the media were collected into separate containers. The media was stored at $4^{O}C$ for no more than a week, while the cells were re-suspended in a small volume of media, put through three freeze/thaw cycles (using a $-80^{O}C$ freezer and a $25^{O}C$ water bath) until they were sufficiently lysed. The lysate was recombined with the stored media to create the final crude viral lysate (CVL). The CVL was then added to new HEK-293a cells for large scale amplification of the adenovirus in 15-25 cm petri dishes and then purified and concentrated to about $3*10^{13}$ viral particles per 5ml using a Vivapure AdenoPACK 500 kit (Sartorius Stedim, VS-AVPQ501) and stored in 100 ul aliquots at $-80^{O}C$ in a low salt physiological buffer containing glycerol. Upon use, an aliquot was thawed on ice, diluted ten times, and 30-40 µl was delivered directly to the acinar cells in each SSG of a mouse by cannulation and injection into Wharton's Duct.

4. Administration of drugs, dextrans and viral particles

Pharmacological compounds and dextrans were delivered to the acinar cells of the SSGs by one of two methods: 1) diffusion through the stroma of the glands or 2) by cannulation and injection through Wharton's Duct. Viral particles and DNA could only be delivered effectively to the cells by cannulation. Delivery through the stroma first affected the basolateral sides of the acini, while delivery by cannulation targeted the apical poles of the acinar cells, since the basolateral and apical poles of the cells are separated from one another by tight junction between adjacent cells within each acinus [95, 96, 190].

Delivery through the stroma was carried out by externalizing the SSGs, as previously described, and bathing them in the compounds (e.g. dextrans or drugs) in

custom-made wells, which hold approximately 0.5 ml and 1.5 ml of solution for mice and rats, respectively (Fig. 28). Immediately after administration of the drugs or dextrans, the glands were either fixed for immunofluorescence staining (in the case of drug delivery), or moved to the microscope for IVM (in the case of dextran administration). When the SSGs were bathed with drugs or dextrans during IVM, no change in the imaging method was applied, although the glands were bathed in a custom made chamber that was able to contain the appropriate solution around the gland during the course of the experiment. Further stabilization was needed to keep the glands stable during the imaging process, since the glands bathed in solution were more likely to slide on the coverslip generating additional motion artifacts.

Figure 28. Custom-made wells for drug delivery to the SSGs by bathing. Rat and mouse SSGs were exposed as described and a custom-made plastic well was inserted underneath the skin around the SSGs (images on the left). Rodents were fixed by cardiac perfusion while the glands were bathed with the drugs for consistency. During IVM, a custom-made well was positioned on the microscope stage and drugs were added to it during imaging (images on the right). If the rodents were fixed following IVM, the SSG was made sure to stay bathed in the drugs during the fixation procedure. Keeping the gland

stable during IVM was a major challenge, although it was possible to achieve adequate stability [96].

For delivery into the rat SSGs by cannulation, the mouth was held open by a custom-made apparatus, while a polyethylene cannula (0.008" ID x 0.020" OD, Strategic Applications Incorporated, Catalog# PE-5-100) was inserted ~0.3-0.4 cm into Wharton's Duct below the tongue using tweezers and then sealed using commercially available glue [188]. To prevent damaging the glands, the volume injected did not exceed 45-50 µl per SSG, and at a slow rate using a PHD Ultra Nanomite syringe pump (Harvard Apparatus).

Different cannulation methods and materials were used with the mice due to the much smaller diameter of their Wharton's Ducts. To cannulate a mouse, the mouth of the mouse was held open by a different custom-made apparatus. The Wharton's Ducts were located using a stereo-microscope and slightly stretched out using a highly flexible metallic cannula. Then, a tail vein catheter (BrainTree Scientific) was extended and thinned out at the tip by mechanical force using tweezers, and carefully inserted into one of the slightly stretched out ducts to a reasonable distance, at which point it was glued in place. Precautions were taken to not damage the ducts during stretching. Injections into mouse SSGs following cannulation were performed very slowly (2-5 µl/min) using the same apparatus as for the rats.

Prior to administration, dextrans were diluted to a concentration of 1 mg/ml, and the drug concentrations were as described in Table 4. All of these compounds were diluted in saline to their respective concentrations and DMSO at various concentrations was used as a delivery vehicle. After 20-45 minutes from the administration of each drug, the glands

were imaged or fixed, and the time depended on the properties of each drug and varied slightly based on how the compounds were administered.

Drug	Concentration	% DMSO	Method of administration	Target
Forchlorfenuron (FCF)	100 - 800 µM	5%	Bathing and cannulation	Inhibitor of septin functional activity
	25 µM	5%	Cannulation/IVM	
Cytochalasin D (CytoD)	10 µM	0.5%	Bathing and cannulation/IVM	F-actin depolymerization
Latrunculin A (Lat A)	10 µM	0.5%	Bathing	F-actin depolymerization
ML-7	10 µM – 1 mM	0.5%	Bathing	MLCK inhibitor
	1 µM	0.5%	Cannulation/IVM	

Table 4. Drug concentrations used to probe the role of the actin cytoskeleton during regulated exocytosis in the SSGs of live rodents.

As for the delivery of genes to the glands, DNA was mixed with a cationic polymer, incubated and injected by cannulation into the SSGs of rats, as previously described [188]. However, since this method did not work for mice, adeno-viral particles were used to deliver genes to the acinar cells in mouse SSGs. The RFP-LifeAct plasmid was a gift from Dr. Tamas Balla (NICHD, NIH) and the GFP-Septin 2 plasmid was a generous gift from Dr. William Trimble (University of Toronto, Canada); both were delivered in the same

mixture to rat SSGs for IVM, which was done 24-48 hours after transfection. Adeno-viral particles were purified and concentrated as previously described and injected into floxed mice, which were imaged and fixed ~2 weeks after gene delivery.

5. Indirect immunofluorescence

Fluorescent staining was carried out by various protocols, depending on the antibody used. In order to preserve the sub-cellular architecture of the acinar cells, the SSGs were fixed by cardiac perfusion using a solution consisting of 0.05% glutaraldehyde and 4% formaldehyde in 0.2 M HEPES buffered at a pH of 7.3. Cardiac perfusion was performed as follows: the left ventricle of the heart was punctured, saline was injected to wash out the blood (from the right atrium, which was also cut), followed by 30-35 ml of the fixative pre-warmed to 37^{O}C. Once the glands were fixed, they were excised, sliced into 150-200 μm sections in 1X PBS 7.4 using a vibratome (Leica, VT1000s), placed in fixative overnight at 4^{O}C, washed in 1X PBS 7.4, and then stained. Whole-mount staining was also performed, as previously described [94],

The immunostaining procedure following cardiac fixation involved the following steps: 1) blocking in 10% FBS and 0.02% Saponin in PBS (blocking solution) for 30-45 minutes at room temperature (RT), 2) incubation with primary antibodies in blocking solution for 2 days at 4^{O}C, 3) staining with secondary antibodies in blocking solution overnight at 4^{O}C, 4) if needed, staining with either Phalloidin or HÖESCHT, for 30-60 minutes at room temperature, and 5) mounting each section on a glass slide with a #1.5

cover slips for confocal imaging. In some cases glutaraldehyde was omitted from the fixative to improve the antigenicity of the antibodies, provided that the structure of the acini were not significantly altered.

Alternatively, fixation was done by excising the glands, embedding them in O.C.T. compound (Tissue-Tek) and freezing them in isopentane cooled in liquid nitrogen. Afterwards, 10-15 µm cryosections of the frozen tissue blocks were taken using a cryostat at -20^{O}C, adhered to silane-coated glass slides, and stained. The staining procedure involved first fixing each section by incubating it with the fixative solution described above for 15 minutes at room temperature. The staining involved the following steps: 1) incubation with blocking solution for 30-45 minutes at RT, 2) incubation with primary antibodies in blocking solution overnight 4^{O}C, 3) staining with secondary antibodies in blocking solution for 1 hour at room temperature, 4) if needed, staining with either Phalloidin or HÖESCHT, for 30-60 minutes at room temperature, and 5) mounting each section on a glass slide and sealing each section with a #1.5 cover slip for confocal imaging. All antibodies, including Phalloidin and HÖESCHT, and the staining conditions are summarized in Table 5.

Staining	**Source**	**Company/ Person**	**Dilution**	**Incubation Condition**	**Fixation Conditions**
NMIIA heavy chain	Rabbit (polyclonal)	BioLegend	1:50	2 days, 4ºC	Cardiac perfusion
				8 hours, 4ºC	Cryosections
NMIIB	Rabbit	BioLegend	1:50	2 days, 4ºC	Cardiac

heavy chain	(polyclonal)				perfusion
				8 hours, 4ºC	Cryosections
Phospho-NMII (S19)	Rabbit (polyclonal)	Cell Signaling Technology	1:50	2 days, 4ºC	Cardiac perfusion
				8 hours, 4ºC	Cryosections
Phospho-NMII (S19T18)	Rabbit (polyclonal)	Cell Signaling Technology	1:50	2 days, 4ºC	Cardiac perfusion
				8 hours, 4ºC	Cryosections
Septin 2	Rabbit (polyclonal)	Dr. William Trimble (U. of Toronto)	1:50	2 days, 4ºC	Cardiac perfusion
				8 hours, 4ºC	Cryosections
Septin 5 (SP20)	Mouse (monoclonal)	Santa Cruz Biotechnology Inc.	1:25	2 days, 4ºC	Cardiac perfusion
				8 hours, 4ºC	Cryosections
Septin 6	Rabbit (polyclonal)	Dr. Elias Spiliotis (Drexel U.)	1:50	2 days, 4ºC	Cardiac perfusion
				8 hours,	Cryosections

				4ºC	
Septin 7 (c)	Rabbit (polyclonal)	IBL America	1:50	2 days, 4ºC	Cardiac perfusion
				8 hours, 4ºC	Cryosections
Septin 9	Rabbit (polyclonal)	Proteintech	1:50	2 days, 4ºC	Cardiac perfusion
				8 hours, 4ºC	Cryosections
Myosin Light Chain Kinase (Clone K36)	Mouse (monoclonal)	Sigma Aldrich Corp.	1:50	2 days, 4ºC	Cardiac perfusion
				8 hours, 4ºC	Cryosections
Phalloidin 488	-	Life Technologies	1:400	1 hour, RT	All
Phalloidin 647	-	Life Technologies	1:200	1 hour, RT	All
HÖESCHT 33342	-	Life Technologies	1:10,000	1 hour, RT	All
All Alexa Fluor®	As appropriate	Life Technologies	1:200	1 day, 4ºC	Cardiac perfusion
				1 hour, RT	Cryosections

Table 5. Immunocytochemistry staining conditions.

To obtain information on the dose response of the glands to the treatments, fixation and staining were done in parallel using the same blocking, primary and secondary antibody mixtures for each tissue slice or section. Then, the fluorescent molecules were imaged using the same exact microscope setting for each section, after the signals were adjusted in a nearby area of the tissue to avoid saturation without adding any unaccounted-for photobleaching of the imaged sections. Direct correlations between how a drug affected a particular process at different concentrations was done by visual inspection.

6. Image processing, analysis and *in vivo* drug dose response

Quantitative information was obtained from single, stacked and time-lapse images using a series of methods, all focused on either measuring or identifying the fluorescence intensity from a given output channel within a specified region of interest (ROI), or by measuring the scalar distance between two points in each frame. Prior to quantification, all the time-lapse movies were processed by digital image stabilization, which was performed using linear alignment using the Stackreg plugin in ImageJ (NIH). Stabilization significantly minimized any distortions from motion artifacts created during IVM. Data analysis and graphing was done in Prism (GraphPad) and Excel (Microsoft), and the images were assembled in Photoshop (Adobe) and PowerPoint (Microsoft). All statistical analyses can be found in the appendix.

The diameters of the secretory granules over time were measured by taking the scalar distance between two points in each frame of the respective time series. This was

particularly done for all the floxed mice and the m-Tomato controls, as well as the m-Tomato mice in which the inhibitors (i.e. ML-7 and FCF) were applied to during live imaging, and the controls for those experiments. During processing, lines were drawn across the diameter of each secretory granule at each frame, and the length of each line was determined in microns using ImageJ [97] (Fig. 29, and as part of results). The frames in the time-lapse series were about 0.765 seconds apart from one another. The plots of secretory granule diameters over time in the floxed mice and controls were fitted by non-linear least squares using a sum of two Gaussians (f(x) = a1*exp(-((x-b1)/c1)^2) + a2*exp(-((x-b2)/c2)^2), using the curve fitting toolbox in MATLAB (MathWorks); for the controls a2 was assumed to be 0, since granule integration was linear without a second peak. In control m-Tomato mice, granule diameters were averaged at each time point and curve fitting was done in Excel.

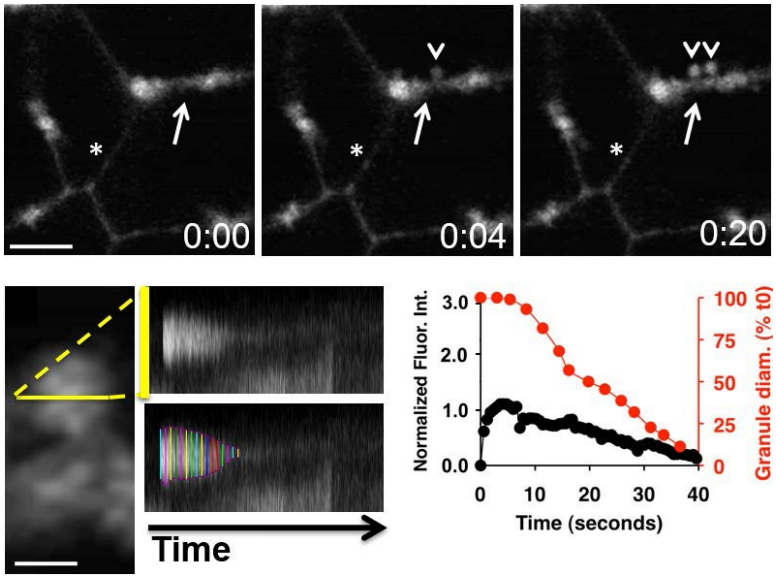

Figure 29. Measurements of secretory granule kinetics during their post-fusion integration. In this image, 10 kDa dextran was injected into the canaliculi by way of Wharton's Duct and taken up into the lumen of the secretory granules upon fusion and opening of the fusion pore. As integration occurred, the fluorescent intensity signal of the dextran decayed. Fluorescent intensity

measurements and measurements of the diameter of the dextran showed that granule integration occurred in a linear manner at a relatively constant rate. The same methods were used for the transgenes in the m-Tomato and other mice.

Measurements of the fluorescent intensity over time were used to determine the kinetics and dynamics of the recruitment of the NMII isoforms and F-actin assembly around the secretory granules, as well as their dissociations as granules integrated into the APMs of the acinar cells. For this, a ROI was defined around each granule using Metamorph (Molecular Devices) and the integrated fluorescent intensity (IFI) within that region was measured for each frame. Frames were taken about every 0.765 seconds apart and care was taken to not over-saturate any regions during imaging where the fluorescent intensity would be measured.

Lastly, the percentage of myosin light chain kinase (MLCK) per F-actin profiles vs. the controls was determined by calculating the number of MLCK profiles on top of the F-actin profiles highlighting the fused secretory granules at the apical plasma membranes divided by the total number of F-actin profiles counted, times 100%, in a field of view that was taken by the same 60x oil lens at 3.0x digital zoom where the entire field of view was comparably filled with acinar cells in which secretory granule exocytosis was occurring. Both the FCF treated samples and the controls were treated (by FCF, or DMSO) and fixed in the exact same manner, and stained in parallel.

RESULTS AND DISCUSSION

1. Development of a method based on confocal IVM to determine the kinetics of secretory granule exocytosis and its molecular mechanism

Previous studies determined that in live rodents stimulation of the β-adrenergic receptor elicits the exocytosis of secretory granules in the acinar cells of the SSGs. Specifically, secretory granules fuse and fully integrate into the APM one at a time, as they secrete their contents into the canaliculi outside the cells [13]. It was determined that the time between fusion and complete integration was relatively consistent in each rodent and appeared to occur within approximately 60 seconds [13]. In this work, I first set up a method to analyze the kinetics of this process and the machinery responsible for it. The method is based on using intravital confocal microscopy to measure the fluorescent intensities over time of various fluorescently tagged proteins expressed in mice as transgenes, as they are recruited onto, or diffuse into the secretory granules. The measurements were taken starting from the fusion step until their complete integration into the APMs.

Most of the studies carried out in this thesis were based on the use of a mouse that expresses a membrane-targeted peptide fused with the fluorescent protein Tandem-Tomato (m-Tomato mouse). This peptide, which is localized almost exclusively at the PM, is derived from the first eight N-terminal amino acids of MARCKS (Myristoylated Alanine-Rich Kinase Substrate), and it is myristoylated on the first methionine and palmitoylated

at the cysteines in positions 3 and 4 [191]. This mouse model enables imaging the secretory granules after their fusion with the PM, since the fluorescent peptide diffuses into their limiting membranes (Fig. 30).

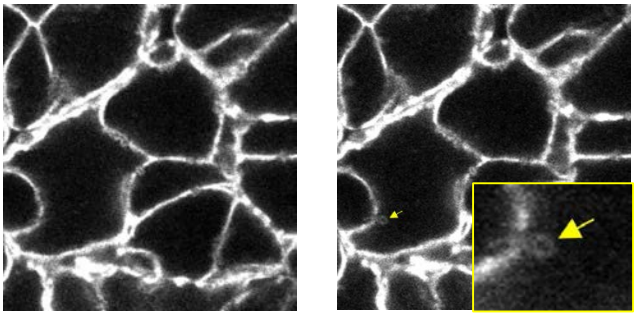

Figure 30. m-Tomato diffusion from the plasma membrane into fused granules. m-Tomato diffuses into the limiting membranes of the secretory granules fused at the APM (yellow arrow), and allows for the kinetics and dynamics of secretory granule integration to be studied during regulated exocytosis.

With respect to the procedures that were previously published by our group, some improvements were introduced. For example, it was noticed that the response to the secretory stimuli and the kinetics of the granules during exocytosis were altered when there was poor blood supply to the cells being imaged. Since the blood vessels around the acini, and the erythrocytes flowing through them can be seen in the m-Tomato mouse (as well as the other mice that express the transgenes discussed in this thesis), the imaging areas were always chosen close to a blood vessel and adequate blood flow was validated prior to each experiment. This allowed us to obtain consistent data on the kinetics and morphologies of the granules during their post-fusion integration into the APMs in each animal.

A second issue that affects the quantitative analysis of exocytic events imaged by subcellular IVM is the motion artifacts due to heartbeat and respiration. In the SSGs, a

residual xy drift in the acquired time-lapse sequences was still present, in spite of the fact that most of the motion was eliminated by properly positioning the exposed organs, as previously described [97]. This drift was eliminated by processing the raw images using the Stackreg plugin available in ImageJ and performing a rigid body transformation on frames with the greatest chance of alignment [192]. If the motion artifacts were too great, the frames were also filtered per frequency of motion, which usually corrected the distortions and enabled quantitative analysis to be performed.

After the stabilization step, regions of interest (ROIs) were drawn around the fused granules and the integrated fluorescence intensity (IFI) in each ROI was measured and expressed as arbitrary units (A.U.). Before each experiment the detectors were calibrated to avoid over-saturation of the fluorescent signals. Furthermore, since the fluorescent intensity varied from animal to animal, the IFI was normalized in order to compare different experiments. After fusion with the APM, the IFI of the molecules recruited onto the secretory granules or diffused into the granular membranes reached a peak to which a value of 1.0 was attributed. On the other hand, a value of 0.0 was attributed to the IFI in the ROI before fusion (Fig. 31).

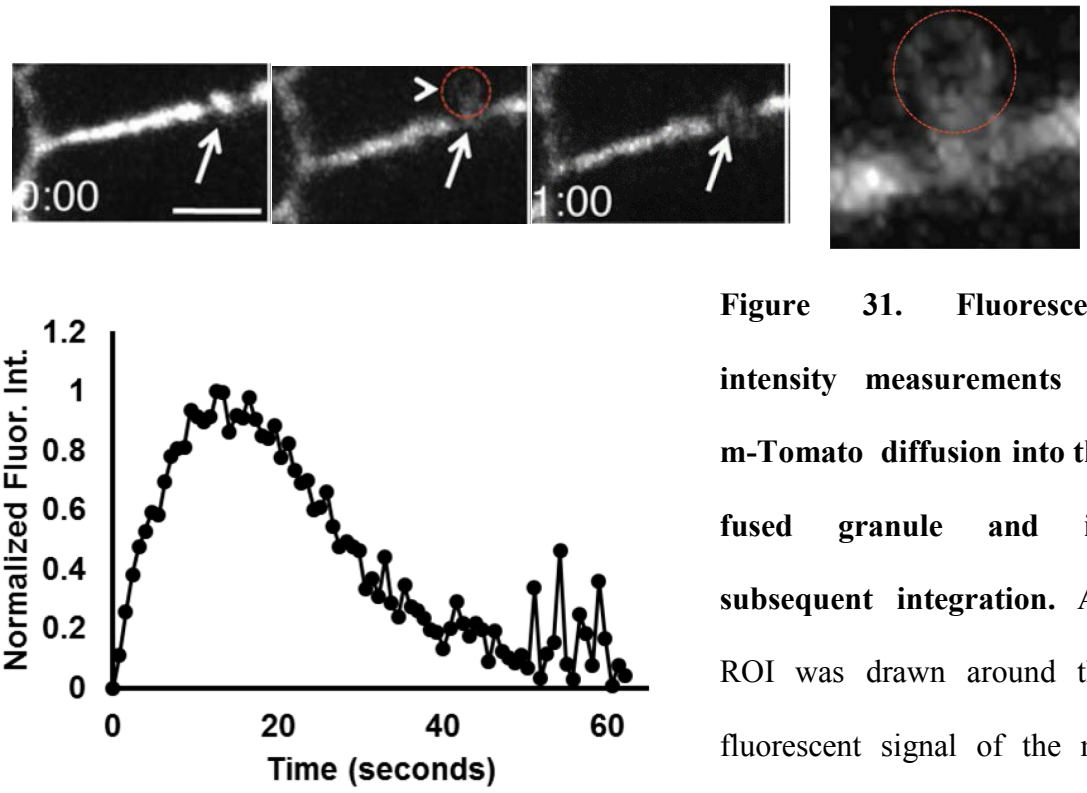

Figure 31. Fluorescent intensity measurements of m-Tomato diffusion into the fused granule and its subsequent integration. An ROI was drawn around the fluorescent signal of the m-Tomato probe that had diffused into the membrane of a fused secretory granule at the APM (red dotted circle). A plot of the integrated fluorescent intensity (IFI) signal around the granule from the beginning of fusion until its completion was made and normalized on a scale from 0.0 to 1.0.

In addition, the diameters of the secretory granules during their integration were measured to provide information on the rate of the exocytic process. For these measurements, I used either the kymograph function of Metamorph, or a line was drawn across the fused granules and their diameters were measured manually using ImageJ (Fig. 32). In the former case, a line parallel to the APM was drawn across the diameter of an individual secretory granule, and a kymograph was generated. The diameters were then outlined manually in the kymograph at selected time points, measured, and reported as a function of time.

It should be noted that the kymograph method is slightly less accurate than the manual method for measuring the rate of transgene (granule) integration. This is possibly due to the fact that while the kymograph line is stable in one position at all times, granules tend to shift slightly during integration. In addition, the exact boundaries of some granules were more difficult to identify in a kymograph, especially since the fluorescent intensity on the granules tended to fade over time and was not always equally distributed. Therefore, I preferred to manually measure the granule diameters at each time point during their integration without generating a kymograph, and this is the predominant method used in this thesis. Lastly, it should be noted that the kinetics and timing of the gradual collapse determined with the m-Tomato mice were found to be consistent with those determined using the GFP mice [97]; indicating that the m-Tomato probe did not interfere with the kinetics and dynamics of the post-fusion integration of the secretory granules.

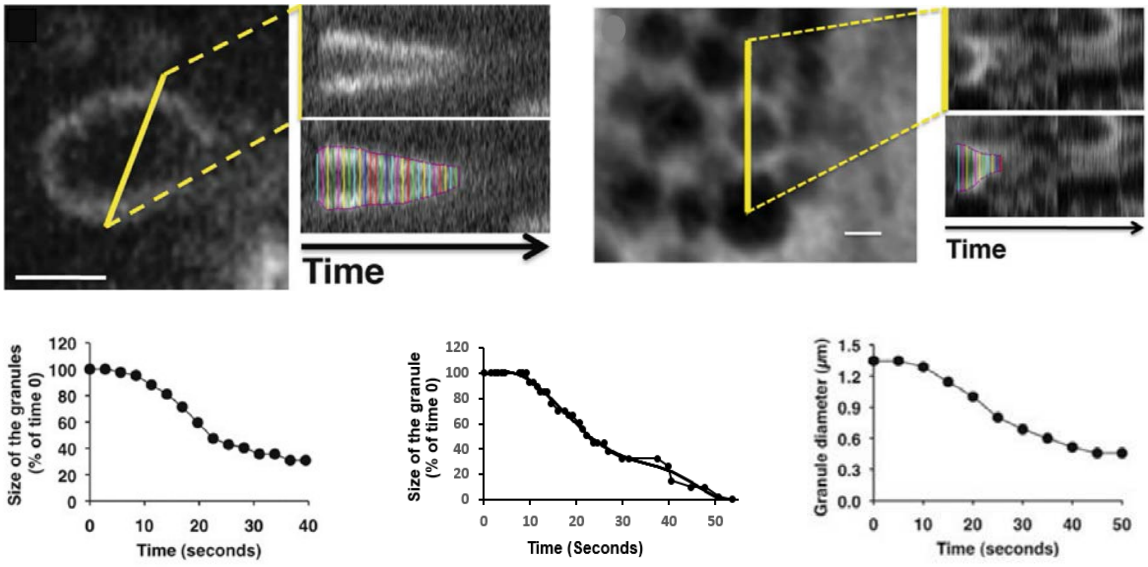

Figure 32. Measurements of granule diameters over time in m-Tomato and GFP mice show comparable kinetics. Lines were drawn across the diameters of secretory granules

in m-Tomato (left) and GFP (right) mice, and their diameters were measured over time using the kymograph method described in the text (left and right graphs, respectively). Manual measurements (middle graph) in m-Tomato mice were also taken, and were reasonably comparable to the kymograph analysis, but provided a more thorough picture. Granule diameters were also either reported as they were measured (right graph), or as percentages of their starting diameter, from 0 to 100% (left and middle graphs). Each graph represents one granule.

2. Secretory granules undergo regulated exocytosis with approximately consistent kinetics and dynamics from one animal to the next

Comparison between the measurements of the granule diameter and the m-Tomato signal overtime determined that the process of membrane integration begins after 15-20 seconds from the onset of the fusion step (Fig. 33). This delay may be an indication of the time it takes to assemble and activate the machinery responsible for driving secretory granule integration, as discussed in the next section. Notably, once started, the integration occurs mainly with linear kinetics. By measuring the fluorescent intensity of the m-Tomato signal, I determined that the signal reached its peak in a consistently linear manner at a rate of 0.062 +/- 0.012 A.U./s, and the approximate rate of integration following the peak was found to be 0.017 +/- 0.003 A.U./s. Furthermore, granule integration completed within 46.5 +/- 7.0 seconds from the start of integration (i.e. in total about 60-70 seconds post-fusion). These data were consistent with the dynamics of the secretory granules, as determined by

their granule diameter changes over time.

Indeed, we observed that the diameter of the secretory granules decreased at a constant rate of 43.2 +/- 7.5 nm/s with the linear portion of granule integration accounting for about 85% of the total process, which was completed in 37.1 +/- 3.1 seconds (Fig. 33 and 34). Furthermore, the starting average granule diameter at the time of measurement was found to be 1.58 +/- 0.19μm. During the analysis, I found a weak correlation between initial granule size and the rate of integration (Pearson correlation: 0.43); suggesting that the rate of integration is mainly a function of the inherent properties of the machinery responsible for driving the process.

The values listed above are summarized in Table 6 and will be used from now on as the background kinetic and time parameters to which to compare the activities of all proteins directly involved in secretory granule exocytosis post-fusion. Overall, these measurements confirmed that the kinetics of secretory granule integration during exocytosis were 1) mostly consistently linear in different animals, 2) occurred within a defined time range and 3) could be measured in two comparable and complementary ways (by granule diameter and marker fluorescent intensities over time). In the next section, I will begin to explore how the actomyosin complex functions in order to develop a mechanistic model of how it drives secretory granule integration. Specifically, I focus on determining the roles of two mechanoenzymes, NMIIA and NMIIB, believed to be responsible for actomyosin activity and thus, secretory granule integration.

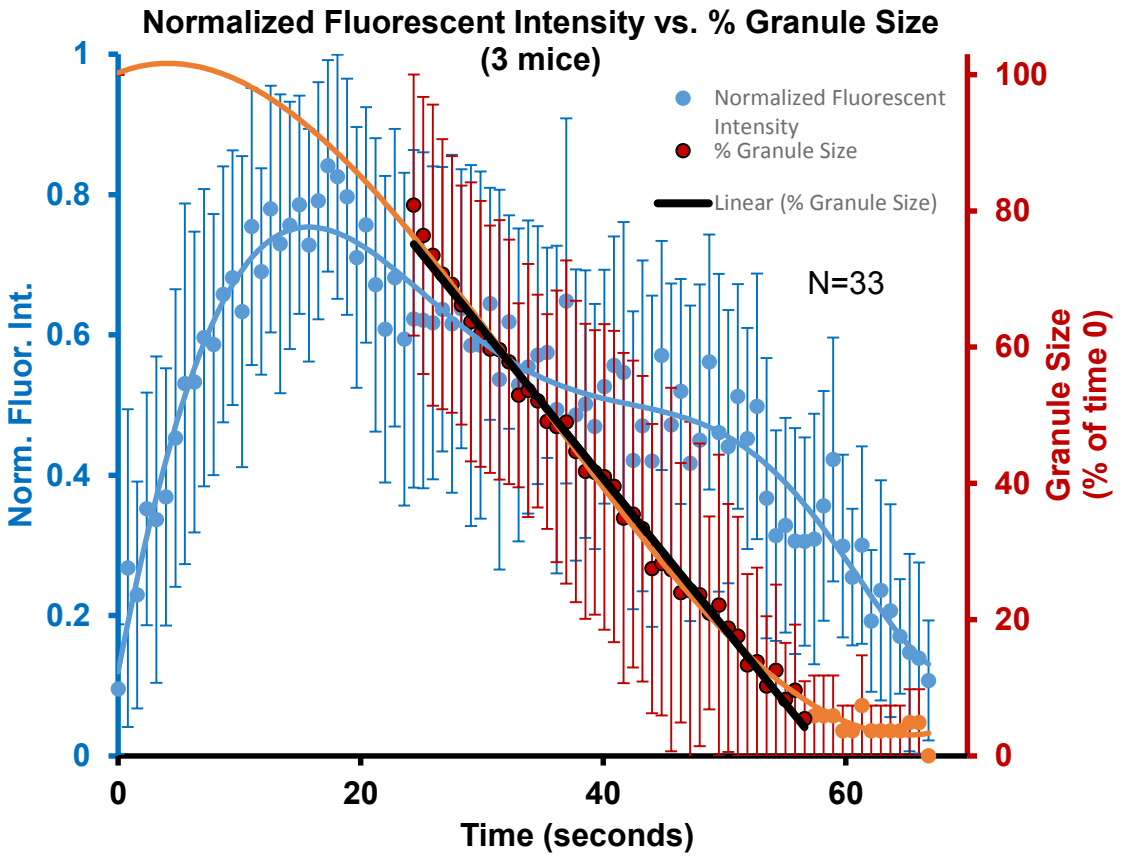

Figure 33. Normalized fluorescent intensity vs. % granules size of secretory granules during regulated exocytosis in m-Tomato mice (N=33 granules, in three animals). This plot was generated by first measuring the fluorescent intensity signal of the m-Tomato probe and subsequently measuring the diameters of the same granules over time during regulated exocytosis in three mice. Granule measurements were taken when the fluorescent signal around the granules was sufficiently strong enough to be visible around the granules, which was at some arbitrary point post-fusion. Therefore, the average fluorescent intensity of the granules, which determined the initial point of fusion was used as a marker of the time at which integration began to occur, which was around the peak of the fluorescent signal. As a result, granule diameter measurements were fit according to this starting point. Thus, it was determined that granule integration appeared to begin about 15-20 seconds

post-fusion and integrated at a constant rate from 90% of initial granule size to about 5%, on average, in about 40 seconds. The total length of the linear portion of the curve occurred over 37.1 +/- 3.1 seconds. The integration rate during the remaining seconds after the linear integration (the remaining ~5% of the granule diameters), was significantly slower.

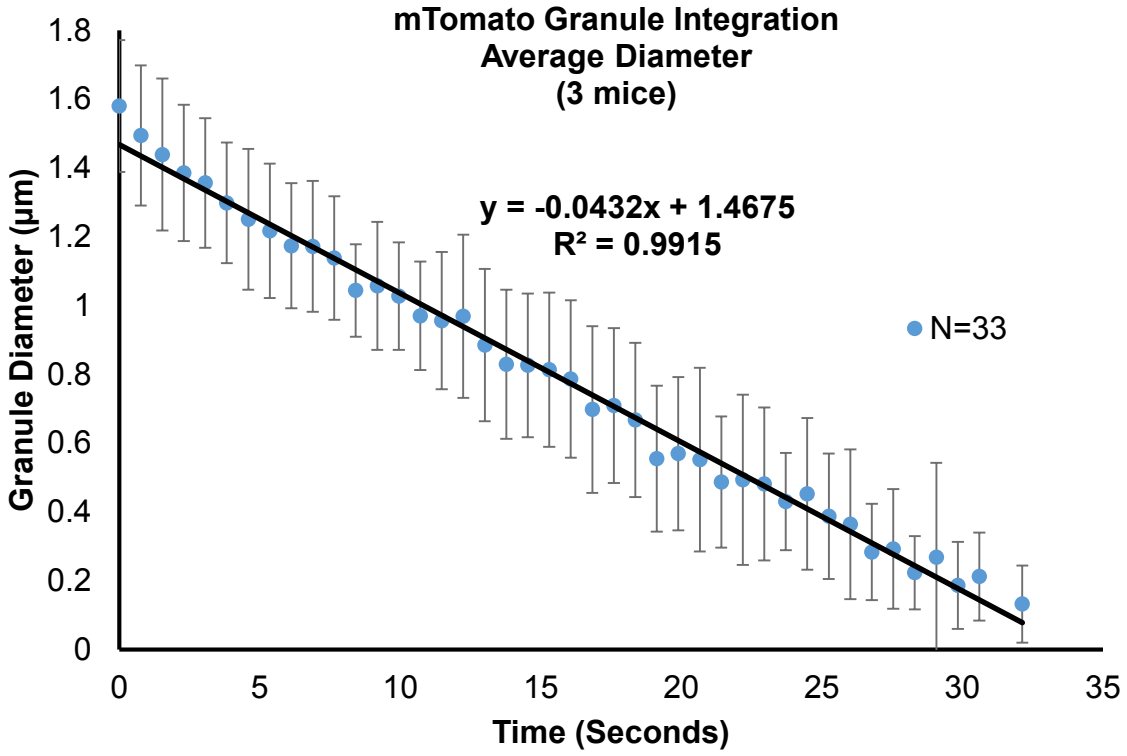

Figure 34. Granule diameters measured over time in the same three m-Tomato mice (N = 33 granules, in three animals). This plot is the measured linear portion of the average granule integration plot in Figure 33, showing that integration occurred at a constant rate of 43.2 +/- 7.5 nm/s with a starting measured granule diameter of 1.58 +/- 0.19 µm.

Measurement	Initial granule diameter	Post-fusion start of integration	Time of integration	Rate of integration
m-Tomato Fluorescent intensity	-	17 s	46.5 +/- 7.0 s	0.017 +/- 0.003
Granule diameter	1.58 +/- 0.19 µm	15 s	37.1 +/- 3.1 s	43.2 +/- 7.5 nm/s

Table 6. Average values of granule exocytosis determined in m-Tomato mice. Fluorescent intensity and granule diameter measurements over time during granule integration in m-Tomato mice determined that initial granule diameter was about 1.58 +/- 0.19 µm and their integration began 15-20 seconds post-fusion at a rate of 43.2 +/- 7.5 nm/s. Furthermore, the total integration time, as determined by the fluorescent signal around the granules was 46.5 +/- 7.0 s on average, with the last approximately 5% of integration occurring at a much slower rate than the rest of the process.

3. Conditional knock-out mice for NMIIA and NMIIB show that the NMII isoforms regulate two distinct aspects of secretory granule integration

3.1. Development and characterization of floxed NMII reporter mice

In order to test the hypothesis that NMIIA is mainly responsible for maintaining the fusion pore, while NMIIB is responsible for stabilizing the granules and promoting their gradual integration, Cre-Lox technology was used to ablate one or both proteins from the genome and compare the kinetics and dynamics of granule integration using IVM. Mice in which loxP sites flank the coding sequences of NMIIA ($IIA^{fl/fl}$), NMIIB ($IIB^{fl/fl}$), or both ($IIA/IIB^{fl/fl}$) [185, 193] were crossed with the m-Tomato mice described earlier [182] to generate $IIA^{mT/mGFPfl/fl}$, $IIB^{mT/mGFPfl/fl}$, and $IIA/IIB^{mT/mGFPfl/fl}$ mice, respectively. The m-Tomato mice are reporter $Rosa^{mT/mGFP}$ mice where the m-Tomato probe is floxed, and mGFP (membrane GFP) is expressed in its place upon its excision from the genome. All the mice were bred until all the floxed genes were homozygous, as confirmed by PCR genotyping (Fig. 35).

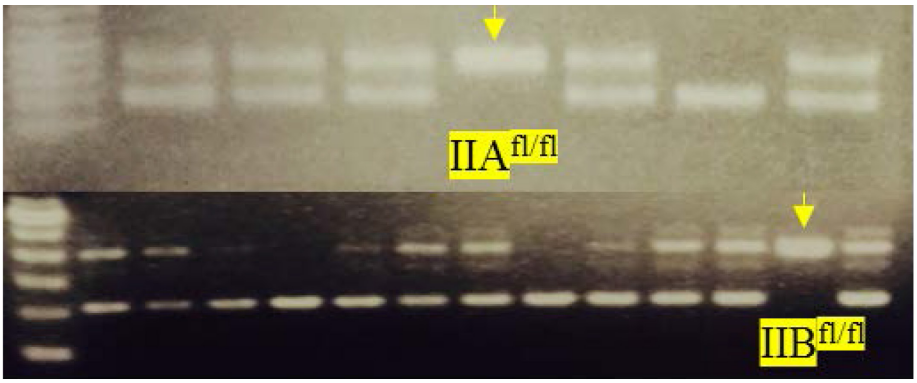

Figure 35. PCR genotyping of floxed mice confirmed homozygous NMII reporter mice. The PCR products of multiple IIA/IIB$^{mT/mGFPfl/fl}$ mice were run on 2.5% DNA gels and the mouse linked to the fifth column from the left (top gel) and the second column from the right (bottom gel) was determined to be homozygous for NMIIA$^{fl/fl}$ and NMIIB$^{fl/fl}$ (yellow arrows). NMIIA$^{fl/fl}$ and NMIIB$^{fl/fl}$ genes showed bands at 770bp and 350bp, respectively, while the wild type NMIIA and NMIIB genes showed bands at 600bp and 250bp, respectively. When both bands were seen in a column on the gel, the mouse was designated heterozygous for that gene; whereas only the upper band designated it to be homozygous floxed. 100bp DNA ladders (Life Technologies) are seen on both gels in the columns all the way to the left. Genotyping was done according to protocol, as described in the methods section. Other IIA$^{mT/mGFPfl/fl}$, IIB$^{mT/mGFPfl/fl}$, and IIA/IIB$^{mT/mGFPfl/fl}$ mice were verified to be homozygous for each of the floxed genes in the same manner and only bred to other homozygous mice of the same kind, if possible. Only homozygous mice and the ones with the brightest m-Tomato signal were used for experiments.

Nuclear Cre-GFP was inserted into an adenoviral vector, and the virus was then delivered to the APMs of the acinar cells in the SSGs of the floxed NMII reporter mice by cannulation (Fig. 36). Cells that expressed the Cre-GFP appeared in a mosaic pattern throughout the infected glands within 24-36 hours after infection (Fig. 37A). In all of the cells that expressed the mGFP, the GFP from the nuclear Cre-GFP signal was no longer visible after 2-4 days post transfection, thus leaving the targeted cells to be identified specifically by their mGFP signals.

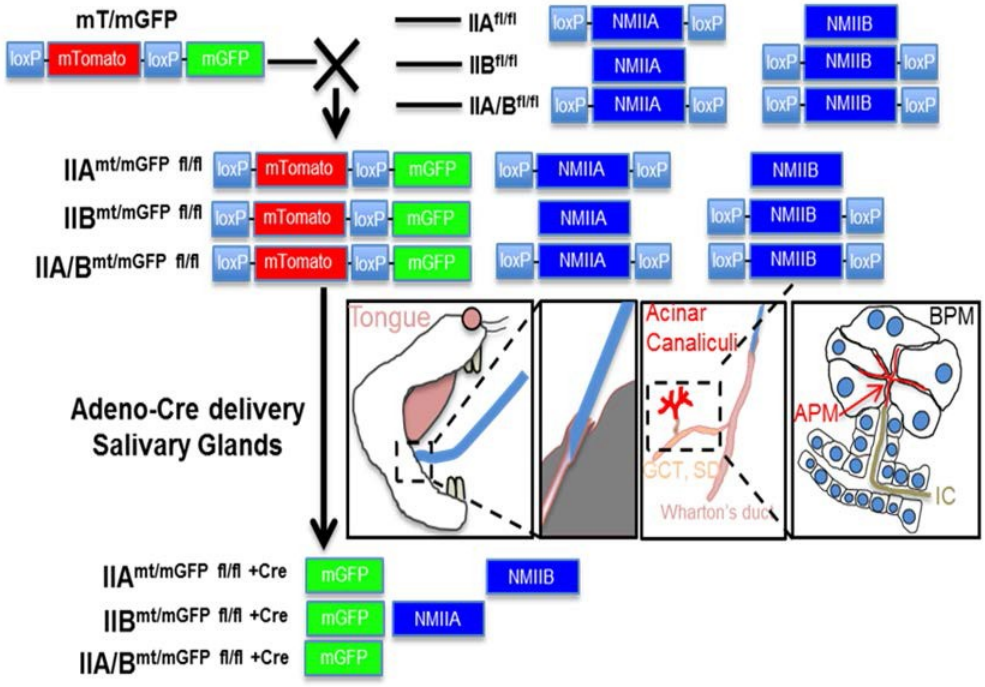

Figure 36. Generation of NMIIfl/fl mice and delivery of Cre-GFP adenovirus. $IIA^{fl/fl}$, $IIB^{fl/fl}$, or $IIA/IIB^{fl/fl}$ mice were crossed with the m-Tomato (mT/mGFP) mice to generate $IIA^{mT/mGFPfl/fl}$, $IIB^{mT/mGFPfl/fl}$, and $IIA/IIB^{mT/mGFPfl/fl}$ mice, respectively. The resulting mice were cannulated and Cre-GFP adenovirus (Adeno-Cre) was injected, as described. Expression of the Cre enzyme caused excision of the floxed genes in the respective mice.

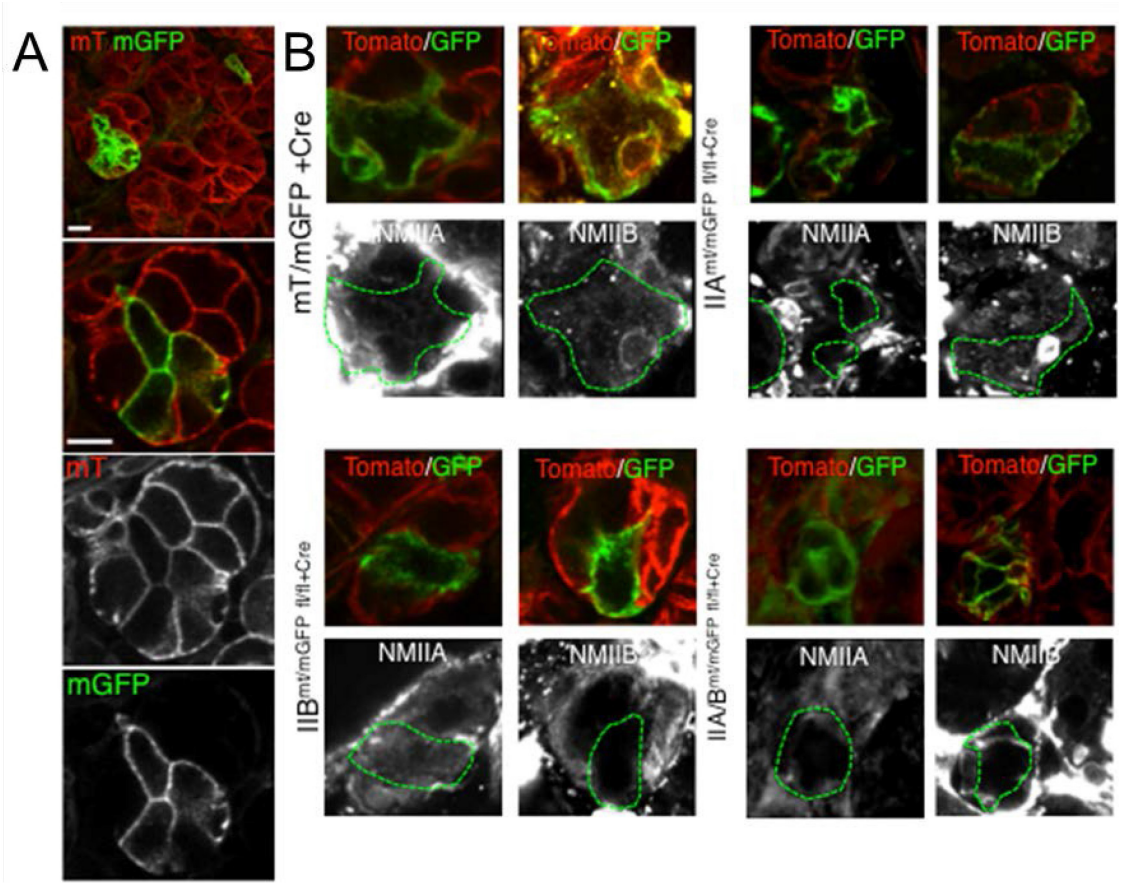

Figure 37. Delivery of Cre-GFP adenovirus to SSGs of NMII$^{fl/fl}$ mice results in a mosaic expression pattern and reduced protein levels of NMII in the respective cells. **A)** 13-15 days post-infection, Cre expression was ascertained by observing for the presence of membrane GFP (mGFP) expressing acinar cells (green) dispersed in between the m-Tomato (mT) expressing cells that were not transfected (red). Single green cells surrounded by red cells were subsequently imaged. Scale bars, 20 µm. **B)** Expression of NMIIA and NMIIB in the acini was verified by immunocytochemistry in IIA$^{mT/mGFPfl/fl+Cre}$, IIB$^{mT/mGFPfl/fl+Cre}$, and IIA/IIB$^{mT/mGFPfl/fl+Cre}$ mice 10 days post-Cre injection. Note, that the large ducts had reduced levels of NMIIA and NMIIB, while the myoepithelial cells that surrounded the acini had higher levels of both myosins. Acinar cells that expressed Cre were highlighted by the green dotted line.

In the $II^{AmT/mGFPfl/fl+Cre}$, $IIB^{mT/mGFPfl/fl+Cre}$, and $IIA/IIB^{mT/mGFPfl/fl+Cre}$ mice, Cre-GFP transfected cells exhibited significantly reduced levels of the targeted NMII proteins after 10 days from the time of injection, which was checked by immunocytochemistry (Fig. 37B). Therefore, imaging was performed within 13-15 days post-Cre injection. A longer time period in $IIA/IIB^{mT/mGFPfl/fl+Cre}$ cells resulted in the disruption of the cellular architecture, possibly due to impairments in the formation or maintenance of cell-to-cell junctions (i.e. tight or adherens junctions) [194], in addition to other phenotypic differences, such as pre-fused granules from the endogenous activities of the cells.

m-Tomato (mT/mGFP) mice that were not crossed with any of the floxed NMII mice were used as controls for the experiments. The expression of adenoviral Cre-recombinase did not affect the morphology of the acinar cells and the levels of NMIIA and NMIIB in those mice (Fig. 37 B and 38). The kinetics of granule integration into the APMs in the m-Tomato mice upon injection of ISOP was linear (Fig. 38 and Movie 1), and similar to what was previously reported in the non-transfected m-Tomato mice (Fig. 33 and 34). Furthermore, the linear granule integration rate was fitted to a Gaussian curve (for comparison with the data from the other floxed mice), and the linear part of the fitted average was measured and showed that the granules integrated at 45.2 +/- 5.3 nm/s (N=24 granules in three mice), and no granule expansion was seen to occur from a starting diameter of 1.46 +/- 0.13 μm (Fig. 38, 39 and 44). This strongly suggested that the secretory processes were not perturbed by the expression of the Cre, or by the adenovirus, since the granules integrated at a similar rate to what was reported in the non-transfected m-Tomato mice described earlier (43.2 +/- 7.5 nm/s), and with a similar starting diameter (1.58 +/- 0.19 μm).

A two-way ANOVA comparison of the starting granule diameters and rates of integration in the mT/mGFP and mT/mGFP^{+Cre} mice showed that the two are comparably similar overall (P-value = 0.31, for 24 granules each), and a one-way ANOVA on each of the factors separately (i.e. starting granule diameters, or rates of integration) for the total population sizes also showed comparability, with P-values of 0.034 and 0.78, respectively. In the latter case, the integration rates were clearly not found to be statistically different, as expected within the 95% confidence interval. However, since the P-value for the starting granule diameters was found to be less than 0.050, I've decided to set the lower P-value (of 0.030) as the threshold (instead of 0.050) for statistical comparison between the granule diameters in the Cre control (mT/mGFP^{+Cre}) mice and the diameters of all the other floxed mice using the one-way ANOVA test. The reasoning is that since the rates of integration between the granules in both the mT/mGFP and mT/mGFP^{+Cre} mice are highly similar, both in observance and statistics, it is almost with certainty that the Cre enzyme or the adenovirus did not perturb the process of regulated exocytosis, and the seemingly statistical difference seen between the granule diameters between the two types of mice (which resulted in a P-value of 0.034) may have resulted from a slight error in measurement of the granule sizes (of about 100 nm), or just a chance occurrence, which more data would confirm. In the following analyses, one-way ANOVA tests are the standard used to compare granule diameters of mice with different granule population sizes; treating the granule diameters and integration rates as two independent factors.

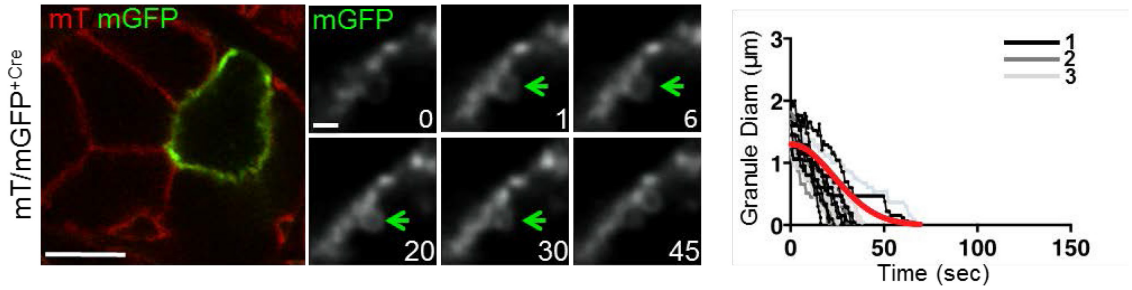

Figure 38. Membrane integration in mT/mGFP^{+Cre} mice. Left panel shows an acinar cell that expressed Cre-recombinase (green) in between other non-transfected (red) cells. Granule integration in the Cre expressing (mGFP) cell was imaged (time-series) 13-15 days after Cre transfection. Scale bars, 20 µm and 2 µm. Plot of the granule diameters over time (right) shows the kinetics of integration of the secretory granules (24 granules in three animals, as shown in the figure legend). The red curve represents the fit to a normal distribution.

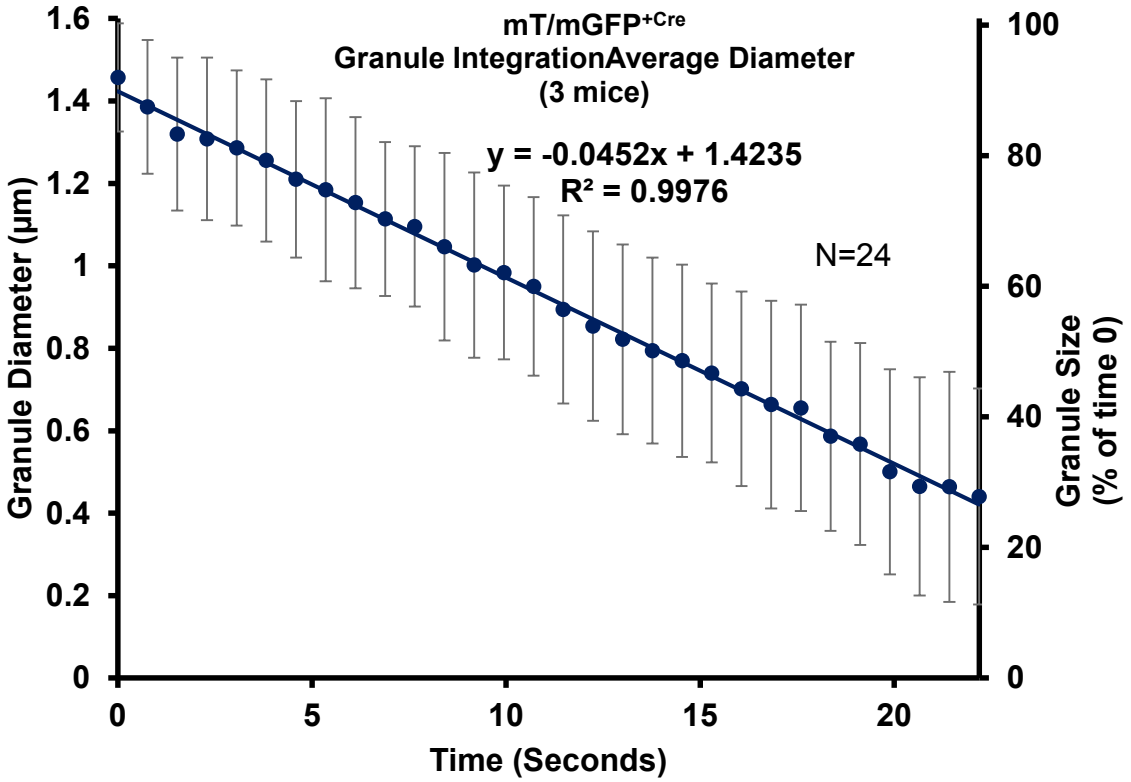

Figure 39. Granule diameters measured over time in mT/mGFP^{+Cre} mice (N = 24 granules, in three animals). This plot is the linear portion of the fitted average granule integration plot in Fig. 38, showing that integration occurred at a constant rate of 45.2 +/- 5.3 nm/s with a starting measured granule diameter of 1.46 +/- 0.13 µm.

3.2. NMIIA and NMIIB are both required for secretory granule integration

IIA/IIB$^{mT/mGFPfl/fl+Cre}$ mice were imaged 13-15 days after Cre injection into the SSGs and the diameters of the secretory granules were measured over time in the mGFP expressing cells after their fusion with the APM. Notably, none of the secretory granules integrated within the control range (Fig. 40) and around 80% of the fused secretory granules increased in diameter upon fusion. The average maximum diameter of all the

granules was found to be 2.05 +/- 0.30 µm, which was an increase of about 40 +/- 20% with respect to the mT/mGFP^{+Cre} average, and that was statistically significant (P-value = 3.1E-09 << 0.030), a similar case was seen when compared to the non-transfect control (P-value = 7.6E-09). A more detailed analysis revealed that approximately 40% (8 out of 19) of the granules went through a prolonged integration, undergoing a series of expansion and contraction cycles before fully integrating into the APMs, whereas in the remaining 60% of the granules, their integration was completely halted. Furthermore, within the latter population we observed two distinct behaviors: part of the granules initially expanded and were not able to integrate, whereas the others rapidly underwent a partial integration (approximately 50% of their initial diameters) and then stopped (Figure 40 and Movie 2).

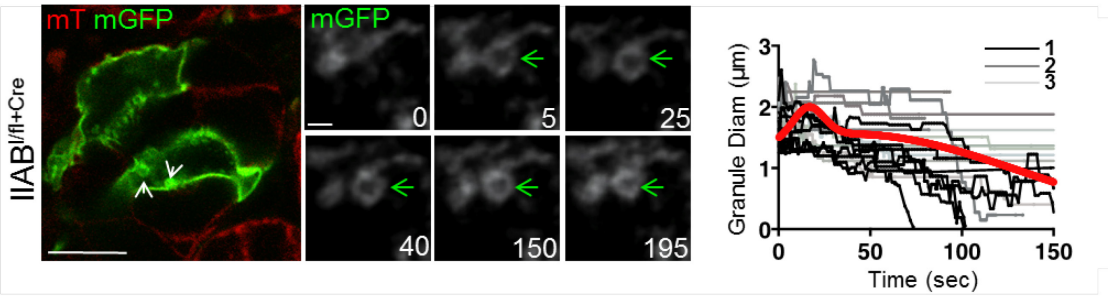

Figure 40. Membrane integration in IIA/IIB$^{mT/mGFPfl/fl+Cre}$ mice. Mice were cannulated with Adeno-Cre-GFP and imaged after 13-15 days. Time-series shows the integration of a granule upon ISOP injection in one of the mGFP expressing acinar cells depicted in the left panel. Scale bars, 20 µm and 2 µm. Plot of the granule diameters over time (right) shows the kinetics of integration of the secretory granules (19 granules in three animals, as shown in the figure legend). The red curve represents the fit to the sum of two normal distributions.

Interestingly, F-actin was still present at the APMs and on all fused secretory granules in the cells that expressed Cre (Fig. 41). Thus, the lack of both NMII isoforms does not affect the normal assembly and maintenance of the F-actin scaffold.

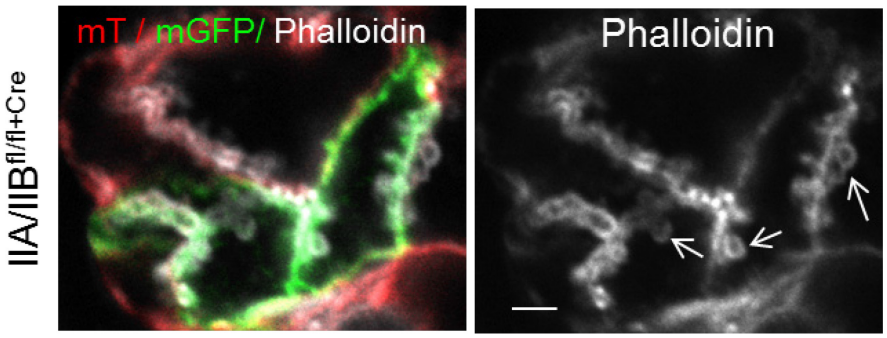

Figure 41. Immunostaining for F-actin in IIA/IIB$^{mT/mGFPfl/fl+Cre}$ mice. IIA/IIB$^{mT/mGFPfl/fl+Cre}$ mice were cannulated with Adeno-Cre-GFP, as described earlier. After 15 days, the SSGs were excised and stained for Phalloidin to highlight F-actin (grey). In both Cre (green) and non-Cre expressing (red) cells, F-actin was found present at the APMs and on the fused secretory granules. Scale bar, 2 μm.

Overall, the different phenotypes in the IIA/IIB$^{mT/mGFPfl/fl+Cre}$ mice may depend on variations in the residual levels of the NMII isoforms that may be below the detection limits of immunocytochemistry. Nonetheless, these data show a clear role for both NMIIA and NMIIB in 1) stabilizing the secretory granules (from expansion upon fusion) and 2) promoting and controlling their integration, either by direct mechanical activity, or by providing structural stability to the F-actin scaffold and the fusion pore.

3.3. NMIIA mainly maintains the fusion pore, while NMIIB stabilizes the granule and promotes its gradual integration into the APM

When NMIIA and NMIIB were ablated from the cells by expression of Cre-GFP in $IIA^{mt/mGFPfl/fl+Cre}$ and $IIB^{mt/mGFPfl/fl+Cre}$ mice, respectively, the distinct role of each NMII isoform during secretory granule integration became more apparent. In the $IIA^{mt/mGFPfl/fl+Cre}$ mice, we observed a bi-phasic behavior. Mainly in the first 15-30 seconds after fusion, the secretory granules partially integrated into the APMs (to about 50%-60% of their initial diameters) and then were abruptly halted (Fig. 42). This occurred for almost 90% of the granules (20 out of 23).

Moreover, there was no indication of granule expansion initially upon fusion, or during the process of integration. Furthermore, the average maximum diameter of the secretory granules was 1.62 +/- 0.28 μm, which was statistically similar to the maximum diameters in the control mice (1.46 +/- 0.13 μm in $mT/mGFP^{+Cre}$, see Fig. 38, 39 and 44, and 1.58 +/- 0.19 μm in $mT/mGFP^{-Cre}$, see Fig. 34), with P-values of 0.033 and 0.49, respectively. However, while the granule diameters were not different from the controls, some of the granules were observed to detach and to float inside the cells sometime after their integration was halted (Fig. 42 time-series and Movie 3). Altogether, this indicates that initial granule stabilization and integration mainly does not require NMIIA, which appears to be responsible for regulating a later step in the integration process.

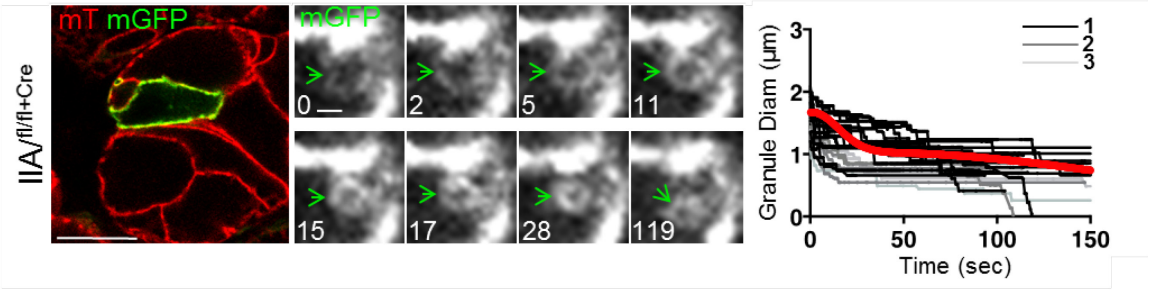

Figure 42. Membrane integration in IIA$^{mT/mGFPfl/fl+Cre}$ mice. Mice were cannulated with Adeno-Cre-GFP and imaged after 13-15 days. Time-series shows the integration of a granule upon ISOP injection. Scale bars, 20 µm and 2 µm. Right panel plot shows the kinetics of integration of the secretory granules (23 granules in three animals, as shown in the figure legend). The red curve represents the fit to the sum of two normal distributions.

On the other hand, in the IIB$^{mT/mGFPfl/fl+Cre}$ mice, the secretory granules initially expanded in diameter upon fusion (to a measured average diameter of 2.19 +/- 0.45 µm, which was around 31 +/- 30% from their starting average diameter of about 1.67 +/- 0.28 µm, and 50 +/- 30% increase from the Cre control, P-value = 5.1E-08 << 0.030) prior to undergoing a prolonged integration, which appeared to involve small cycles of expansion and contraction (Fig. 43 and 44, and Movie 4). In comparison to the non-Cre transfected control, the expansion was also significant (P-value = 3.8E-08). The initial expansion of the granules was less than what was reported when F-actin was depolymerized by Cytochalasin D (which was 110+/-30% from starting diameter) [13]. More specifically, the average maximum diameter of the granules in the IIB$^{mT/mGFPfl/fl+Cre}$ mice was slightly greater than that seen when both NMII isoforms were ablated from the cells (2.05 +/- 0.30 µm) (Fig. 40, 43 and 44). This slight difference in granule expansion, while not significantly different (P-value = 0.32 >> 0.050), may have been the result of weaker tight

junction in the IIA/IIB$^{mT/mGFPfl/fl+Cre}$ mice holding the canaliculi of the acini together, and therefore a lower hydrostatic pressure in the canaliculi acting on the granules. Furthermore, about 55% (10 out of 18) of the granules in the IIB$^{mT/mGFPfl/fl+Cre}$ mice didn't complete integration, which was on par with what was seen in the IIA/IIB$^{mT/mGFPfl/fl+Cre}$ mice (60%), and comparably, granules underwent expansion and contraction in both floxed mice, unlike when NMIIA was knocked-down.

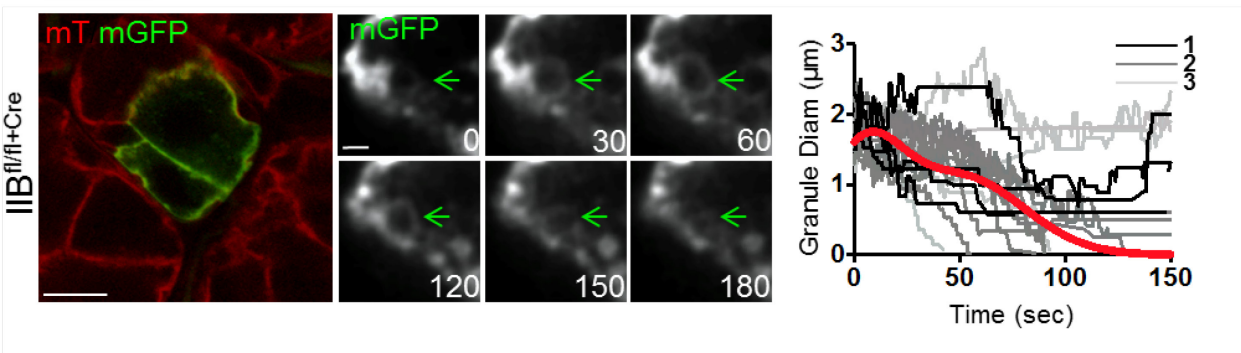

Figure 43. Membrane integration in IIB$^{mT/mGFPfl/fl+Cre}$ mice. Mice were cannulated with Adeno-Cre-GFP and imaged after 13-15 days. Time-series shows the integration of the granules upon ISOP injection. Scale bars, 20 µm and 2 µm. Right panel shows the kinetics of integration of the secretory granules (18 granules in three animals, as shown in the figure legend). The red curve represents the fit to the sum of two normal distributions.

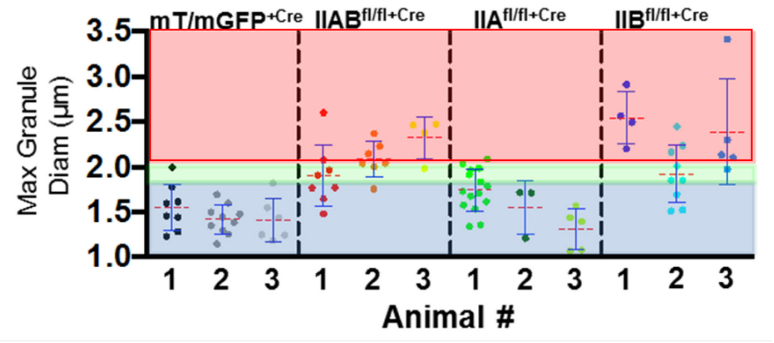

Figure 44. Maximum diameters of fused secretory granules in floxed mice. Floxed mice and controls were cannulated with Adeno-Cre-GFP, as described previously, and the cells expressing the Cre transgene were imaged by time-lapse IVM 13-15 days later. The maximum granule diameters were measured and plotted for each animal for each type of mouse. The reddish area is almost entirely composed of dots representing the maximum granule diameters in the floxed mice in which NMIIB, or both isoforms have been knocked-down.

Overall, our data support the idea that NMIIB plays a role in granule stabilization, and it is suggested that its activity is restricted to regions where stabilization and slower dynamics are involved, outside of the highly dynamic fusion pore. While, in line with what was mentioned in the previous paragraph, NMIIA appears to play a role in maintaining an open fusion pore for granule integration to occur, and based on the measured starting size of the granules, it may play only a minor role in granule stabilization and integration. In other words, there may be regions of overlap of both NMII isoforms, although NMIIB and NMIIA clearly play two distinct roles during granule integration, based on the phenotypes observed in the floxed mice: one stabilizes the granules and regulates their integration, while the other allows integration to occur to completion.

3.4. Structured illumination imaging suggests that NMIIA is localized in proximity of the fusion pore on the secretory granules

In order to visualize the distribution of NMIIA and NMIIB around the secretory granules during membrane integration we decided to use, first, time-lapse confocal microscopy. To this end we used knock-in mice, which express GFP-NMIIA and GFP-NMIIB [195, 196]. The presence of the GFP tag does not affect the localization of both proteins and it was also shown to not interfere with NMII endogenous activity [128, 180]. Indeed, under basal conditions, both GFP-NMIIA and GFP-NMIIB are localized to the APMs of the acinar cells (Fig. 45, left panels, white arrows). Moreover, upon stimulation with ISOP both NMII isoforms were recruited onto the secretory granules (Fig. 45, time-series).

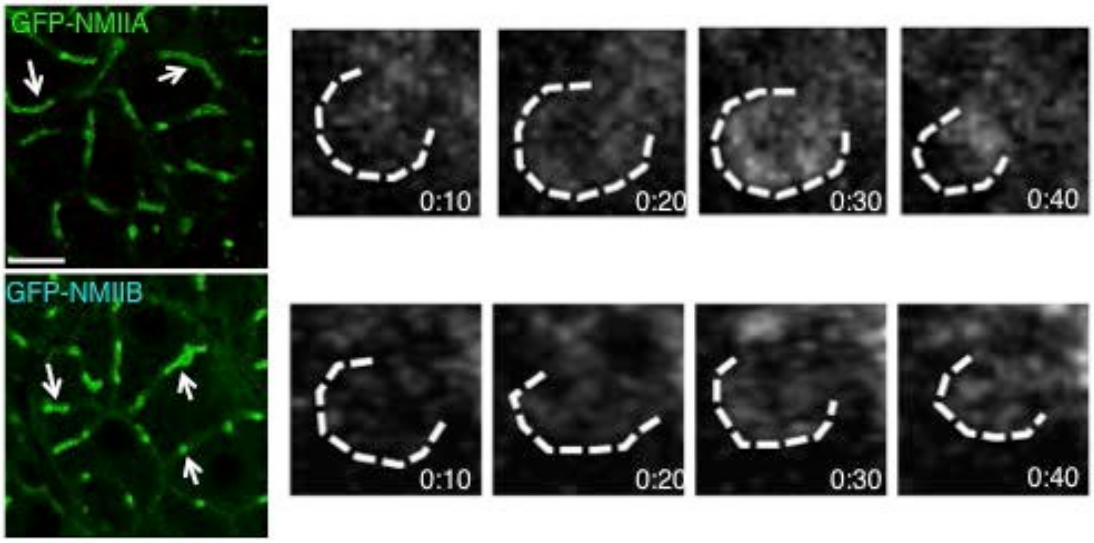

Figure 45. IVM time-series of NMII recruitment in GFP-NMII knock-in mice, shows that NMIIA localizes within proximity to the fusion pore, while NMIIB localizes around the secretory granule. In acini, NMIIA and NMIIB can be found localized at the APMs

(white arrows, left panel). Both NMIIA and NMIIB are recruited to the secretory granules (time-series, first three slide columns from the left), and appear to be redistributed to distinct regions around the secretory granules (time-series, last slides on the right). There, it appears that NMIIA is specifically active within the region of the fusion pore, while NMIIB is recruited elsewhere around the granule.

Interestingly, time-lapse imaging showed that GFP-NMIIA was localized more at the neck of the vesicle and closer to the fusion pore, whereas GFP-NMIIB was more uniformly distributed onto the granular membranes (Fig. 45, time-series). However, since confocal microscopy does not often provide sufficient resolution, due to the diffraction limit of light, we used another approach, called super-resolution multiphoton multifocal structured illumination microscopy (MP-MSIM). For the GFP fluorophore, using a standard light microscope, the resolution is about half the emission wavelength (~255 nm/pixel at its peak), at best. MSIM is a super-resolution technique that is based on exciting multiple equally dispersed foci within a given focal plane at the same time, and scanning across the field of view with that foci conformation for each frame. The array of excitation spots can then be pinholed, scaled and summed up to produce a super-resolution image. By implementing a multiphoton component to it, it was possible to image deeper into the tissue of a live rodent with better resolution than with single photon imaging [181].

The GFP signal in the SSGs was determined to be ~150 nm/pixel, which is comparable to what is expected from single photon MSIM imaging in *in vitro* cultures. In order to perform the imaging, GFP-NMIIA knock-in mice were fixed by cardiac perfusion (with a fixation mixture that included Glutaraldehyde to fix the membranes) 15 minutes

after injection of ISOP. GFP-NMIIA coated secretory granules that were oriented parallel to the focal plane were imaged so that the fusion pore and the rest of each granule could be captured in the same imaging frame, imaged by MP-MSIM, and processed. In several granules, NMIIA was present close to the fusion pore, and excluded from the opposite side (Fig. 46). We speculated that these granules may represent a later stage after fusion. Unfortunately, as a result of the multiple scans and the multiphoton nature of the beam, it was not possible to correlate the fluorescence signal with the relative concentrations of NMIIA around the secretory granules (see section 4 for such correlations). The same procedure was then attempted with the GFP-NMIIB mice. However, the levels of expression of GFP-NMIIB appeared lower in comparison to the GFP-NMIIA and due to the extensive photo-bleaching it was not possible to perform MP-MSIM on the granules in those mice.

The observations obtained by MP-MSIM and confocal microscopy, strongly indicate that NMIIA localizes to the fusion pore area of the granules during integration and in combination with the data from the floxed mice, it supports a role for this isoform in controlling the dynamics of the fusion pore. On the other hand, NMIIB appears to localize around the granular membranes and based on the data from the floxed mice, it may specifically be involved in regulating membrane stabilization and integration.

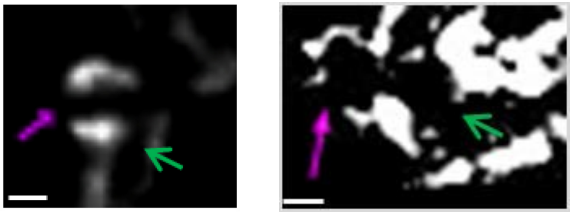

Figure 46. MP-MSIM imaging in GFP-NMIIA knock-in mice showed that NMIIA is recruited closer to the fusion pore area around the granules, but not opposite it. MP-MSIM (~150 nm/pixel), allowed for a clearer image of GFP-NMIIA around the fusion pore area and on the sides of the granules, but not opposite the fusion pore on the rest of the granule (both images). The image on the right is a maximum projection of a z-stack taken of a granule that was oriented perpendicular to the plane of imaging, while the left image is a single frame of a different granule in the same orientation. Purple arrows point to the granules, while the green arrows point to the canaliculi, which are known to be lined by NMII. Scale bars, 0.5μm.

In conclusion, it was determined that the assembly and function of an F-actin scaffold is not enough to promote secretory granule stabilization and integration without the presence of NMII isoforms A and B. Furthermore, it was determined that NMIIA localizes to the fusion pore area where it is in the ideal position to regulate the maintenance, or expansion of the fusion pore. Interestingly, NMIIA has also been reported to maintain the fusion pore in pancreatic acinar cells [40] and possibly also in neuroendocrine cells [43]. On the other hand, although we have not precisely localized NMIIB onto the granules, the findings are consistent with a role for it to stabilize the granules and promote their gradual integration into the APMs. These two distinct activities of NMIIA and NMIIB are possibly complementary and coordinated. Indeed, it is plausible that the expansion of the

fusion pore controlled by NMIIA may alter the membrane curvature at the neck of the granule; thus, facilitating the movement of the granule membrane towards the APM that is driven by the activity of NMIIB. In fact, computational modeling has shown that fusion pore expansion is proportional to the non-linear increase in the membrane integration rate [197]. More experimental work is needed to further prove this working model.

In addition, it is interesting to note that it has been found in vitro using TIRF microscopy that NMIIB bipolar filaments can translocate F-actin at a rate of 48 +/- 2 nm/s [128], which is very similar to the rate of granule integration measured in the six m-Tomato mice described thus far (i.e. 43.2 +/- 7.5 nm/s in the three mT/mGFP^{-Cre} mice, and 45.2 +/- 5.3 nm/s in the three mT/mGFP^{+Cre} mice). If the actomyosin scaffold is ideally assumed to behave as a large interconnected structure around each secretory granule (i.e. one large F-actin filamentous cage) that is driven by NMIIB, then it can be expected that the maximum rate of actomyosin contraction would be around the maximum rate at which NMIIB can translocate F-actin (i.e. 48 +/- 2 nm/s). Aside from being a possible coincidence, the consistency in this maximal average rate of integration between granules in different animals, independent of their initial diameters, suggests that the rate of granule integration is in fact determined by the inherent rate of NMIIB motor activity. Furthermore, the rate of NMIIB translocation on F-actin is significantly slower than the rate at which NMIIA has been found to translocate F-actin, which is 350 +/- 60 nm/s, based on in vitro motility assays involving wild type heavy meromyosin IIA (i.e. the fully functional N-terminal globular head of NMIIA with both light chains and a part of the coiled-coil tail) [180]. Thus, it is unlikely that NMIIA would provide the driving force for granule integration, since mostly likely the rate of integration would be proportionally greater than what we

found, or not as consistent with rate of NMIIB translocation on F-actin; leaving NMIIB to be the best candidate for the role.

As it was discussed previously, NMII drives secretory granule integration through its interactions with F-actin, which is directly linked to the membranes of the granules. The need for both NMII isoforms shows that indeed actomyosin contractile activity is the predominant (if not the only) driving force for secretory granule integration. Therefore, in the remainder of this thesis I focus on the process of actomyosin assembly, regulation and function as a whole during regulated exocytosis in the SSGs.

4. Characterization of recruitment of NMIIA and NMIIB onto the secretory granules

The kinetics of recruitment and function of the actomyosin complex during secretory granule exocytosis were determined using transgenic mice expressing fluorescently tagged LifeAct (a marker for F-actin) and knock-in mice expressing GFP tagged NMIIA and NMIIB (see Section 3, Fig. 45). In addition, these mice were crossed with each other and with the m-Tomato mice. This provided the opportunity to determine the time at which F-actin assembly and NMII recruitment began to occur after fusion.

Fluorescent intensity measurements in these mice were performed as described for the m-Tomato mice. LifeAct is a 17-amino acid peptide derived from the yeast binding protein Abp140, which has no mammalian homologues [183, 184]. It functions by binding F-actin with a very high on- and off-rate, thus avoiding to disturb the filament assembly.

The localization of LifeAct in the SSGs was found to be very similar to the endogenous F-actin, as assessed by Phalloidin staining.

Our group previously showed that ectopically transfected GFP- and RFP-tagged LifeAct (GFP-LF and RFP-LF, respectively) are recruited onto fused secretory granules in rats [13]. The same is true for mice expressing these molecules as transgenes. RFP-LF and GFP-LF (Fig. 47A) localized primarily to the APMs of the acinar cells (arrows) and to a lesser extent to the basolateral plasma membranes. Moreover, upon injection of ISOP these molecules appeared recruited onto the secretory granules (arrowheads) in close proximity to the APM (Fig. 47A time-series, and Movie 5). Furthermore, IVM in RFP- and GFP-LF mice allowed us to measure their fluorescent intensities around the granules over time as they integrated into the APMs (Fig. 47B), and it was determined that both F-actin probes reach their peak intensities around the same time (15-20 seconds), which is also around the time when the m-Tomato signal was found to reach its peak, in the respective mice (Fig. 33 and Table 6).

Also, the fluorescent intensities of both probes were found present around the granules within the control time frame of 60-70 seconds, as determined in Sections 1 and 2, using the m-Tomato mice. Further quantitative analysis allowed us to determine the half-time of F-actin assembly around the granules, as well as their kinetics of dissociation during granule integration (Fig. 47B and C, and Table 7). Both LifeAct markers had very similar half-times of recruitment to F-actin during its assembly around the secretory granules at 8 +/- 2 seconds (N=49) for RFP-LF, and 8 +/- 3 seconds (N=54) for GFP-LF in three animals each (*P*-value = 0.92). On the other hand, they varied a bit more in their dissociation half-times as the granules integrated, at 10 +/- 2 seconds for RFP-LF, and 11 +/- 4 seconds for

GFP-LF in the same mice (*P*-value = 0.052). The higher variability in their dissociation half-times is speculated to be due to the differences in the photobleaching rates (between the RFP and GFP fluorophores) and to possible diffusion limitations which may occur as the F-actin scaffold becomes smaller in size during integration, trapping some of the fluorescent probes, which would cause the region to photobleach faster than if new LifeAct molecules were allowed to diffuse in.

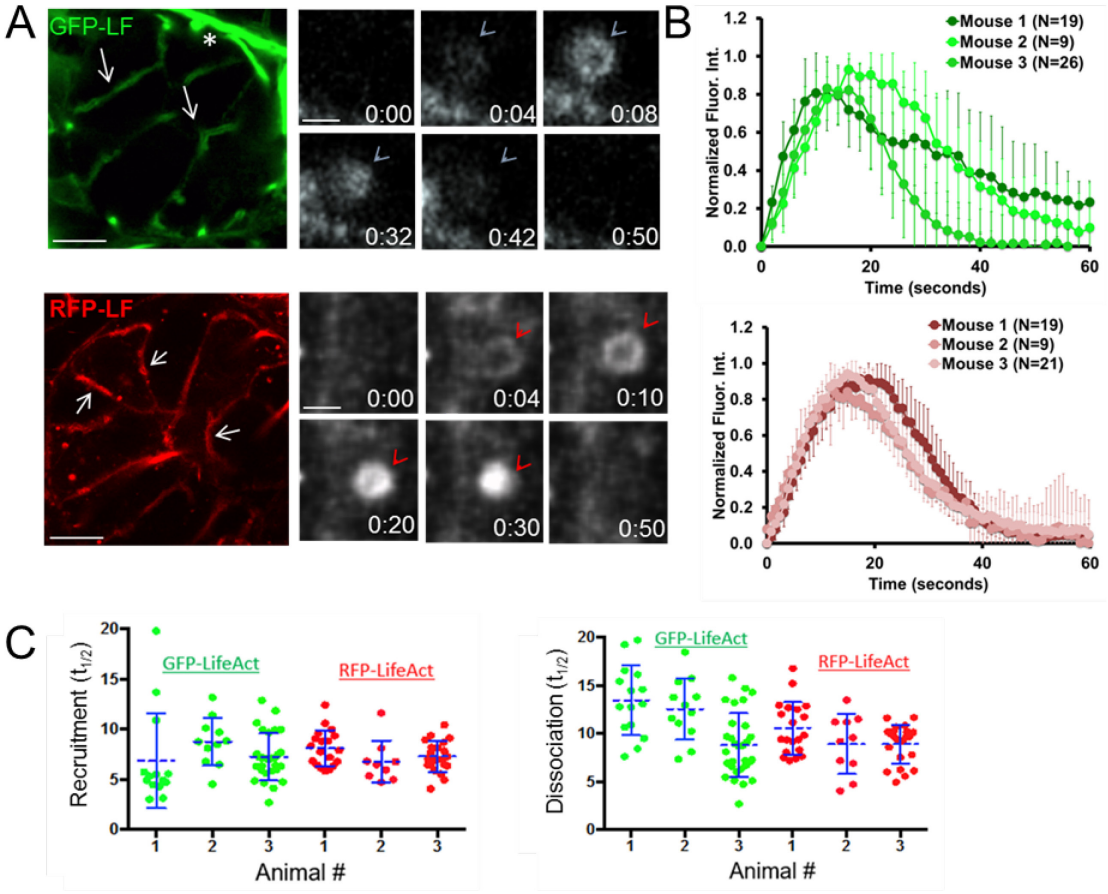

Figure 47. Fluorescent intensity curves in RFP-LF and GFP-LF mice during regulated exocytosis. A) RFP-LF and GFP-LF mice were imaged by IVM under resting conditions (left panels). Both markers are concentrated mainly at the APM (white arrows)

of secretory acinar cells. Scale bar, 20 μm. Upon stimulation of regulated exocytosis by ISOP, both marker were recruited around the fused secretory granules (time-series, arrow heads). The very bright signals in the GFP-LF mouse above the acinar cells, are the myoepithelial cells. Scale bar, 1 μm. **B)** Kinetics of recruitment of RFP-LF and GFP-LF onto the secretory granules. The IFI of either GFP-LF (upper panel) or RFP-LF (lower panel) was measured over time during each exocytic event. For each animal, the average normalized IFI was reported as a function of time. The error bars represent the standard deviations (number of total granules are in the figure legends). The experiments were repeated in three animals for each plot. **C)** From the curves derived from each secretory granule analyzed in B), the $t_{1/2}$ of recruitment onto the granules (left graph) and the $t_{1/2}$ of dissociation from the granules (right graph) were calculated and reported. Data show that F-actin assembly, as measured with both RFP-LF (red dots) and GFP-LF (green dots) occurs in a comparable manner in all the mice analyzed, with a higher variance for their dissociation (*P-value* = 0.92 for recruitment and *P-value* = 0.052 for dissociation).

In addition, in order to precisely time the recruitment of F-actin with the fusion step, mice expressing GFP-LF were crossed with those expressing the m-Tomato probe. The co-expression of the two probes did not alter the kinetics of integration of the secretory granules as shown in Fig. 48A, where granule exocytosis was seen to occur within the control time frame, and without any unexpected morphological changes of the granules (i.e. granule expansion or delays in integration) during the process. Interestingly, the GFP-LF/m-Tomato mice showed that F-actin recruitment onto the secretory granules was initiated 2.6 +/- 0.7 seconds (standard error of mean, N=21) after the appearance of the m-

Tomato in the granules (Fig. 48B and C), indicating that F-actin is assembled around the granules almost immediately upon fusion to help stabilize the granules and prevent homotypic fusion, which would result in compound exocytosis and significant granule enlargement.

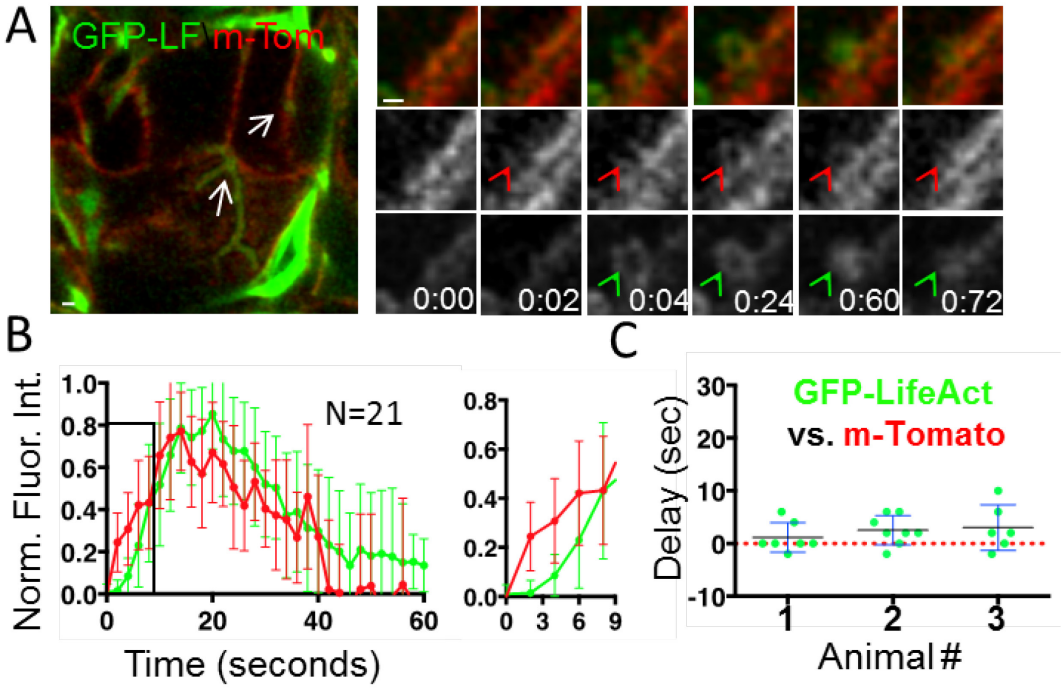

Figure 48. F-actin recruitment occurred after secretory granules fused with the APMs. A) GFP-LF/m-Tomato mice were imaged by IVM under resting conditions (left panel). GFP-LF was localized primarily at the APMs (white arrows). Scale bar, 2 µm. Upon stimulation of regulated exocytosis by ISOP, m-Tomato diffused first into the granules (red arrowheads), followed by the recruitment of GFP-LF (green arrowheads). Scale bar, 1 µm. **A)** Kinetics of recruitment of m-Tomato and GFP-LF onto the secretory granules. The IFI of both GFP-LF and m-Tomato (lower panel) was measured over time during each exocytic event and the average normalized IFI was reported as a function of time in the left plot.

The error bars represent the standard deviations (number of granules are reported in the figure legend). The curve represents one of three animals. The inset on the right shows a detail of the first nine seconds after fusion. **C)** The time delay between the appearance of the m-Tomato and the GFP-LF signals on the secretory granules was scored in three animals and reported in the graph.

In a similar manner to LifeAct, GFP-NMIIA and GFP-NMIIB were found to localize specifically to the APMs of the acinar cells, and upon injection of ISOP these molecules also appeared to be recruited onto the secretory granules in close proximity to the APMs (as shown in section 3, Fig. 45, and Movie 6). Fluorescent intensity measurements in the GFP-NMIIA and GFP-NMIIB mice determined that the two NMII isoforms were recruited to the granules at about equal rates with half-times of 13 +/- 5 seconds (N=41 granules) and 14 +/- 3 seconds (N=43 granules), respectively, for three animals each (*P-value* = 0.70) (Fig. 49). However, their rates of dissociation were found to be more variable at 10 +/- 4 seconds for GFP-NMIIA and 12 +/- 4 seconds for GFP-NMIIB (*P-value* = 0.14). Although the slight difference between NMIIA and NMIIB dissociation half-times is not statistically significant (0.14 > 0.05, in relation to a 5% confidence interval), this finding still suggests that NMIIB may be retained slightly longer on the granules to play its role in driving secretory granule integration to completion, as supported by the data from the floxed mice described earlier. The half-times of recruitment of integration in NMII knock-in and LifeAct mice are summarized in Table 7.

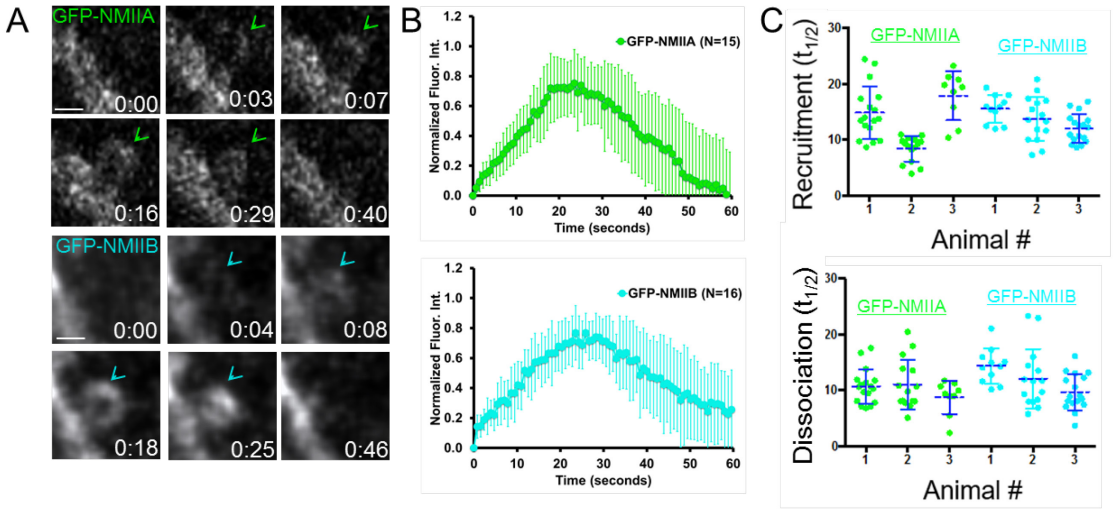

Figure 49. GFP -NMIIA and -NMIIB recruitment onto fused secretory granules. A) GFP-NMIIA (upper panel time-series, green color code) and GFP-NMIIB (lower panel time-series, cyan color code) were imaged by time-lapse IVM upon ISOP injection. Both proteins are recruited onto the fused granules at the APMs (arrowheads). Scale bars, 1 µm. **B)** Kinetics of recruitment of GFP-NMIIA and GFP-NMIIB onto the secretory granules. The IFI of either GFP-NMIIA (upper panel, green color code) or GFP-NMIIB (lower panel, cyan color code) was measured over time during each exocytic event and the average normalized IFI was reported as a function of time. The error bars represent the standard deviations (total number of granules in the figure legend). The curve represents one of three animals each. **C)** From the curves derived from each secretory granule analyzed in B), the $t_{1/2}$ of recruitment onto the granules (upper graph) and the $t_{1/2}$ of dissociation from the granules (lower graph) were calculated and reported for either GFP-NMIIA (green dots) or GFP-NMIIB (cyan dots).

	Recruitment (t½) [seconds]	Dissociation (t½) [seconds]
RFP-LifeAct (N=49)	8 +/- 2	10 +/- 2
GFP-LifeAct (N=54)	8 +/- 3	11 +/- 4
GFP-NMIIA (N=41)	13 +/- 5	10 +/- 4
GFP-NMIIB (N=43)	14 +/- 3	12 +/- 4

Table 7. Average half-times of recruitment and dissociation of RFP- and GFP-LifeAct, and GFP -NMIIA and -NMIIB (three animals each).

Previously, we reported that NMII and F-actin were found to colocalize onto fused secretory granules [13], but the extent of colocalization was never reported. Regulated exocytosis was stimulated in GFP-NMIIA mice and subsequently the mice were fixed by cardiac perfusion and stained by Phalloidin for F-actin. It was determined that 89.5 +/- 1.5% (N=1010) of fused secretory granules coated with F-actin were positive for GFP-NMIIA (Fig. 50A), and 75.2 +/- 0.65% (N=744) were positive for GFP-NMIIB, in a similar manner. These data clearly show that both NMIIA and NMIIB are localized on the same granules and do not define distinct populations. In addition, as will be shown, all RFP-LifeAct coated granules were found to have GFP -NMIIA or -NMIIB recruited to them during live imaging.

To study the dynamics of actomyosin assembly and function, RFP-LifeAct mice were crossed with the GFP-NMII knock-in mice, which showed the same morphology as the mice expressing only one probe (Fig. 50B). In these mice, GFP-NMIIA and GFP-NMIIB were mainly localized to the APMs, outlining the canaliculi (white arrows), while RFP-LifeAct was mainly present on the APMs, and somewhat on the basolateral PM also.

The major difference between the RFP-LifeAct/NMIIA-GFP mice and the RFP-LifeAct/NMIIB-GFP mice, was that the RFP-LifeAct signal was weaker in the former, although still measurable.

Analysis in the crossed mice showed that NMIIA and NMIIB recruitment was initiated 6.3 +/- 2.2 seconds (N=21) and 3.3 +/- 2.4 seconds (N=36) after the beginning of F-actin assembly, respectively (Fig. 50C). Altogether, this data indicates that it may take about 8-10 seconds after fusion for an actomyosin complex to be assembled around the granules (i.e. 2-3 seconds to initiate F-actin assembly, and about 6-7 seconds for NMIIB and 8-9 seconds for NMIIA recruitment to begin post-fusion). However, since membrane integration mainly begins at around 15 seconds, as determined in the m-Tomato mice, the additional time may be required to generate a fully functional actomyosin complex as the proteins reach their optimal concentrations on the granules, or to elicit the necessary modifications to generate contractile filaments. This supported the evidence found previously that the two NMII isoforms have different functional roles in driving secretory granule exocytosis in the SSGs.

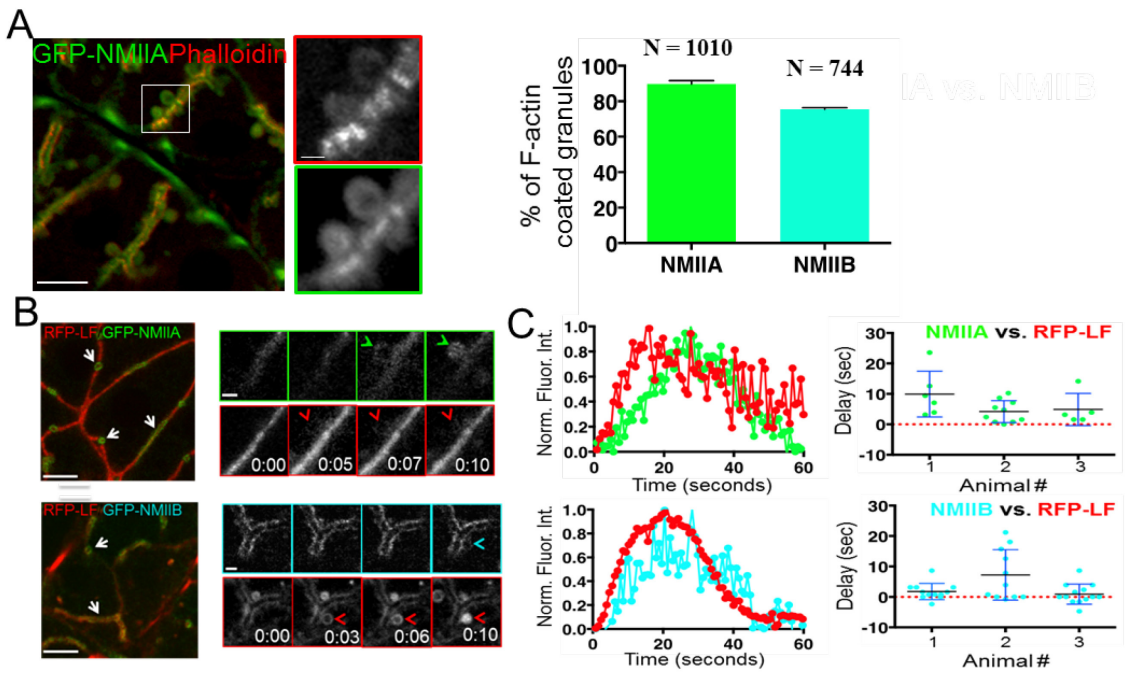

Figure 50. NMII and F-actin colocalize to the same granules but with different times of recruitment. A) Phalloidin staining in GFP-NMIIA mice (left panel), and quantification of the colocalization between F-actin and NMIIA or NMIIB during regulated exocytosis (bar graph). N=1010 and N=744, granules counted in GFP-NMIIA and GFP-NMIIB mice, respectively, in a total of three animals for each NMII isoform. Scale bars, 20 µm and 1 µm. **B**) RFP-LF/GFP-NMIIA and RFP-LF/GFP-NMIIB mice were imaged by IVM under resting conditions (left panels). Both markers are localized at the APM (white arrows) of secretory acinar cells. Scale bar, 20 µm. Upon stimulation of regulated exocytosis by ISOP, RFP-LF is recruited first (red arrowheads) onto the secretory granules, followed by GFP-NMIIA or GFP-NMIIB (green and cyan arrowheads, respectively). Scale bars, 1 µm. **C)** Kinetics of recruitment onto the secretory granules of GFP-NMIIA or GFP-NMIIB with respect to RFP-LF. The IFI of RFP-LF (red curve) and either GFP-NMIIA (upper panel, green curve) or GFP-NMIIB (lower panel, cyan curve) was measured over time during each exocytic event. For each animal, the average normalized IFI was reported as a function

of time. The curves on the left represent the kinetics of an individual granule. 26 granules for RFP-LF/GFP-NMIIA mice and 36 granules for RFP-LF/GFP-NMIIB mice were scored per animal in a total of three animals each. In the right graphs, the delay between the appearance on the secretory granules of the RFP-LF and either GFP-NMIIA (upper panel) or GFP-NMIIB (lower panel) was scored and reported.

To provide an overall picture of the integration of the secretory granules and the role of the actin cytoskeleton in this process, I have summarized in Fig. 51 the kinetics of 1) secretory granule integration, and 2) recruitment and disassembly of the actomyosin machinery, as determined thus far. In summary, granule integration appears to begin after F-actin, NMIIA and NMIIB reach a certain threshold, indicating that the actomyosin complex has to be properly assembled to become fully functional. This begins the linear and constant integration of the secretory granules that occurs between approximately 15 and 55 seconds after fusion, to near complete integration. Furthermore, we see that although NMIIB is recruited to the secretory granules a few seconds prior to NMIIA, both isoforms reach their maximum levels on the granules at the same time, while NMIIB appears to dissociate from the granules after NMIIA. This picture is consistent with NMIIB being recruited first onto the granules to provide the force that is needed for their stabilization and then to drive their gradual integration into the APMs to completion. Meanwhile, NMIIA, which is recruited slightly later than NMIIB, may be mainly responsible for maintaining and expanding the fusion pore to an irreversibly open state. We envision that initially the fusion pore may open and close, as previously shown in other systems, and that the recruitment and activation of NMIIA may induce its irreversible

expansion.

Interestingly, NMIIA and NMIIB reach their maximum levels around the secretory granules after F-actin begins to dissociate from them (Fig. 50 and 51). This suggests that the recruitment of both myosins, although temporally linked to the assembly of F-actin, may be independent from it. Moreover, it may indicate that NMII induces the depolymerization of F-actin, as shown by others during cytokinesis [113]. This would be consistent with a need to shorten the actin filaments as the granules integrate and therefore become smaller in size. It is interesting to speculate that during the integration process there is a change in the ratio of NMII molecules bound to actin filaments that dictates the robustness of the actomyosin contractile activity. However, more work would need to be done to validate this point.

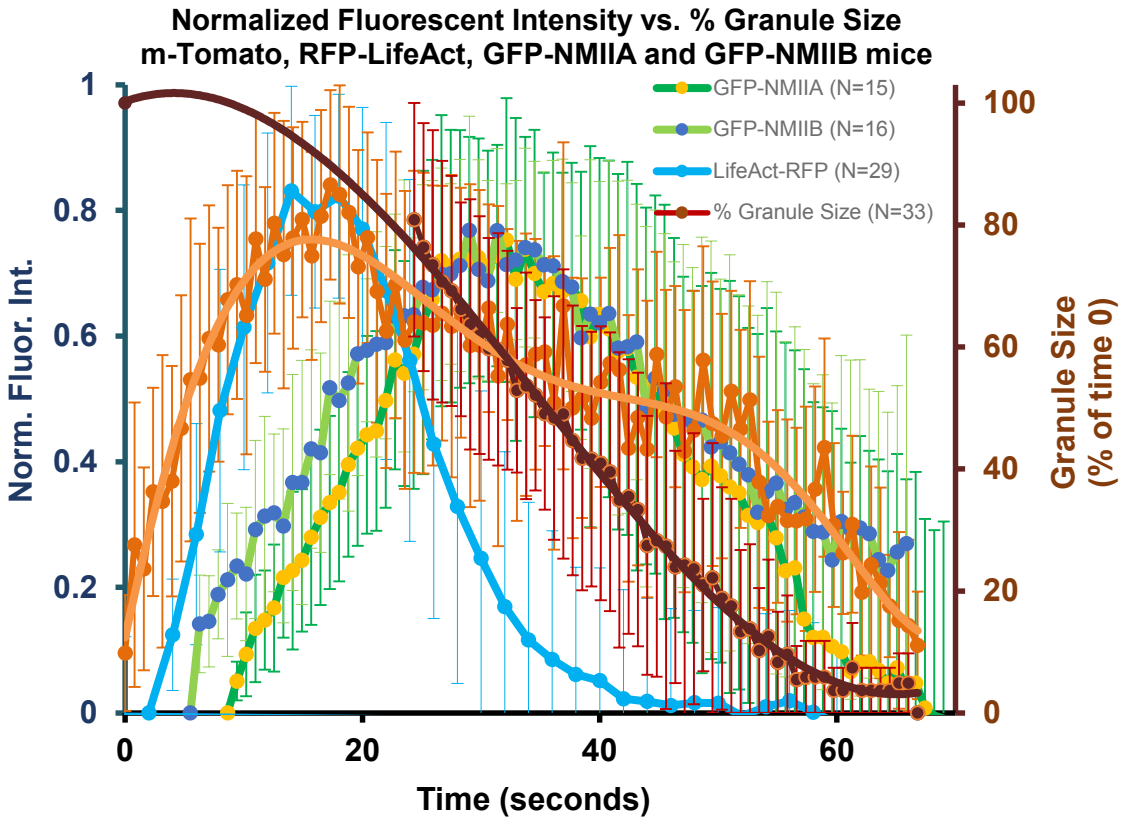

Figure 51. Summary plot of the kinetics and dynamics of secretory granule integration and of the actomyosin machinery responsible for driving the process. Fluorescent intensities from the m-Tomato, RFP-LifeAct, GFP-NMIIA and GFP-NMIIB mice described above were plotted along with the changes in average granule diameters over time that were determined from the same granules in the m-Tomato mice from which the fluorescent intensities were acquired (see Fig. 33, and 47-50). The recruitment of RFP-LifeAct and both of the GFP-NMII isoforms were offset relative to the time of fusion, as determined, and the m-Tomato signal (orange line) was used to designate the time of fusion until complete granule integration. This showed that full speed integration begins at about 17 seconds post-fusion, when the F-actin scaffold (light blue line) has fully assembled around the granules; at which point the granules begin to integrate at a constant rate (dark brown line) until near completion of the process. NMIIB (light green

line with blue dots) is recruited first to the granules to stabilize them and initiate their integration, while NMIIA (green line with yellow dots) is recruited a few seconds later and is believed to maintain an open fusion pore to allow integration to occur. The expansion of the fusion pore may also facilitate granule integration, although to a lesser. Interestingly, both NMII isoforms reach their peak concentrations at the same time, although NMIIB appears to dissociate from the granules later than NMIIA. This is possibly to drive granule integration to completion. As granule integration occurs at a constant rate, there is an increase in the concentrations of the force producing molecules (i.e., NMIIA and NMIIB) until about 30 seconds post-fusion, while F-actin shows an inverse correlation at that time. It is believed that the F-actin filaments are getting proportionally shorter as granule integration is occurring, and this may be driven by the myosins as they induce contractile activity through their motor activities, which may also promote actin filament depolymerization. Although we have used RFP-LifeAct for the plot to represent F-actin here, GFP-LifeAct, as determined earlier, would have resulted in about the same time when the peak fluorescent intensity would occur and thus, we would also see an inverse (albeit, possibly less drastic), correlation between GFP-NMII signal increase and LifeAct signal decay.

5. Regulation of NMII recruitment and phosphorylation

Since the highly-conserved motor domain of the NMII heavy chain contains a well-characterized actin-binding site [198] we reasoned that both isoforms could be recruited onto the granules, directly to the F-actin filaments. To test this hypothesis, I took advantage of a series of pharmacological tools to perturb the actin filaments, and I further used IVM and indirect immunofluorescence to stain for F-actin and NMII to see if the latter is recruited to the granules regardless of F-actin assembly.

5.1. Drug delivery to the mouse submandibular salivary glands

In the past, we used two methods of delivering drugs to the acinar cells in the SSGs: 1) by direct exposure of the glands to the drugs through bathing, or 2) by direct delivery to the APMs of the acinar cells by retro-diffusion through the Wharton's duct (i.e. cannulation). Bathing was used in mice and rats, and resulted in a homogenous response of the parenchymal cells to the drugs across the exposed surface of the glands. Although this approach is ideal when the glands are fixed and used for immunostaining afterwards, a few issues were encountered when performing time-lapse imaging while bathing. In our bathing protocol, the glands of the anesthetized animals are surgically exposed, and a custom-made well is placed within the neck area underneath the skin and around the glands to hold the drug solution at the appropriate dilution (Fig. 28). After 20-30 minutes of bathing, the animal is brought to the microscope stage and prepared for imaging. This step takes typically 5-10 minutes, and during this time the glands are not exposed to the drug.

This often affects the outcome of the experiment, especially for drugs that are rapidly metabolized and eliminated from the tissue. In addition, once the animal is set up for IVM, the gland is placed on a custom-made chamber with a cover glass at the bottom. The drug is then reapplied and this time it is primarily accumulated at the interface between the gland and the coverslip. This thin layer of fluid induces sliding of the tissue during imaging, thus significantly worsening the motion artifacts. In rats, these issues were easily solved by delivering the drugs via cannulation. However, in mice the procedure was not effective due to the smaller size of the Wharton's duct and its high sensitivity to external pressure. To solve this issue, I have developed an alternative method of cannulation. The new method required a much thinner and more flexible cannula, and a pump that would inject the solution at a slow speed (i.e. 2-5 μl/min was chosen as the rate of injection).

In order to cannulate the Wharton's ducts in mice, a small highly flexible metallic blunt-end needle was used to find the opening of the ducts visible with a stereo-microscope. Once the ducts were found, a tail vein catheter was stretched out at its end until it was extremely thin and flexible, and then it was cut to a beveled edge. At that point, it was grabbed near the tip by tweezers, and guided into the ducts just past the surface (enough to get the opening of the catheter into the ducts). Care was taken to not damage the surrounding tissue with the tweezers. Since the tip of the catheter has a tendency to regain its form after being stretched out, the procedure was done quickly and once inserted the catheter was allowed to swell in diameter slightly. If necessary histoacrylic glue was added to the interface between the ducts and the catheter in order to hold the catheter in place during the experiment. Once the catheter was stably inserted, the glands were surgically exposed and the animal was positioned on the microscope stage. The solution containing

the drug was injected with a pump, usually at 2 µl/min. In order to carefully monitor any damage and to follow the distribution of the drug, a fluorescently labeled molecule (typically a small MW dextran) was added to the solution. The localization and distribution of the tracer was followed in real time using the microscope (Fig. 52 and Movie *7*).

Interestingly, the concentration range and time frame at which a particular drug could be used on the glands of a live rodent did not always correlate with what was published for its use in cell culture, or for *ex vivo* preparations. Thus, the optimal concentration for each drug was determined experimentally for both methods of delivery to the glands *in vivo*. This resulted in the generation of dose response curves for some of the drugs. In addition, some hydrophobic drugs needed to be delivered at much higher concentrations *in vivo* compared to cell culture, and therefore required the use of different levels of DMSO above the typical 0.5%, or 1.0% used as a delivery vehicle. In our case, *in vivo* delivery of up to 10% DMSO did not show any abnormalities in the acinar cells, or in changes of the kinetics and dynamics of secretory granule integration. Furthermore, since topical applications below 50% DMSO have been found to be beneficial for wound healing with minimal to no side effects [199], we proceeded to use 5% DMSO as a delivery vehicle during some of the experiments, as necessary.

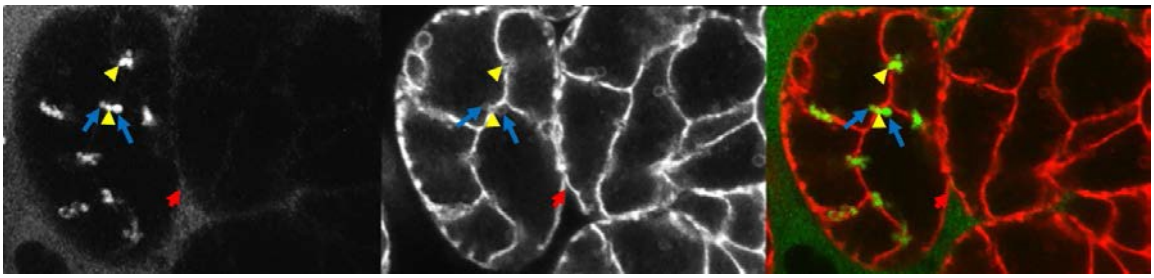

Figure 52. Administration of pharmacological compounds to the acinar cells in the SSGs by bathing the glands and retro-diffusion through Wharton's duct. SSGs of an m-Tomato mouse (membrane outlined in red channel, middle panel and red color in composite image in right panel) were cannulated and bathed with Oregon green 500 kDa dextran (green channel, left panel and green color in the composite image on the right). The green dextran diffused through the stroma to the basolateral surface of the acinar cells and outlines the acini (red arrow), but not individual acinar cells within each acinus. Green dextran delivered by cannulation entered the canaliculi and the granule in the left acinus. One yellow arrowheads point to the canaliculus that is in between two fused secretory granules (blue arrows), one from each acinar cell within the acinus on opposite sides of the canaliculus. Scale bar, 5 μm.

5.2. NMII is recruited onto fused secretory granules independently of F-actin formation

Based on existing literature, it was expected that F-actin would be responsible for NMII recruitment [200]. However, when the dynamics of the actin cytoskeleton were disrupted by administration (via bathing) of either Cytochalasin D or Latrunculin A, NMII was recruited onto the enlarged secretory granules despite the impairment of F -actin

assembly around the granules (Fig. 53A). The lack of F-actin on the enlarged granules and the APMs was confirmed by indirect immunofluorescence and Phalloidin staining, which is a very specific and robust staining for Actin filaments. Although we cannot rule out that the levels of F-actin were below the detection limits of light microscopy, the fact that the NMII recruitment onto the granular membranes was not affected by the severe disruption of the cytoskeleton assembly clearly indicates that this process occurs in an F-actin independent manner. When the m-Tomato mice were treated with 10μM Cytochalasin D administered by cannulation, the phenotype in the glands was less severe and more heterogeneous (Fig. 53B). Indeed, within the same acinar cells we observed both enlarged granules lacking F-actin and normal secretory granules coated with F-actin. As expected, both population of granules were coated with NMII regardless of the levels of F-actin.

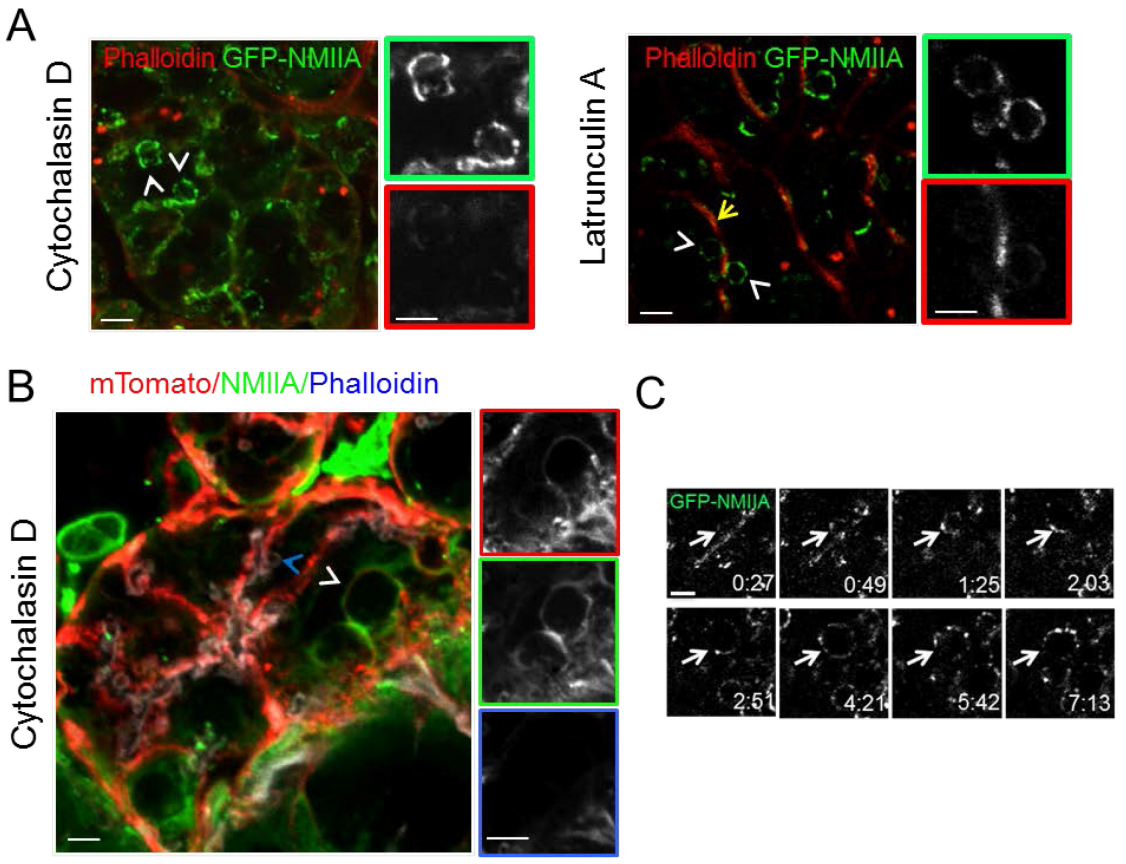

Figure 53. NMII is recruited to the secretory granules independently of F-actin polymerization and assembly. A) 10 µM Cytochalasin D and 10 µM Latrunculin A, respectively, were administered to the acinar cells in the SSGs of GFP-NMIIA mice by bathing the glands in the drugs for 20 minutes. Regulated exocytosis was stimulated by a subcutaneous injection of ISOP, and after 5-10 minutes the animals were fixed by cardiac perfusion, and the glands were stained for F-actin by Phalloidin. GFP-NMIIA was found on the enlarged granules at the APMs, which did not label for F-actin (white arrowheads). Yellow arrow point to the basolateral PM adjacent to the granules and the APM where they were fused in the Latrunculin A treated gland, which did not depolymerize. Scale bars, 5 µm. **B)** SSGs of m-Tomato mice were cannulated with 10 µM Cytochalasin D, resulting in a heterogeneous response to the drug. After a 20 minute incubation period, the glands were

processed as in A) and stained with Phalloidin and an antibody against NMIIA. NMIIA was recruited to both the normal and enlarged granules regardless of the presence of F-actin (blue and white arrowheads, respectively). Scale bars, 3 μm and 5 μm. **C)** IVM of GFP-NMIIA mice following 20 minutes of incubation with 10 μM Cytochalasin D and after stimulation with ISOP. The granules expanded in size due to a lack of F-actin scaffold formation, GFP-NMIIA was recruited to the granules and stayed on them in discreet patches as they expanded (arrow). Scale bar, 3 μm.

Similar experiments with NMIIB-GFP mice were inconclusive due to an unexpected reduction in the total fluorescent signal. However, since both NMIIA and NMIIB have very similar rates of recruitment to the granules and possess highly conserved N-terminal globular heads that bind to and translocate on F-actin, it is reasonable to assume that they are regulated in the same manner. Furthermore, it has been shown by others that the NMII isoforms are recruited to overlapping regions only if their motor activities are not activated. Thus, it can be assumed that both NMII isoforms are recruited to the secretory granules in an inactive state independently of F-actin formation and that both isoforms would later be redistributed to the F-actin scaffold to carry-out their specific roles.

In support of this, time-lapse imaging in mice treated with 10μM Cytochalasin D showed that GFP-NMIIA was recruited onto the secretory granules in discrete patches as they expanded (Fig. 53C time-series, and Movie 8), whereas in the untreated mice, GFP- NMIIA was seen to coat the granules more uniformly (Fig. 45, 49A and 50B time-series, and Movie 6). Therefore, on the granular membranes, NMII recruitment and activation appear to be two independent processes. This is in contrast to what is reported

in the literature, where NMII is recruited in an F-actin dependent manner, possibly in a pre-activated state. Both cases may occur, however it may depend on the particular process that the NMII isoforms are regulating. In the SSGs during regulated exocytosis, our data are consistent with a main role for F-actin to promote the assembly of NMII bipolar filaments at specific locations on the F-actin scaffold following NMII recruitment to the granules independently of F-actin.

5.3. NMII isoforms are activated by phosphorylation of their regulatory light chains solely by myosin light chain kinase (MLCK) in an F-actin dependent manner

It is well known that prior to activation of the NMII isoforms by the phosphorylation of their RLCs at Serine 19 and/or Threonine 18, they are held as inactive dimers in a 10S conformation, where their C-terminal tails are folded over their N-terminal heads [115]. In this conformation, their ATPase activity cannot function and bipolar filaments cannot be assembled, which prevents any cross-linking or mechanical activities. These observations have been shown *in vitro*, and a variety of activating kinases are known to regulate NMII activity in cell culture.

First, I wanted to check whether the NMII RLCs are phosphorylated around the secretory granules during regulated exocytosis. To this end, wild type (C57BL/6J) mice were fixed by cardiac perfusion, sectioned on a vibratome and stained for the mono- and di-phosphorylated forms of the NMII RLCs. Under resting conditions both of them w e r e found at the APMs, but not on the granules (Fig. 54A and B). This was expected in order

to maintain a functional actomyosin complex that should serve as a functional barrier to limit basal exocytosis. However, after ISOP stimulation for 10-15 minutes, both phosphorylated forms were found on the fused secretory granules (Fig. 54C, left and middle panels).

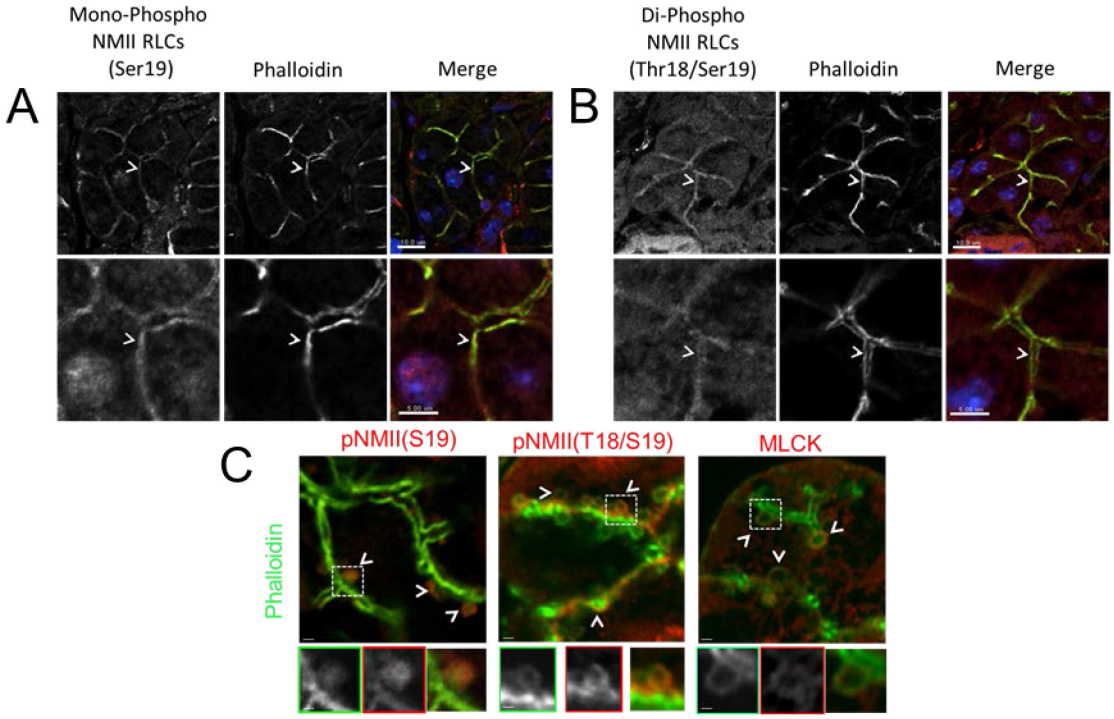

Figure 54. NMII RLCs are mono- and di-phosphorylated on the fused secretory granules by MLCK. An antibody raised against the mono- and the di-phosphorylated forms of human smooth muscle myosin RLCs mono- and di-phosphorylation was used in the SSGs that were fixed and processed as described in the text. It was found that MLCK is solely responsible for phosphorylating NMII RLCs in the SSGs. **A)** NMII RLCs are mono-phosphorylated at S19 and **B)** di-phosphorylated at S19T18 at the APMs prior to stimulation of regulated exocytosis, but not on the secretory granules (white arrowheads, bottom panels are enlargements of top panels). Scale bars, 10 µm and 5 µm, top and bottom

panels, respectively. **C)** Upon stimulation of regulated exocytosis by a subcutaneous injection of ISOP, both mono- and di-phosphorylation of NMII RLC pNMII(S19) and pNMII(T18S19), respectively) were observed around the secretory granules (arrowheads, left two panels). Myosin light chain kinase (MLCK) was also found recruited to the fused secretory upon stimulation of regulated exocytosis (right panel). Scale bars, 5 μm and 1μm (insets).

Interestingly, when F-actin was disrupted by the administration of 10 μM Cytochalasin D (either by cannulation or bathing), NMII phosphorylation was blocked (Fig. 55A). Thus, NMII activation occurs in an F-actin dependent manner. This finding combined with our previous data suggests the following working model: 1) after fusion of the secretory granules with the APMs, an F-actin scaffold is assembled onto the granule membranes; 2) after a slight delay, NMII isoforms are recruited onto the granules independently of F-actin and possibly in an inactive conformation; 3) the NMII isoforms would then be redistributed onto the scaffold where they would interact either directly or indirectly with the F-actin filaments, which may also serve as docking sites for the kinase(s) responsible for the phosphorylation of the RLCs and, as previously reported, for the activation of NMII ATPase/motor activity [201]. This cascade of events would also lead to the formation of fully functional NMII bipolar filaments, which would directly interact with actin filaments through their N-terminal globular heads, to cause contraction of the F-actin scaffold in order to drive secretory granule integration.

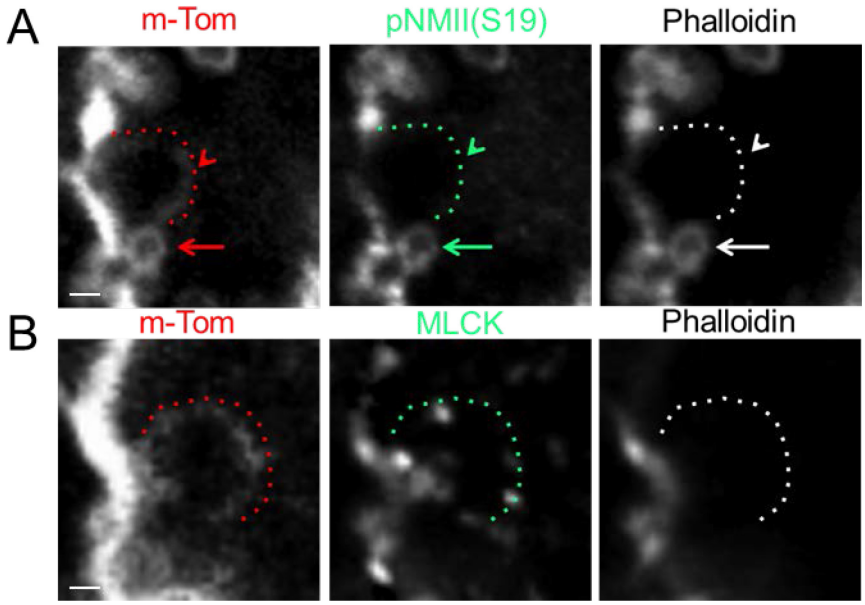

Figure 55. NMII phosphorylation and activation occurs in an F-actin dependent manner on the secretory granules. A) m-Tomato mice were cannulated with 10 µM Cytochalasin D for 15-20 minutes, stimulated by ISOP for 5-10 minutes, fixed by cardiac perfusion, excised, sectioned and stained for pNMII (S19) and Phalloidin for F-actin. Cannulation caused a heterogeneous response to the drug, where a normal sized granule with a full actin coating was found at the APM (red and white arrow, in the left and right panels, respectively) next to an enlarged granule with no F-actin coating on it (red and white arrowheads and dotted lines, in the left and right panels, respectively). The m-Tomato probe highlighted both granules. The normal sized granule coated with F-actin also had pNMII (S19) on it (green arrow, middle panel), while the enlarged granule with no F-actin coating did not have NMII that was phosphorylated at its RLCs recruited to it (green arrowhead and dotted line, middle panel). Scale bar, 1 µm. **B)** In a similar manner, enlarged granules were not decorated by F-actin and MLCK. Scale bar, 1 µm.

Based on these findings, I sought to determine whether any of the kinases known to phosphorylate NMII RLC were implicated in regulated exocytosis in the SSGs. The most obvious candidate to investigate was the Myosin Light Chain Kinase (MLCK), which in other secretory systems has been shown to play a role during secretion although, in different steps [202]. By using indirect immunofluorescence, I observed that MLCK is localized onto the secretory granules after Isoproterenol stimulation (Fig. 54C), whereas under control conditions it is known to be cytosolic and can also be found at the plasma membrane. In addition, similar to phosphorylation of NMII RLCs, MLCK was also found to be recruited to the secretory granules in an F-actin dependent manner (Fig. 55B). In agreement with our working model, this showed that F-actin, while not necessary for the recruitment of NMII to the granules, is indeed required for the recruitment of a NMII regulating kinase, and thus it can directly or indirectly regulate actomyosin contractile activity in this manner.

Furthermore, inhibition of MLCK activity by bathing the glands in ML-7 and staining for phospho-NMII RLCs in either GFP or C57BL/6J mice, respectively, showed a dose dependent inhibition of the RLC phosphorylation (Fig. 56A). At the highest dose (100μM ML-7), RLC phosphorylation, but not NMII recruitment, was completely abolished suggesting that MLCK is the only kinase recruited to the secretory granules that is responsible for NMII activation (Fig. 56B). Furthermore, time-lapse imaging of m-Tomato mice treated with 1μM ML-7 delivered by cannulation, showed a delay in the integration of the secretory granules into the APMs of the cells, which occurred at around 82 +/- 56 seconds (23 granules in three mice) compared to the controls (0.5% DMSO) where granule integration occurred in about 33 +/- 8 seconds (32 granules in three mice);

which was about a 148% +/- 170% increase over the controls (*P-value* = 1.27E-05 << 0.05, one-way ANOVA). Since the drug was delivered by cannulation, the response was heterogeneous, and therefore such wide variability was expected. Regardless of the variability, a clear and significant effect in the delay in integration of the secretory granules was seen, which confirmed that MLCK activity is necessary for NMII activation and thus, secretory granule exocytosis. In addition, the granules during integration reached a maximum average diameter of about 2.11 +/- 0.51 μm, which was about a 33% +/- 33% increase compared to the control granules that integrated with a maximum average diameter of 1.58 +/- 0.19 μm (*P-value* = 2E-06 << 0.05; one-way ANOVA), and is consistent with the impairment in the function of both NMII isoforms (Fig. 56C). Altogether, this shows that MLCK is recruited to the secretory granules in an F-actin dependent manner in order to activate actomyosin contractile activity through the phosphorylation of the RLCs of NMII on both isoforms at Serine 19 and Threonine 18.

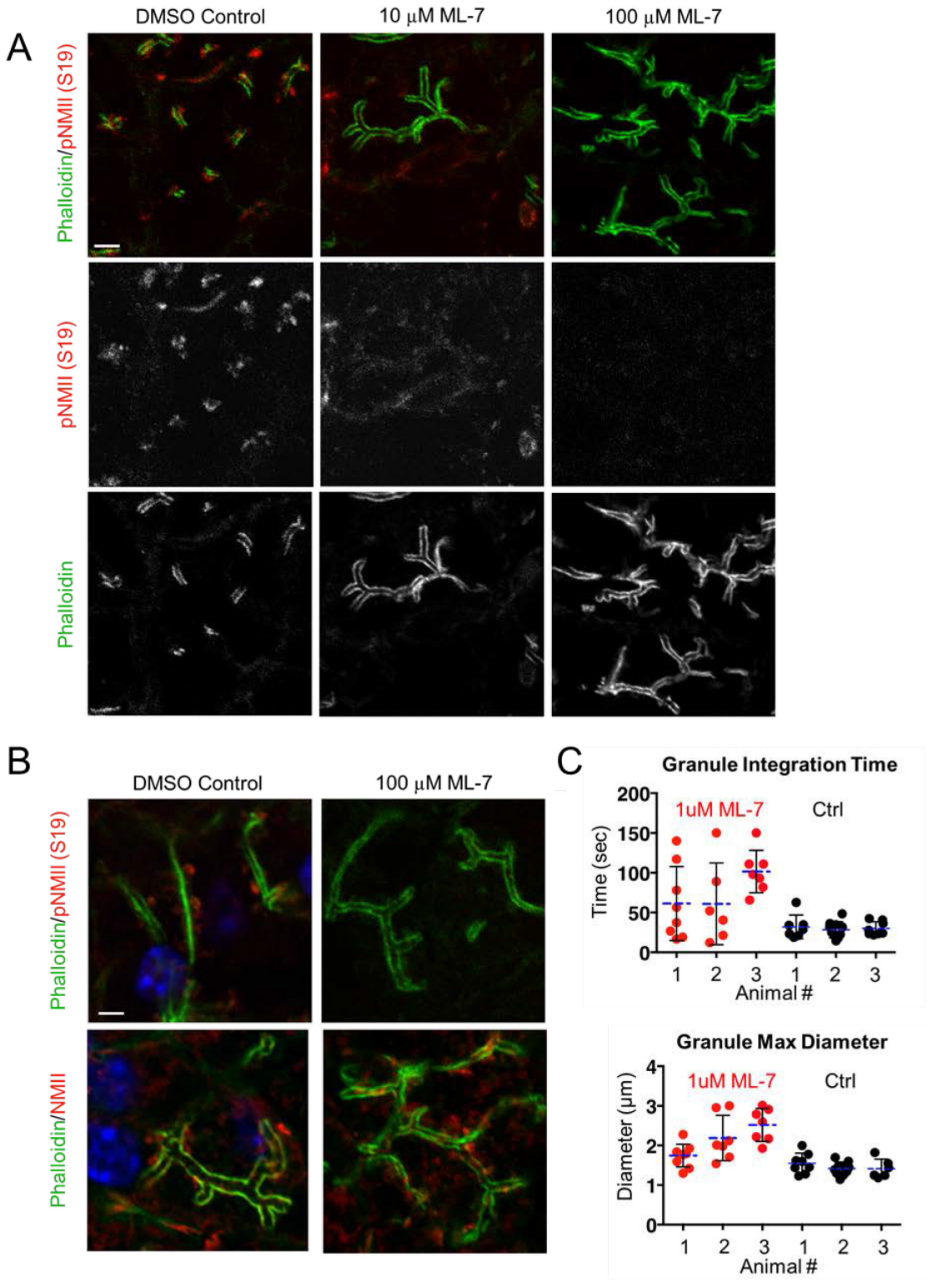

Figure 56. ML-7 inhibition of MLCK activity affects NMII RLC phosphorylation on the granules and at the APM. A) Dose-dependent inhibition of MLCK activity with

increasing ML-7 concentration. SSGs of C57BL/6J mice were bathed with either 10 μM (center panels) or 100 μM (right panels) of ML-7 for 30 minutes and stimulated with ISOP for 10-15 minutes. Cryosections of the SSGs were stained with an antibody against pNMII (S19) (Red), and Phalloidin 488 (green). 0.5% DMSO was used as control (left panels). Scale bar, 5μm. **B)** Mice were treated as described in A) with either 100 μM ML-7 (right panels) or DMSO (left panels), and the SSGs were stained for either pNMII (S19) (upper panels) or NMIIA (lower panels). Scale bars, 5μm. **C)** m-Tomato mice were cannulated with either DMSO or 1μM ML-7, injected with ISOP, and imaged by IVM. The kinetics of membrane integration were determined as described before, and the integration time (upper panel) and the maximum diameters (lower panel) of the granules were reported for each animal (N=23 granules in three ML-7 treated mice; N=32 granules in three DMSO treated mice). All values were plotted to a maximum time of 150 seconds.

Although this result is consistent with the known interactions between F-actin and MLCK [201], based on other data in the literature I wondered whether other molecules could be implicated in linking F-actin to the machinery regulating NMII phosphorylation [203, 204]. In addition, one possible model of NMII recruitment, may be that NMII is recruited to a particular protein, or a set of proteins that are normally present on the granule membranes, and which get distributed to specific sites on the F-actin scaffold as it forms. Therefore, with F-actin formation, NMII may be recruited to these proteins as they are directly on the scaffold as it forms, or on the granule membranes, if it doesn't. Furthermore, I envisioned that these proteins may have a role in not only recruiting NMII, but also activating it. As stated earlier, I specifically explored one specific set of proteins, namely

the septin GTPases, which have NMII, F-actin and membrane binding sites [176], and which during cytokinesis are master regulators of the actomyosin contractile ring.

5.4. Septin GTPases are recruited in an F-actin dependent manner to activate the NMII isoforms through the recruitment of MLCK

Previous work has shown that Septin 2 is responsible for maintaining or recruiting NMII onto F-actin stress fibers in cell culture, and it has also been implicated in promoting actomyosin activity during cytokinesis, possibly through the recruitment of NMII RLC phosphorylating kinases [163]. One of the main findings of this work was that Septin 2 directly binds a portion of the C-terminal tail of NMII in order to promote its activation. Further work from Mavrakis et al. in Drosophila showed that Septins 2, 6 and 7 bind to F-actin and generate curved and tightly packed F-actin networks [141]. They further reported defects in F-actin ring formation, when septins were genetically disrupted in the fly. Together these studies supported the idea that septin filaments may be responsible for forming curved actin filament networks around the secretory granules, and for recruiting and activating NMII onto the granular membranes. Lastly, it should be noted that Ptdns(4, 5)P_2 is a di-phosphorylated phosphoinositide (Ptdns) that is present at the APMs and is continuously produced on the granule membranes in high amounts during regulated exocytosis [8]. Septins, including Septin 2, have been shown to interact with these lipids in other processes in order to regulate their activities [205]. Thus, it is possible that septin filaments may play similar roles during regulated exocytosis in the SSGs.

First, I checked whether Septin 2 and its associated septins were expressed and localized onto the fused secretory granules. Under resting conditions, Septins 2, 6, and 7 were localized to the apical and basolateral PM, but not on the cytoplasmic granules (Fig. 57). Upon stimulation, Septins 2, 6 and 7 were recruited onto the fused secretory granules (Fig. 58). Moreover, all the three septins were also found in a series of cytoplasmic puncta, whose nature has not been established, yet. Interestingly, Septin 9, which is known to play a role in cancer cell migration and has been associated with Septin 2 [206, 207], was also found to be recruited to the secretory granules post-fusion (Fig. 57 and 58). On the other hand, Septin 5 appeared on the basolateral PM, but was not localized on the APM and the secretory granules before or after β-adrenergic stimulation (Fig. 59); thus, showing that other septin GTPases, may regulate activities in the acinar cells other than secretory granules exocytosis.

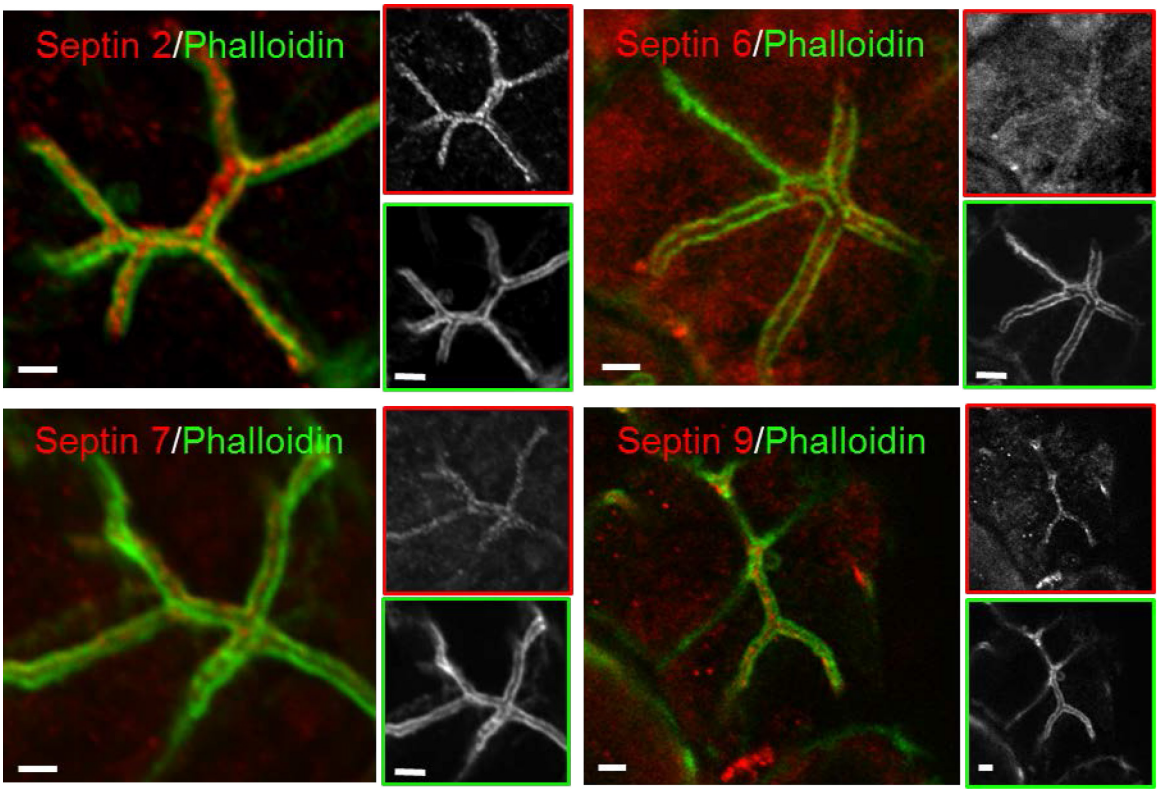

Figure 57. Septins 2, 6, 7 and 9 are localized to the APM along with F-actin under resting conditions. C57BL/6J were fixed by cardiac fixation and sectioned on a vibratome. Staining for Septins 2, 6, 7 and 9 (red) are seen in the images above co-labeled with Phalloidin (green) for F-actin, which is outlining the canaliculi. Thus, all four septins are colocalized with F-actin at the APMs in the respective acini and are largely excluded from the cytoplasmic granules that haven't fused with the APM. Scale bars, 5 µm.

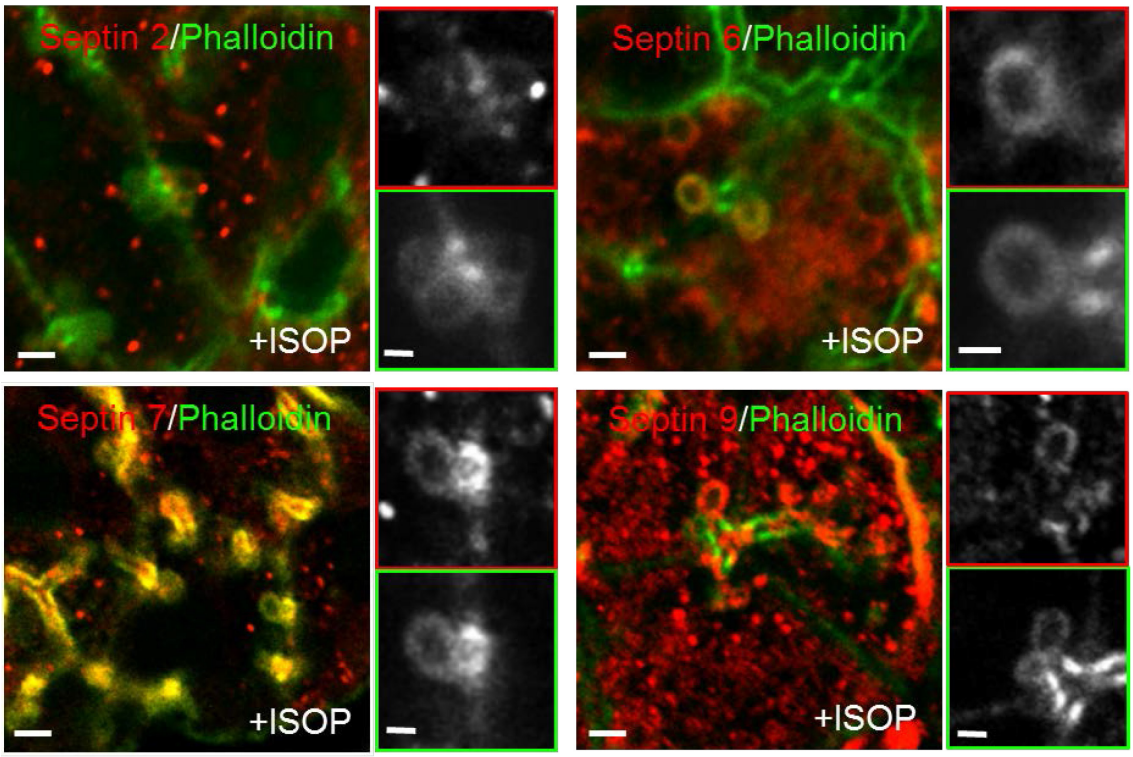

Figure 58. Septins 2, 6, 7 and 9 are recruited to fused secretory granules coated by F-actin following stimulation of regulated exocytosis by ISOP. C57BL/6J mice were stimulated with ISOP for 10-15 minutes and fixed by cardiac perfusion. The SSGs were excised, sectioned on a vibratome and stained for the respective septins (red) and for Phalloidin (green). All four septins were found to colocalize with F-actin around the fused secretory granules at the APMs. Scale bars, 5 µm.

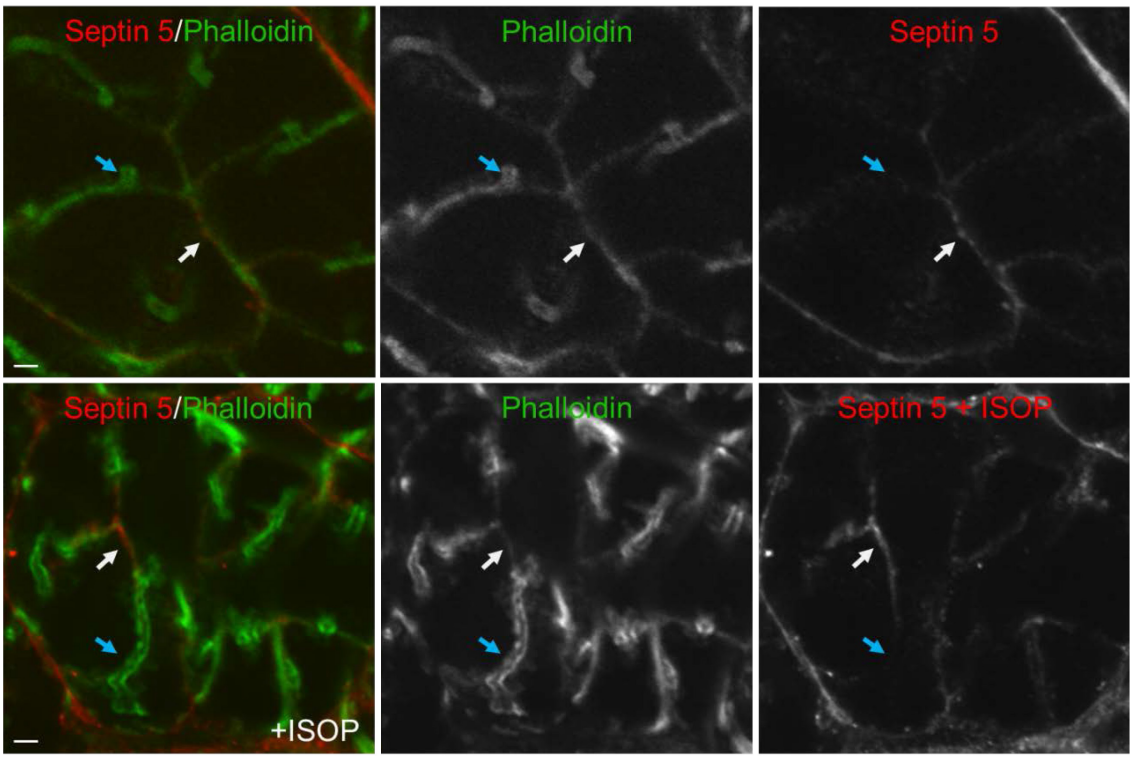

Figure 59. Septin5 is localized to the basolateral PM before and after stimulation of regulated exocytosis, but is excluded from the APMs, or the secretory granules. SSGs of C57BL/6J mice were treated were either fixed directly by cardiac perfusion (under resting conditions; top panel), or following the stimulation of regulated exocytosis for 10-15 minutes by a subcutaneous injection of ISOP (bottom panel). The glands were subsequently sectioned on a vibratome and stained for Septin 5 (red) and Phalloidin (green). Septin 5 is localized to the basolateral PM under resting conditions and after stimulation of regulated exocytosis (white arrows). Septin 5 is largely excluded from the APMs before and after stimulation of regulated exocytosis (blue arrows). Scale bar, 3µm.

In addition, in order to look at the dynamics of recruitment of the septins with respect to F-actin assembly, I co-transfected Sprague-Dawley rats with RFP-LifeAct and GFP-Septin 2 plasmids. Interestingly, time-lapse imaging showed that Septin 2 was recruited to the secretory granules after the recruitment of F-actin (Fig. 60 and Movie 9). Since it has only been found that septins function as heterofilaments upon binding GTP, I assumed that all four septins found on the secretory granules were recruited to, or at least began to function at the same time they were recruited to the F- actin scaffold. However, this aspect has to be experimentally confirmed.

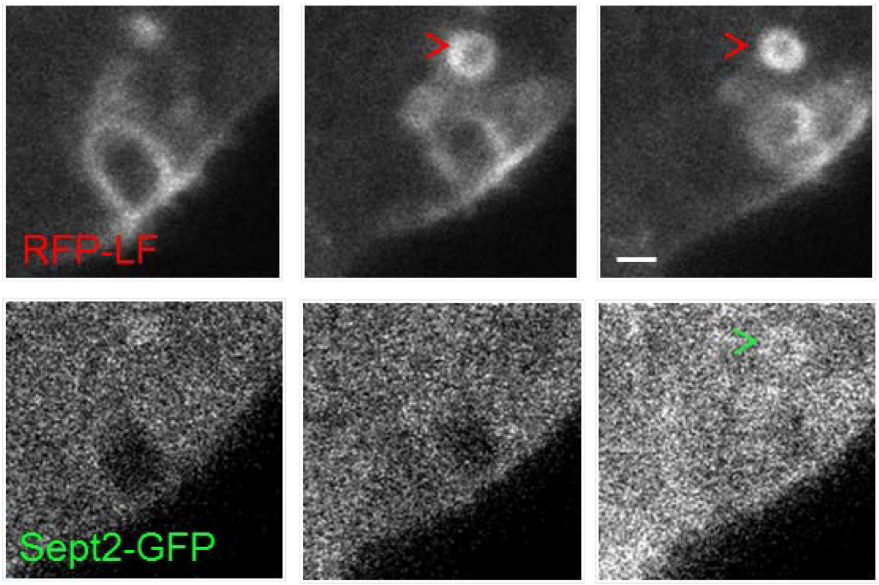

Figure 60. Septin 2 is recruited to the secretory granules at the APM following the recruitment of F-actin. RFP-LifeAct (RFP-LF) and Septin 2-GFP (Sept2-GFP) were transfected in rats, as described in the methods, and imaged 48 hours later by IVM. After stimulation with ISOP, RFP-LF (red arrowhead) was found to be recruited to fused secretory granules at the APM, and followed after some delay by the recruitment of Sept2-GFP (green arrowhead). Scale bar, 1µm.

The role of the septins in regulating the activity of the actomyosin complex was tested by administering Forchlorfenuron (FCF), which is a synthetic plant cytokinin that has been shown to be a specific functional inhibitor of septin filament activity [208-210]. FCF was delivered to the acinar cells in the SSGs of m-Tomato mice by either cannulation or bathing, and exocytosis was stimulated. Immunofluorescence staining showed that F-actin and NMII were still recruited onto the secretory granules. However phosphorylation, of NMII RLCs was inhibited in a dose dependent manner (Fig. 61A).

Furthermore, inhibition of septin activity by administration of 25 μM FCF by cannulation to partially inhibit NMII phosphorylation during exocytosis during live imaging produced a heterogeneous response, with results comparable to those of ML-7 administration. The results showed that granule integration was delayed to around 96 +/- 32 seconds (21 granules in three mice) compared to the controls (0.5% DMSO), where granule integration occurred in about 33 +/- 8 seconds (32 granules in three mice); which was about a 190% +/- 98% increase over the controls (*P-value* = 7.5E-11 << 0.05, one-way ANOVA). In addition, the granules during integration reached a maximum average diameter of about 2.41 +/- 0.50 μm, which was about a 53% +/- 31% increase compared to the control granules that had a maximum average diameter of 1.58 +/- 0.19 μm (*P-value* = 4.7E-11 << 0.05; one-way ANOVA), and this is consistent with the results obtained from the impairment in the function of both NMII isoforms (Fig. 61B and Movie 10).

Furthermore, staining for MLCK and Phalloidin in C57BL/6J mice following 800 μM FCF administration (the maximum effective dose that was determined) showed that MLCK recruitment to F-actin coated granules was significantly reduced (Fig. 62A). Quantification of the percentage of actin-coated profile that also had MLCK on the

granules in the control SSGs was 62.3 +/- 5.1% (N=600 granules in three mice) and in the FCF treated SSGs it was 3.1 +/- 0.4% (N=1073 granules in three mice) (Fig. 62B). Interestingly, in m-Tomato mice that were treated with 10 μM Cytochalasin D through cannulation, Septin 2 was not localized on the expanded granules lacking F-actin, whereas it was recruited to the F-actin coated ones (Fig. 62C); and the same was observed with the other septins (not shown). Thus, similar to MLCK, septins are recruited in an F-actin dependent manner in order to promote the activation of NMII through the phosphorylation of their RLCs. In conclusion, septins are recruited in an F-actin dependent manner and possibly act as a docking site to bring MLCK and NMII together in order to promote NMII phosphorylation and actomyosin contractile activity, which drives secretory granule integration.

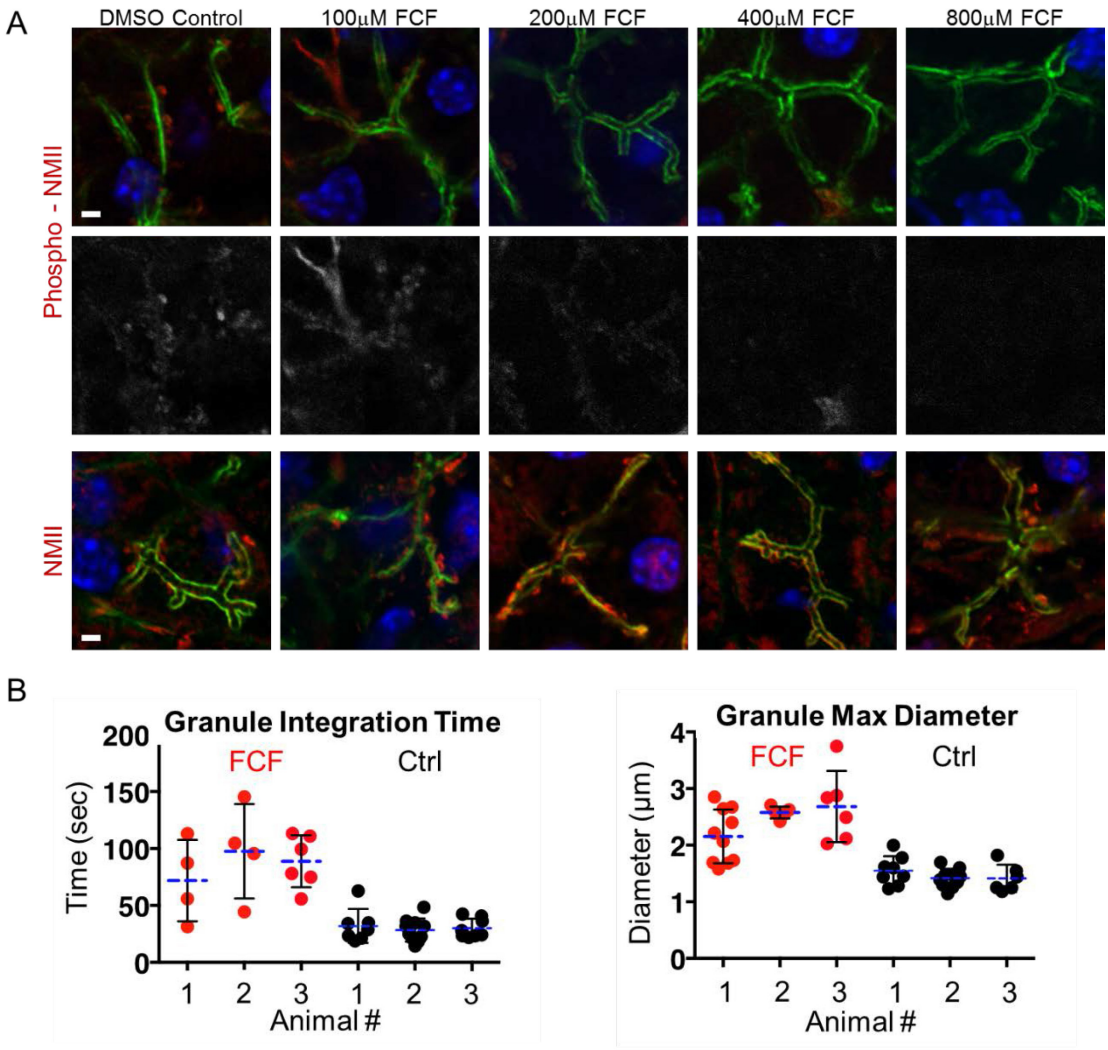

Figure 61. Forchlorfenuron (FCF) specifically inhibits septin functional activity in a dose dependent manner, showing a clear role for septin GTPases in promoting the phosphorylation of NMII RLCs and thus, NMII activity during regulated exocytosis.

A) C57BL/6J mice SSGs were bathed with different concentrations of FCF or 5% DMSO, as control, for 45 minutes, and then stimulated with ISOP for 10-15 minutes. Glands were fixed by cardiac perfusion, sectioned on a vibratome and stained with Phalloidin and either pNMII (S19T18) or NMIIA. It is clearly seen that the level of pNMII on the granules (red, top panel; grey, middle panel) decreases rapidly with increasing FCF concentration, while the NMIIA (red, bottom panel) is still recruited to the granules at all FCF concentrations.

Scale bar, 5 µm. **B)** 25 µM FCF was administered by cannulation to partially inhibit phosphorylation of NMII RLCs, mice were injected with ISOP, and imaged by time-lapse IVM. The integration time (left panel) and the granule maximum diameter (right panel) were determined and reported for each animal (N=21 granules in three mice for the FCF treated glands, and N=32 granules in three mice for the controls). All values were plotted to a maximum time of 150 seconds.

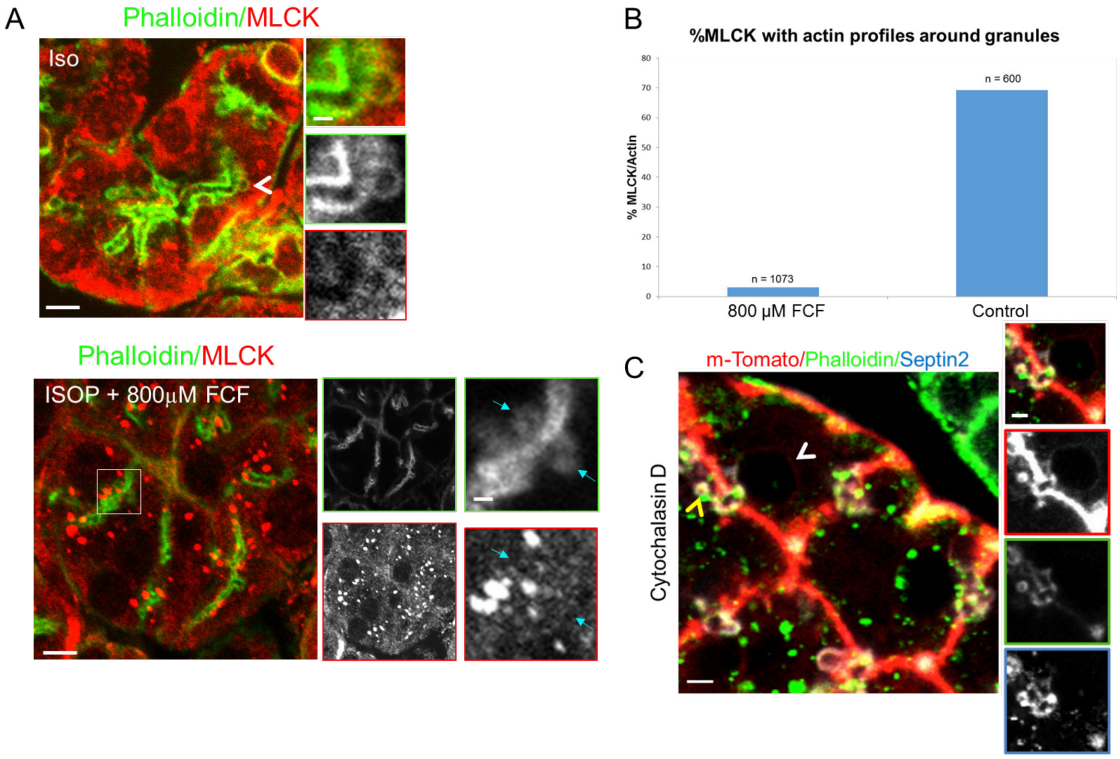

Figure 62. Septins are recruited in an F-actin dependent manner to activate NMII through MLCK recruitment to the F-actin scaffold. A) 800 µM FCF or 5% DMSO were administered by cannulation into the SSGs of C57BL/6J mice, and after 45 minutes stimulated with ISOP for 5-10 minutes. SSGs were then fixed by cardiac perfusion, excised and stained in parallel using the same mixture for MLCK, Phalloidin, and secondary antibodies. Staining revealed that in the FCF treated gland, MLCK appeared mainly as

large bright aggregates and was not colocalized with the APM, and its presence on any fused secretory granules was minimum (white arrowhead, bottom panel). On the other hand, in the DMSO control gland, MLCK staining was found to colocalize with F-actin on the fused granules and at the APM (white arrowhead, top panel). Scale bars, 5 μm. **B)** Quantification of the percentage of actin coated secretory granules that were positive for MLCK. Experiments were carried out with N=1073 granules quantified in three animals treated with FCF, and N=600 granules quantified in the glands that were treated with 5% DMSO for the same amount of time in three animals. All images were taken using the same magnification, so that the entire field of view was occupied with acinar cells. The FCF treated samples had more granules per acini. **C)** 10 μM Cytochalasin D was administered by cannulation in m-Tomato mice. After ISOP stimulation, SSGs were fixed, excised and stained for Septin 2 and Phalloidin. Septin 2 was not recruited to enlarged granules (white arrowhead) that lacked F-actin, but was recruited to normal size granule, which had F-actin coated on them (blue arrowhead). Scale bars, 2 μm and 1 μm inset.

It is important to emphasize that at this point I have not formally proven whether 1) septins form a complex on the secretory granules and 2) if heterofilaments or any of the individual septins interact with the MLCK. However, based on the large body ofliterature on the role of Septin 2 during cytokinesis, I am inclined to support the idea that this septin, while assembled in heterofilaments, may play the main role during exocytosis. Indeed, a Septin 2 binding sites has been found and characterized on the c-terminal domain of NMIIA and a direct interaction between F-actin and Septin 2 has been recently shown [141, 163, 211]. Therefore, Septin 2 is the ideal candidate to re-distribute the membrane bound

NMII to specific sites on the F-actin scaffold and promote their interactions with MLCK. An important issue to be addressed is what the role of the other septins are. Since the two NMII isoforms show different localization it would be important to determine whether the heterofilaments on the secretory granules are heterogeneous in composition and hence may show a different specificity in their interaction with either NMIIA or NMIIB, thus regulating their exact distribution on the secretory granules. Due to the limitations of the pharmacological approach these issues could be sorted out only with the development of selective genetic tools (i.e. septin conditional knock-out mice).

Lastly, as mentioned above, we observed that after stimulation of exocytosis the septins (and the other proteins) are also redistributed from the APM into cytoplasmic puncta (Fig. 63). This structure may represent compensatory vesicles that are used to either retrieve the membranes integrated into the APM, or to partially disassemble the actin cytoskeleton at the APM to favor docking and fusion of the incoming secretory granules. This is an important area of investigation that is beyond the aims of this thesis work but that gives a clear picture of the complexity of this process in vivo.

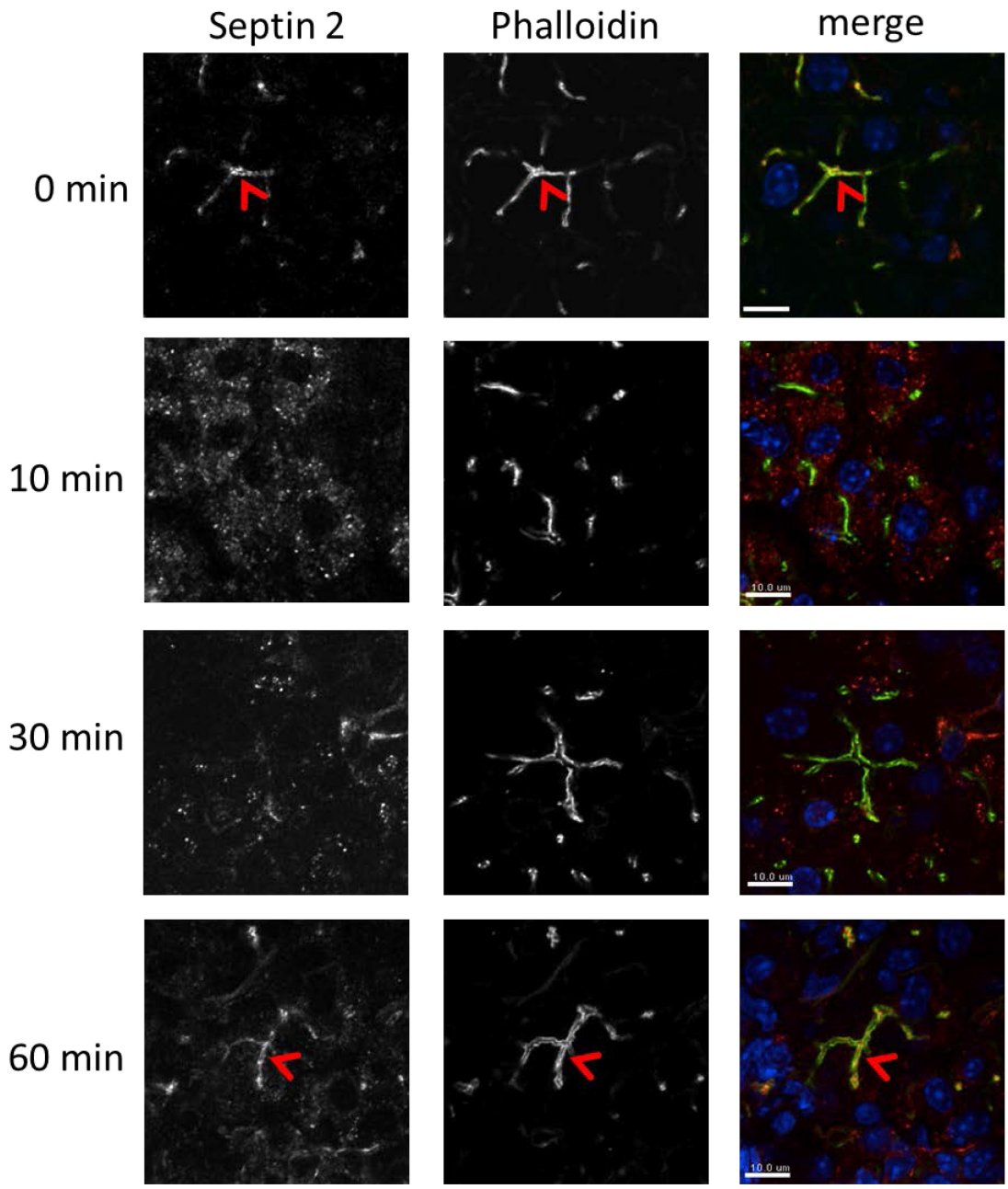

Figure 63. Upon stimulation of regulated exocytosis, Septin 2 is redistributed from the APMs into cytosolic puncta, suggesting its multiple roles within the acinar cells during the exocytic process. Regulated exocytosis was stimulated in four different C57BL/6J mice from 10-60 minutes and each mouse was fixed at a different time point. The SSGs form each mouse were then sectioned and stained for Septin 2 (red), with Phallodin (green)

for F-actin, and HÖESCHT (blue) to label the cell nuclei. It is shown that prior to stimulation Septin 2 in on the APMs with F-actin, stimulation causes it come to the cytoplasm in the form of small puncta. Over the course of 60 minutes, Septin 2 is gradually returned to the APMs (red arrowheads). Scale bars, 10 μm.

6. Conclusions: A working model for the dynamics of the actomyosin contractile complex in driving secretory granule integration

Finally, having discussed the kinetics and the process of actomyosin assembly, as well as its regulation and activity, I would like to speculate about the molecular structure of the actomyosin complex and how it transmits the force needed to drive secretory granule integration. Two interesting aspects that were determined about the process of granule integration are: 1) that the rate of integration, from the beginning to end, occurs at a constant linear rate that is within and around 50 nm/s, which is about the same rate at which NMIIB filaments were found to translocate along F-actin filaments *in vitro* [128], and 2) that the levels of NMIIA and NMIIB recruited onto the granules increase at a constant rate even as granule integration proceeds for some time, and all the other fluorescent probes are decreasing in intensity during that time (i.e. mainly referring to the other actomyosin complex component, F-actin).

The work I presented in this thesis suggests that NMIIB may be responsible for secretory granule integration by stabilizing the granules and pushing them into the APMs, whereas NMIIA may work on regulating the opening of the fusion pore, at the neck of the secretory granules. Both NMIIA and NMIIB cannot directly act on the membranes of the

granules but rather do so through the membrane-associated F-actin scaffold built around them. Therefore, I envision that the structure of the F-actin scaffold is the main determinant of how the force generated by each NMII molecule is transduced to the granular membrane. Since the F-actin scaffold is directly responsible for driving the integration of each granule into the APM, its rate of contraction should ideally be equivalent to the rate of granule integration. The maximum rate at which NMIIB filaments can walk along F-actin was estimated to be 48 +/- 2 nm/s, which should be the maximum rate at which an anchored NMIIB filament can translocate an actin filament. An interesting speculation is that the F-actin scaffold, functionally behaves as an interconnected unit patterned with NMIIB filaments, which transduces to the membrane the force generated by the NMIIB in the direction of the APM.

Moreover, since the average rate of integration matches the average maximal rate of F-actin translocation achievable by NMIIB, it is plausible that the actomyosin filaments are not assembled in a random fashion but rather in a specific pattern that favors the integration. Some support for this comes from a recent paper where the F-actin scaffold during cytokinesis was depicted to have "structural memory" [212]. Moreover, since our data are consistent with NMIIA and NMIIB forming mostly homo-filaments (i.e. not colocalizing on the same F-actin filaments in order to have separate functional roles in the different regions of the granules), it is conceivable that NMIIA is localized on a separate F-actin scaffold that operates at the neck of the vesicles and generates contractions that are in sync with those generated by NMIIB.

On the other hand, it is conceivable that the F-actin scaffold may still be one functionally interconnected unit, even at the fusion pore area, that is designed in a way such that the scaffold is more dynamic at the fusion pore as pulling open of the fusion pore occurs, and less so around the granules where a gradual contraction (or pushing in) would be necessary. In the latter scenario, while both NMII isoforms would be forced to act cooperatively, each would mainly be responsible for its functional region (i.e. granule integration, or fusion pore expansion). Thus, the different regions of the F-actin scaffold would be patterned with the different NMII isoforms. Computational modeling of the structure and dynamics of the F-actin scaffold and NMII interactions during each step of the integration process to find the theoretically most efficient arrangement may help to solve this dilemma, which can be backed up with the latest advances in imaging and cell biology techniques.

In addition, the increase in the NMII levels during the integration could be related to the shrinking of the F-actin scaffold around the secretory granules. Either the same number or a higher number of NMII isoforms may be required to continue providing force on the granules, although packed into a smaller scaffold. It is possible that the F-actin scaffold gets smaller in size until about half-way through integration, at which point it reaches the same size as that on the APM with which it aligns as the granules integrate. Furthermore, during integration, after the NMII isoforms have reached their peak intensities, they dissociate from the granule as the diameter of the granule shrinks. The exact mechanism of this process is interesting and is something to look into in future studies.

The roles and regulation of the main force producing molecules (NMIIA and NMIIB) responsible for actomyosin contraction during regulated exocytosis in the SSGs were studied and identified in this thesis. In addition, based on the results and with support from existing literature, we have generated a model of how the actomyosin complex dynamically acts to drive the integration of the secretory granules into the APMs in the SSGs of live rodents (Fig. 64). As discussed earlier, these finding may be translatable to how regulated exocytosis occurs in other exocrine organs, such as the exocrine pancreas, as well as to other systems where mechanical and signaling activities are intertwined. Thus, this thesis is the first work, to our knowledge, that links membrane remodeling, cytoskeleton function, intracellular signaling and tissue physiology using a live rodent model system, and it provides the groundwork for studying the biophysics and cell biology of regulated exocytosis *in vivo* (in live rodents).

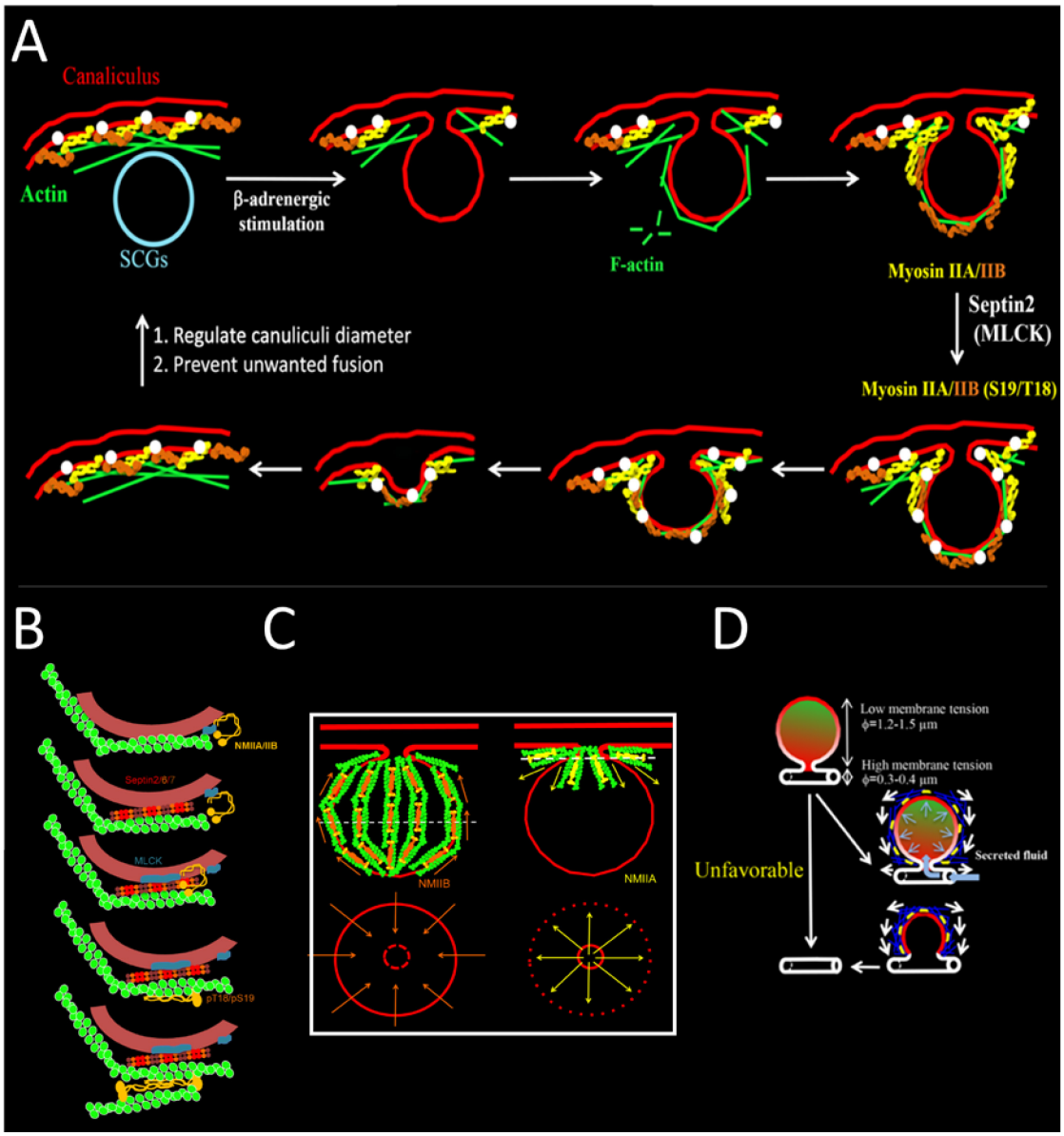

Figure 64. Model of secretory granule exocytosis in the SSGs. A) Secretory granule exocytosis in the SSGs is stimulated through the β-adrenergic receptor by a subcutaneous injection of isoproterenol. F-actin depolymerization at the APM allows for secretory granules to fuse and undergo exocytosis. Upon fusion of the secretory granules with the APM, in order to provide the necessary force for the granules to integrate into APM, an actomyosin complex composed of F-actin and NMIIA and NMIIB are recruited to the secretory granules. An F-actin scaffold is recruited about 2-3 seconds post-fusion followed

by NMIIA and NMIIB 3-6 seconds later, respectively. **B)** The latter are recruited in an F-actin independent manner to the secretory granules in an inactive conformation. In order for contractile activity to begin, septin GTPases, Septin 2 in particular, bring MLCK and NMIIA or NMIIB together to phosphorylate the RLCs of the myosin isoforms, which allows them to form bipolar filaments and interact with the F-actin scaffold. **C)** During contractile activity, NMIIA is localized to the fusion pore region to maintain an open fusion pore, while NMIIB is localized around the granules outside of the fusion pore and acts to stabilize the granules and provide the necessary force to drive the granular membranes into the APMs. **D)** The actomyosin complex is necessary to provide the force to overcome the hydrostatic pressure from the salivary flow, which pushes back on the granules, and also to promote the integration of the granules into a much narrower canaliculi. Following integration, granule integration both Actin and NMII are returned to the APM after some time regulate the architecture of the cells and the canaliculi.

APPENDIX A

Statistical calculations

1. Initial granule size vs. Rate of integration (Pearson correlation), m-Tomato (mT/mGFP mice)

	Total granules	33	33
	Granule #	mT/mGFP (nm/s) - not fitted	mT/mGFP granule sizes (um)
Mouse 1	1	57.2	1.775
	2	62.4	1.521
	3	59.4	1.331
	4	43.9	1.352
	5	37.9	1.66
	6	38.8	1.446
	7	35.1	1.429
	8	53	1.649
	9	46.1	1.355
Mouse 2	10	43.3	1.485
	11	45.9	1.842
	12	45.5	1.714
	13	71.7	1.617
	14	54.5	1.552
	15	32.5	1.303
	16	50.3	1.544
	17	47.1	1.558
	18	48.3	1.423
	19	63.2	1.929
	20	48.6	1.644
	21	48.8	1.561
	22	31.8	1.587
Mouse 3	23	26.5	1.723
	24	89.3	1.961
	25	38.9	1.444
	26	49.3	1.829
	27	55.1	1.988
	28	26.9	1.556
	29	27.5	1.624
	30	34.8	1.213
	31	36	1.695
	32	31	1.477
	33	34.7	1.355

Correlation (Peasrson Correlation Value)		
	mT/mGFP rates (nm/s)	*mT/mGFP granule sizes (um)*
mT/mGFP rates (nm/s) - not fitted	1	
mT/mGFP granule sizes (um)	**0.431426534**	1

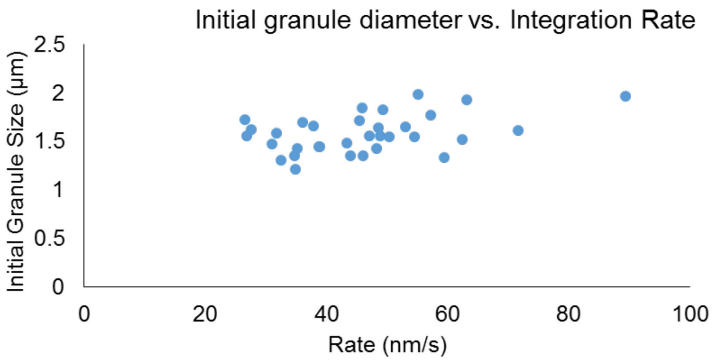

2. mT/mGFP vs. mT/mGFP^{+Cre} initial granule sizes and rates of integration comparison (two-way ANOVA)

Unfitted linear integration rates of individual granules			Starting diameters of individual granules	
Total granules	33	24	33	24
Granule #	mT/mGFP rates (nm/s)	mT/mGFP+Cre rates (nm/s)	mT/mGFP granule sizes (um)	mT/mGFP+Cre granule sizes (um)
1	57.2	44.2	1.775	1.283
2	62.4	52.9	1.521	1.442
3	59.4	41.5	1.331	1.598
4	43.9	86.7	1.352	1.999
5	37.9	40.7	1.66	1.617
6	38.8	49.1	1.446	1.231
7	35.1	39.1	1.429	1.777
8	53	42.4	1.649	1.456
9	46.1	53.4	1.355	1.698
10	43.3	50.2	1.485	1.5
11	45.9	42.9	1.842	1.602
12	45.5	50.1	1.714	1.387
13	71.7	44.1	1.617	1.256
14	54.5	34.8	1.552	1.353
15	32.5	21.7	1.303	1.448
16	50.3	61.8	1.544	1.479
17	47.1	58.9	1.558	1.299
18	48.3	50	1.423	1.145
19	63.2	31.6	1.929	1.441
20	48.6	50.6	1.644	1.25
21	48.8	35.7	1.561	1.185
22	31.8	29.8	1.587	1.82
23	26.5	48.9	1.723	1.247
24	89.3	64.9	1.961	1.548
25	38.9		1.444	
26	49.3		1.829	
27	55.1		1.988	
28	26.9		1.556	
29	27.5		1.624	
30	34.8		1.213	
31	36		1.695	
32	31		1.477	
33	34.7		1.355	

Calculations		
	Rates (nm/s)	Granule size (µm)
mT/mGFP	57.2	1.775
2	62.4	1.521
3	59.4	1.331
4	43.9	1.352
5	37.9	1.66
6	38.8	1.446
7	35.1	1.429
8	53	1.649
9	46.1	1.355
10	43.3	1.485
11	45.9	1.842
12	45.5	1.714
13	71.7	1.617
14	54.5	1.552
15	32.5	1.303
16	50.3	1.544
17	47.1	1.558
18	48.3	1.423
19	63.2	1.929
20	48.6	1.644
21	48.8	1.561
22	31.8	1.587
23	26.5	1.723
24	89.3	1.961
mT/mGFP+Cre	44.2	1.283
2	52.9	1.442
3	41.5	1.598
4	86.7	1.999
5	40.7	1.617
6	49.1	1.231
7	39.1	1.777
8	42.4	1.456
9	53.4	1.698
10	50.2	1.5
11	42.9	1.602
12	50.1	1.387
13	44.1	1.256
14	34.8	1.353
15	21.7	1.448
16	61.8	1.479
17	58.9	1.299
18	50	1.145
19	31.6	1.441
20	50.6	1.25
21	35.7	1.185
22	29.8	1.82
23	48.9	1.247
24	64.9	1.548

Anova: Two-Factor With Replication for integration rates and granule diameters

SUMMARY	Rates (nm/s)	Granule size (µm)	Total
mT			
Count	24	24	48
Sum	1181.1	37.961	1219.061
Average	49.2125	1.581708333	25.39710417
Variance	188.2915761	0.032644216	671.399252
mT+Cre			
Count	24	24	48
Sum	1126	35.061	1161.061
Average	46.91666667	1.460875	24.18877083
Variance	174.7292754	0.047132462	613.0767092
Total			
Count	48	48	
Sum	2307.1	73.022	
Average	48.06458333	1.521291667	
Variance	178.9942509	0.042767488	

ANOVA

Source of Variation	*SS*	*df*	*MS*	*F*	***P-value***	*F crit*
Sample	35.04166667	1	35.04166667	0.386027056	0.535931628	4.858802869
Columns	51990.67198	1	51990.67198	572.7411957	2.77137E-41	4.858802869
Interaction	28.38375	1	28.38375	0.312681916	**0.312681916**	4.858802869
Within	8351.314447	92	90.77515703			
Total	60405.41184	95				

3. mT/mGFP vs. mT/mGFP^{+Cre} initial granule sizes and rates of integration comparison (one-way ANOVA)

Unfitted linear integration rates of individual granules			Starting (and maximum) diameters of individual granules	
Total granules	33	24	33	24
Granule #	mT/mGFP rates (nm/s)	mT/mGFP+Cre granule sizes (nm/s)	mT/mGFP granule sizes (um)	mT/mGFP+Cre granule sizes (um)
1	57.2	44.2	1.775	1.283
2	62.4	52.9	1.521	1.442
3	59.4	41.5	1.331	1.598
4	43.9	86.7	1.352	1.999
5	37.9	40.7	1.66	1.617
6	38.8	49.1	1.446	1.231
7	35.1	39.1	1.429	1.777
8	53	42.4	1.649	1.456
9	46.1	53.4	1.355	1.698
10	43.3	50.2	1.485	1.5
11	45.9	42.9	1.842	1.602
12	45.5	50.1	1.714	1.387
13	71.7	44.1	1.617	1.256
14	54.5	34.8	1.552	1.353
15	32.5	21.7	1.303	1.448
16	50.3	61.8	1.544	1.479
17	47.1	58.9	1.558	1.299
18	48.3	50	1.423	1.145
19	63.2	31.6	1.929	1.441
20	48.6	50.6	1.644	1.25
21	48.8	35.7	1.561	1.185
22	31.8	29.8	1.587	1.82
23	26.5	48.9	1.723	1.247
24	89.3	64.9	1.961	1.548
25	38.9		1.444	
26	49.3		1.829	
27	55.1		1.988	
28	26.9		1.556	
29	27.5		1.624	
30	34.8		1.213	
31	36		1.695	
32	31		1.477	
33	34.7		1.355	

Anova: Single Factor for integration rates

SUMMARY

Groups	*Count*	*Sum*	*Average*	*Variance*
mT/mGFP rates (nm/s)	33	1515.3	45.91818182	187.7334091
mT/mGFP+Cre rates (nm/s)	24	1126	46.91666667	174.7292754

ANOVA

Source of Variation	*SS*	*df*	*MS*	*F*	***P-value***	*F crit*
Between Groups	13.85266348	1	13.85266348	0.075990232	**0.783839802**	4.016195493
Within Groups	10026.24242	55	182.2953168			
Total	10040.09509	56				

Anova: Single Factor for initial (maximum) granule diameters

SUMMARY

Groups	*Count*	*Sum*	*Average*	*Variance*
mT/mGFP granule sizes (um)	33	52.142	1.580060606	0.037797121
mT/mGFP+Cre granule sizes (um)	24	35.061	1.460875	0.047132462

ANOVA

Source of Variation	*SS*	*df*	*MS*	*F*	***P-value***	*F crit*
Between Groups	0.197377637	1	0.197377637	4.733164175	**0.03390126**	4.016195493
Within Groups	2.293554504	55	0.041700991			
Total	2.49093214	56				

4. IIA/IIB$^{mT/mGFP/fl/fl+Cre}$ vs. mT/mGFP^{+Cre} and mT/mGFP maximum granule sizes (one-way ANOVA)

Maximum diameters of individual granules	
19	24
IIA/IIB-mT/mGFPfl/fl+Cre granule sizes (um)	mT/mGFP+Cre granule sizes (um)
2.148	1.283
2.041	1.442
1.756	1.598
2.043	1.999
2.005	1.617
2.373	1.231
2.233	1.777
1.985	1.456
2.474	1.698
2.467	1.5
2.378	1.602
1.911	1.387
1.774	1.256
1.483	1.353
1.647	1.448
1.966	1.479
2.603	1.299
2.077	1.145
1.767	1.441
	1.25
	1.185
	1.82
	1.247
	1.548

Maximum diameters of individual granules	
19	33
IIA/IIB-mT/mGFPfl/fl+Cre granule sizes (um)	mT/mGFP granule sizes (um)
2.148	1.775
2.041	1.521
1.756	1.331
2.043	1.352
2.005	1.66
2.373	1.446
2.233	1.429
1.985	1.649
2.474	1.355
2.467	1.485
2.378	1.842
1.911	1.714
1.774	1.617
1.483	1.552
1.647	1.303
1.966	1.544
2.603	1.558
2.077	1.423
1.767	1.929
	1.644
	1.561
	1.587
	1.723
	1.961
	1.444
	1.829
	1.988
	1.556
	1.624
	1.213
	1.695
	1.477
	1.355

Anova: Single Factor

SUMMARY

Groups	*Count*	*Sum*	*Average*	*Variance*
IIA/IIB-mT/mGFPfl/fl+Cre granule sizes (um)	19	39.131	2.059526316	0.092935596
mT/mGFP+Cre granule sizes (um)	24	35.061	1.460875	0.047132462

ANOVA

Source of Variation	*SS*	*df*	*MS*	***F***	***P-value***	***F crit***
Between Groups	3.800530917	1	3.800530917	56.52090461	**3.08927E-09**	5.054622321
Within Groups	2.756887362	41	0.067241155			
Total	6.557418279	42				

Anova: Single Factor

SUMMARY

Groups	*Count*	*Sum*	*Average*	*Variance*
IIA/IIB-mT/mGFPfl/fl+Cre granule sizes (um)	19	39.131	2.059526316	0.092935596
mT/mGFP granule sizes (um)	33	52.142	1.580060606	0.037797121

ANOVA

Source of Variation	*SS*	*df*	*MS*	***F***	***P-value***	***F crit***
Between Groups	2.771911134	1	2.771911134	48.0842449	**7.60409E-09**	4.989802385
Within Groups	2.882348616	50	0.057646972			
Total	5.65425975	51				

5. IIA$^{mT/mGFP/fl/fl+Cre}$ vs. mT/mGFP^{+Cre} and mT/mGFP maximum granule sizes (one-way ANOVA)

Maximum diameters of individual granules	
23	24
IIA-mT/mGFPfl/fl+Cre granule sizes (um)	mT/mGFP+Cre granule sizes (um)
1.439	1.283
1.081	1.442
1.571	1.598
1.398	1.999
1.07	1.617
1.209	1.231
1.719	1.777
1.715	1.456
2.04	1.698
1.707	1.5
2.09	1.602
1.677	1.387
1.917	1.256
1.339	1.353
1.987	1.448
1.535	1.479
1.788	1.299
1.966	1.145
1.732	1.441
1.834	1.25
1.358	1.185
1.577	1.82
1.617	1.247
	1.548

Maximum diameters of individual granules	
23	33
IIA-mT/mGFPfl/fl+Cre granule sizes (um)	mT/mGFP granule sizes (um)
1.439	1.775
1.081	1.521
1.571	1.331
1.398	1.352
1.07	1.66
1.209	1.446
1.719	1.429
1.715	1.649
2.04	1.355
1.707	1.485
2.09	1.842
1.677	1.714
1.917	1.617
1.339	1.552
1.987	1.303
1.535	1.544
1.788	1.558
1.966	1.423
1.732	1.929
1.834	1.644
1.358	1.561
1.577	1.587
1.617	1.723
	1.961
	1.444
	1.829
	1.988
	1.556
	1.624
	1.213
	1.695
	1.477
	1.355

Anova: Single Factor

SUMMARY

Groups	*Count*	*Sum*	*Average*	*Variance*
IIA-mT/mGFPfl/fl+Cre granule sizes (um)	23	37.366	1.624608696	0.084486794
mT/mGFP+Cre granule sizes (um)	24	35.061	1.460875	0.047132462

ANOVA

Source of Variation	*SS*	*df*	*MS*	*F*	*P-value*	*F crit*
Between Groups	0.314859897	1	0.314859897	4.814770527	**0.033420681**	5.0224611
Within Groups	2.942756103	45	0.06539458			
Total	3.257616	46				

Anova: Single Factor

SUMMARY

Groups	*Count*	*Sum*	*Average*	*Variance*
IIA-mT/mGFPfl/fl+Cre granule sizes (um)	23	37.366	1.624608696	0.084486794
mT/mGFP granule sizes (um)	33	52.142	1.580060606	0.037797121

ANOVA

Source of Variation	*SS*	*df*	*MS*	*F*	*P-value*	*F crit*
Between Groups	0.0268975	1	0.0268975	0.473390518	**0.494376566**	4.968200645
Within Groups	3.068217357	54	0.05681884			
Total	3.095114857	55				

6. IIB$^{mT/mGFP/fl/fl+Cre}$ vs. mT/mGFP^{+Cre} and mT/mGFP maximum granule sizes (one-way ANOVA)

Maximum diameters of individual granules	
18	24
IIB-mT/mGFPfl/fl+Cre granule sizes (um)	mT/mGFP+Cre granule sizes (um)
1.975	1.283
2.137	1.442
2.301	1.598
2.106	1.999
3.417	1.617
2.915	1.231
2.567	1.777
2.496	1.456
2.205	1.698
1.523	1.5
2.166	1.602
1.851	1.387
2.01	1.256
2.236	1.353
2.449	1.448
1.852	1.479
1.515	1.299
1.699	1.145
	1.441
	1.25
	1.185
	1.82
	1.247
	1.548

Maximum diameters of individual granules	
18	33
IIB-mT/mGFPfl/fl+Cre granule sizes (um)	mT/mGFP granule sizes (um)
1.975	1.775
2.137	1.521
2.301	1.331
2.106	1.352
3.417	1.66
2.915	1.446
2.567	1.429
2.496	1.649
2.205	1.355
1.523	1.485
2.166	1.842
1.851	1.714
2.01	1.617
2.236	1.552
2.449	1.303
1.852	1.544
1.515	1.558
1.699	1.423
	1.929
	1.644
	1.561
	1.587
	1.723
	1.961
	1.444
	1.829
	1.988
	1.556
	1.624
	1.213
	1.695
	1.477
	1.355

Anova: Single Factor

SUMMARY

Groups	*Count*	*Sum*	*Average*	*Variance*
IIB-mT/mGFPfl/fl+Cre granule sizes (um)	18	39.42	2.19	0.224028706
mT/mGFP+Cre granule sizes (um)	24	35.061	1.460875	0.047132462

ANOVA

Source of Variation	*SS*	*df*	*MS*	***F***	***P-value***	***F crit***
Between Groups	5.468125018	1	5.468125018	44.70586669	**5.14133E-08**	5.063721323
Within Groups	4.892534625	40	0.122313366			
Total	10.36065964	41				

Anova: Single Factor

SUMMARY

Groups	*Count*	*Sum*	*Average*	*Variance*
IIB-mT/mGFPfl/fl+Cre granule sizes (um)	18	39.42	2.19	0.224028706
mT/mGFP granule sizes (um)	33	52.142	1.580060606	0.037797121

ANOVA

Source of Variation	*SS*	*df*	*MS*	*F*	***P-value***	*F crit*
Between Groups	4.333009455	1	4.333009455	42.31120718	**3.88373E-08**	4.995777813
Within Groups	5.017995879	49	0.102408079			
Total	9.351005333	50				

7. IIA/IIB$^{mT/mGFP/fl/fl+Cre}$ vs. IIB$^{mT/mGFP/fl/fl+Cre}$ maximum granule sizes (one-way ANOVA)

Maximum diameters of individual granules	
19	**18**
IIA/IIB-mT/mGFPfl/fl+Cre granule sizes (um)	**IIB-mT/mGFPfl/fl+Cre granule sizes (um)**
2.148	1.975
2.041	2.137
1.756	2.301
2.043	2.106
2.005	3.417
2.373	2.915
2.233	2.567
1.985	2.496
2.474	2.205
2.467	1.523
2.378	2.166
1.911	1.851
1.774	2.01
1.483	2.236
1.647	2.449
1.966	1.852
2.603	1.515
2.077	1.699
1.767	

Anova: Single Factor

SUMMARY

Groups	*Count*	*Sum*	*Average*	*Variance*
IIA/IIB-mT/mGFPfl/fl+Cre granule sizes (um)	19	39.131	2.059526	0.092936
IIB-mT/mGFPfl/fl+Cre granule sizes (um)	18	39.42	2.19	0.224029

ANOVA

Source of Variation	*SS*	*df*	*MS*	***F***	***P-value***	***F crit***
Between Groups	0.157351263	1	0.157351	1.004737	**0.32305**	5.117494
Within Groups	5.481328737	35	0.156609			
Total	5.63868	36				

8. Recruitment and dissociation half-time comparison between RFP- and GFP- LifeAct (one-way ANOVA). Three mice, entire data set

Recruitment and dissociation half-times comparison between RFP- and GFP- LifeAct								
	Recruitment			Dissociation				
	t1/2	t1/2		t1/2	t1/2			
	RFP-LF	GFP-LF		RFP-LF	GFP-LF			
1	9.363528257	10.90787535		11.1589782	16.143684			
2	8.364650458	5.329115173		15.20321166	16.53683849			
3	6.853855786	4.921412692		12.51896305	14.59703099			
4	7.913214591	13.6961393		7.64778013	15.41852933			
5	9.068918823	5.582827274		9.435071468	19.25672127			
6	6.80547029	3.039032415		12.70809831	8.446266932			
7	5.999453427	4.300785047		9.188675931	9.510035761			
8	7.232778305	4.726905757		8.308413711	12.76635205			
9	8.787134734	3.153425728		9.3931584	7.619296316			
10	9.987455093	5.743877579		9.860263292	14.48102687			
11	6.453597438	19.78759796		16.77418341	10.68204531			
12	6.340614702	5.528833925		12.95700475	19.71553104			
13	12.42482481	4.948027047		11.74808674	12.79101605			
14	9.587163525	4.472993894		12.87037104	13.09310522			
15	5.866265012	8.124687765		7.413512522	12.97489992			
16	6.121069829	10.13765604		8.070550614	13.77882074			
17	10.59270036	4.539036865		7.531160614	18.46004654			
18	7.752986611	11.41455009		7.187586639	15.38402874			
19	8.845216598	13.17349205		12.02224809	11.59361191			
20	4.746678997	6.809497773		9.189388586	10.2343404			
21	5.952840582	8.782759766		9.584983039	12.18288055			
22	6.496945417	8.853818566		11.2030254	13.82760652			
23	5.382746222	6.484876279		13.48936319	7.363341057			
24	6.782828317	8.490196078		11.53146482	15.74937611			
25	11.63142345	9.716195644		4.051490663	11.09730853			
26	8.111065855	2.711084838		11.22275178	9.133696568			
27	5.007329525	5.951023022		6.922842234	5.489678195			
28	6.818444709	7.113838124		7.203046169	11.06794477			
29	4.952814098	7.544861149		6.280431347	5.132426769			
30	7.284122338	5.967444223		6.155346512	9.54598342			
31	9.149818095	7.15503655		9.253865975	8.977984444			
32	7.844960357	11.85604933		9.928499553	13.5265316			
33	6.38114574	7.474880873		9.702814921	6.957491947			
34	6.525786111	6.316846221		9.588402785	7.216841075			
35	6.492420214	7.182668961		10.1766254	7.103988324			
36	10.43553642	7.212228192		7.535842255	14.70623451			
37	5.914784615	4.870434835		10.20855573	13.52039375			
38	6.983410976	7.006645941		5.593511919	6.018125349			
39	8.687144709	9.936348584		9.589947161	7.31693276			
40	8.95430892	12.8799728		10.28475598	15.80417899			
41	6.456630425	6.347183046		10.7126914	9.651517615			
42	4.08321533	9.699732498		10.84780063	10.83115536			
43	7.656943032	4.665679956		9.185290165	13.22017207			
44	5.536674911	4.141571767		10.14295957	9.686346826			
45	8.161327513	7.156830816		8.598457994	6.337406972			
46	7.082484305	5.854443325		7.800931884	7.124654295			
47	6.902079621	7.717067028		11.63072142	8.69346561			
48	9.375412688	6.355934651		6.031545904	6.58615962			
49	8.204936531	9.970935271		11.67183282	14.30493764			
50		9.961986814			5.133321664			
51		10.6341703			6.687209393			
52		4.761146914			8.808686422			
53		5.631522497			4.737946739			
54		6.426213851			8.113006622			
Avg	**7.517493034**	**7.466099971**		**9.74115318**	**11.02107704**			
Std	**1.773958295**	**3.115611146**		**2.470809289**	**3.858629033**			

Anova: Single Factor (Recruitment)

SUMMARY

Groups	*Count*	*Sum*	*Average*	*Variance*
RFP-LF	49	368.3571587	7.517493034	3.212489032
GFP-LF	54	403.1693984	7.466099971	9.890184373

ANOVA

Source of Variation	*SS*	*df*	*MS*	*F*	*P-value*	*F crit*
Between Groups	0.067851839	1	0.067851839	0.010102072	0.920139434	3.935188692
Within Groups	678.3792453	101	6.716626191			
Total	678.4470971	102				

Anova: Single Factor (Dissociation)

SUMMARY

Groups	*Count*	*Sum*	*Average*	*Variance*
RFP-LF	49	477.3165058	9.74115318	6.232083931
GFP-LF	54	595.13816	11.02107704	15.16994288

ANOVA

Source of Variation	*SS*	*df*	*MS*	*F*	*P-value*	*F crit*
Between Groups	42.08437512	1	42.08437512	3.853087469	0.052404959	3.935188692
Within Groups	1103.147001	101	10.92224754			
Total	1145.231376	102				

9. Recruitment and dissociation half-time comparison between GFP-NMIIA and GFP-NMIIB (one-way ANOVA). Three mice, entire data set.

Recruitment and dissociation half-times comparison between NMIIA and NMIIB (GFP tagged)

	Recruitment		Dissociation	
	t1/2	t1/2	t1/2	t1/2
	GFP-NMIIA	GFP-NMIIB	GFP-NMIIA	GFP-NMIIB
1	13.99283013	15.04721435	7.789609973	17.27433628
2	23.68733523	12.18155289	11.75301836	14.95582143
3	8.651074238	18.0279047	10.29384501	10.5714782
4	9.495974345	19.36318632	10.68262174	15.96175341
5	15.85124536	16.68035198	9.496167011	10.16149939
6	13.73762452	18.04367701	10.62750044	12.81608267
7	9.815573117	15.89719172	16.74477546	14.09269946
8	21.31600007	12.46102424	13.80804299	21.0751722
9	9.701704368	15.96494655	7.095024737	15.12006403
10	17.36568436	11.9743053	10.9529553	11.60879451
11	17.66621028	15.44139379	9.706265667	14.27825587
12	13.41569651	20.84460621	17.58220964	22.96492756
13	13.4338441	15.45682749	8.090781802	14.44862444
14	12.12467949	17.01722004	6.819463243	9.691864193
15	24.46265469	10.03894933	11.39210509	23.34528625
16	12.56159892	14.46750054	7.062999605	6.883906786
17	15.32046182	10.01062376	11.88032405	7.905447322
18	6.110969539	17.37228758	7.712521458	11.7241338
19	10.29095453	11.85565987	16.40651768	9.319543939
20	10.92646514	13.58010335	20.47778146	5.771687771
21	9.767148954	16.56832221	13.89684035	8.309438177
22	4.720912654	7.269487717	8.112936777	11.63474526
23	10.00208576	13.31508146	13.57472884	7.957006746
24	5.337528337	11.6385095	10.83926852	11.94615138
25	9.669862953	7.899056103	17.92955751	13.52603453
26	8.198330438	18.85999931	7.248675121	15.99542611
27	10.80875364	16.83003124	10.6926264	8.889726367
28	9.239382797	12.23620284	8.129096598	7.70886613
29	9.338674914	12.53580925	9.756569839	13.4778426
30	8.829024567	16.13584119	8.026052079	3.664814229
31	8.647434288	13.85997869	5.085577606	8.462111929
32	3.921179588	8.639433278	8.070732142	10.58304181
33	15.8400907	9.082032525	5.495596314	7.433506559
34	19.84517871	8.945906326	2.364689532	13.17123691
35	23.29075012	12.62515076	8.924145517	9.015330062
36	10.39742383	10.68290399	9.952900935	13.07224326
37	20.7802164	13.08889369	8.99507733	5.867010204
38	19.46151375	10.35191006	10.71147359	12.27088556
39	21.26287182	15.62219782	11.27611642	8.060693543
40	18.61762642	9.680865948	9.380785473	7.072279749
41	11.58707618	10.942164	11.70738979	11.78586397
42		13.46485208		16.13880335
43		10.09960192		8.043828838
Avg	**13.158333**	**13.537227**	**10.403546**	**11.72228527**
Std	**5.3781594**	**3.3202528**	**3.6224089**	**4.343832036**

Anova: Single Factor (Recruitment)

SUMMARY

Groups	*Count*	*Sum*	*Average*	*Variance*
GFP-NMI	41	539.4916476	13.15833	29.64771296
GFP-NMI	43	582.1007589	13.53723	11.28655647

ANOVA

ce of Vari	*SS*	*df*	*MS*	*F*	***P-value***	*F crit*
Between	3.013066216	1	3.013066	0.148843242	**0.700642369**	3.957388
Within Gro	1659.94389	82	20.24322			
Total	1662.956956	83				

Anova: Single Factor (Dissociation)

SUMMARY

Groups	*Count*	*Sum*	*Average*	*Variance*
GFP-NMI	41	426.5453674	10.40355	13.44989243
GFP-NMI	43	504.0582668	11.72229	19.31813573

ANOVA

ce of Vari	*SS*	*df*	*MS*	*F*	*P-value*	*F crit*
Between	36.49986058	1	36.49986	2.21808438	0.140238461	3.957388
Within Gro	1349.357398	82	16.45558			
Total	1385.857258	83				

10. Total integration time and granule diameter comparisons between 1µM ML-7 and m-Tom DMSO control, live imaging (one-way ANOVA)

Total integration times	
23 (2 didn't integrate)	32
ML-7 integration times (s)	**m-Tom DMSO control integration times (s)**
93.33	60.435
110.16	32.13
171.36	35.19
82.62	35.19
97.92	33.66
65.79	33.66
110.925	32.13
89.505	32.895
21.42	30.6
40.545	30.6
52.02	29.835
12.24	45.135
150.705	45.9
253.98	42.84
16.83	22.185
117.045	21.42
117.045	22.185
56.61	26.775
78.03	29.835
19.125	29.07
26.775	29.07
37.485	20.655
76.5	39.78
	28.305
	42.84
	35.955
	42.075
	27.54
	34.425
	26.01
	32.895
	32.895

Anova: Single Factor

SUMMARY

Groups	*Count*	*Sum*	*Average*	*Variance*
ML-7 integration times (s)	23	1897.965	82.52021739	3279.085069
m-Tom DMSO control integration times (s)	32	1064.115	33.25359375	68.75390844

ANOVA

Source of Variation	*SS*	*df*	*MS*	*F*	***P-value***	*F crit*
Between Groups	32480.35183	1	32480.35183	23.1779971	**1.27183E-05**	4.023016998
Within Groups	74271.24269	53	1401.344202			
Total	106751.5945	54				

Granule max diameters	
23 (2 didn't integrate)	32
ML-7 granule sizes (um)	**m-Tom DMSO control granule sizes (um)**
1.837	1.961
1.595	1.444
1.771	1.829
1.3	1.988
2.28	1.556
1.796	1.624
1.422	1.213
1.927	1.695
1.767	1.477
1.708	1.355
1.543	1.775
2.012	1.521
3.002	1.331
1.982	1.352
2.121	1.66
2.955	1.446
1.929	1.429
3.012	1.649
2.171	1.355
2.218	1.485
2.789	1.842
2.911	1.714
2.596	1.617
	1.552
	1.303
	1.544
	1.558
	1.423
	1.929
	1.644
	1.561
	1.587

Anova: Single Factor

SUMMARY

Groups	*Count*	*Sum*	*Average*	*Variance*
ML-7 granule sizes (um)	23	48.644	2.114956522	0.276439407
m-Tom DMSO control granule sizes (um)	32	50.419	1.57559375	0.038336701

ANOVA

Source of Variation	*SS*	*df*	*MS*	*F*	***P-value***	*F crit*
Between Groups	3.892934161	1	3.892934161	28.37999173	**2.07682E-06**	4.023016998
Within Groups	7.270104675	53	0.137171786			
Total	11.16303884	54				

11. Total integration time and granule diameter comparisons between 25µM FCF and m-Tom DMSO control, live imaging (one-way ANOVA)

Total integration times	
21 (6 didn't integrate)	32
FCF integration times (s)	**m-Tom DMSO control integration times (s)**
55.845	60.435
75.735	32.13
99.45	35.19
78.03	35.19
110.925	33.66
113.22	33.66
176.715	32.13
145.35	32.895
44.37	30.6
95.625	30.6
104.805	29.835
32.13	45.135
55.845	45.9
113.22	42.84
87.21	22.185
	21.42
	22.185
	26.775
	29.835
	29.07
	29.07
	20.655
	39.78
	28.305
	42.84
	35.955
	42.075
	27.54
	34.425
	26.01
	32.895
	32.895

Anova: Single Factor

SUMMARY

Groups	*Count*	*Sum*	*Average*	*Variance*
FCF integration times (s)	15	1388.475	92.565	1461.390429
m-Tom DMSO control integration	32	1064.115	33.25359375	68.75390844

ANOVA

Source of Variation	*SS*	*df*	*MS*	*F*	***P-value***	*F crit*
Between Groups	35926.90633	1	35926.90633	71.56489037	**7.45979E-11**	4.056612461
Within Groups	22590.83716	45	502.0186036			
Total	58517.74349	46				

Granule max diameters	
21 (6 didn't integrate)	32
FCF granule sizes (um)	**m-Tom DMSO control granule sizes (um)**
2.851	1.961
2.215	1.444
2.675	1.829
1.695	1.988
1.581	1.556
1.685	1.624
2.4	1.213
2.646	1.695
2.068	1.477
1.733	1.355
2.625	1.775
2.579	1.521
2.422	1.331
2.553	1.352
2.708	1.66
3.748	1.446
2.878	1.429
2.837	1.649
2.119	1.355
2.027	1.485
2.49	1.842
	1.714
	1.617
	1.552
	1.303
	1.544
	1.558
	1.423
	1.929
	1.644
	1.561
	1.587

Anova: Single Factor

SUMMARY

Groups	*Count*	*Sum*	*Average*	*Variance*
FCF granule sizes (um)	21	50.535	2.406428571	0.263559657
m-Tom DMSO control granule siz	32	50.419	1.57559375	0.038336701

ANOVA

Source of Variation	*SS*	*df*	*MS*	*F*	***P-value***	*F crit*
Between Groups	8.752311855	1	8.752311855	69.10114745	**4.72918E-11**	4.030392595
Within Groups	6.459630862	51	0.126659429			
Total	15.21194272	52				

APPENDIX B

NMII reporter mice 13-15 days +/- Cre transfection comparison (3 mice per color in each graph and average granule integration rates listed in bottom left and color coded).

1. **mT/mGFP$^{+/-Cre}$**

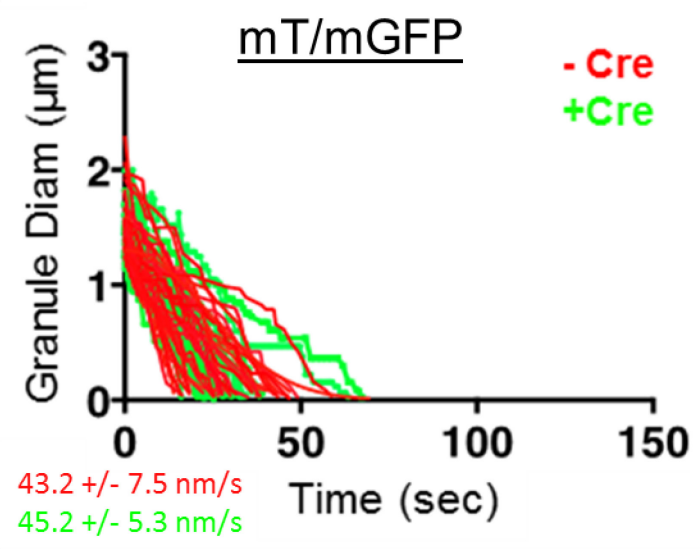

2. **NMIIA/IIB$^{mT/mGFPfl/fl+/-Cre}$**

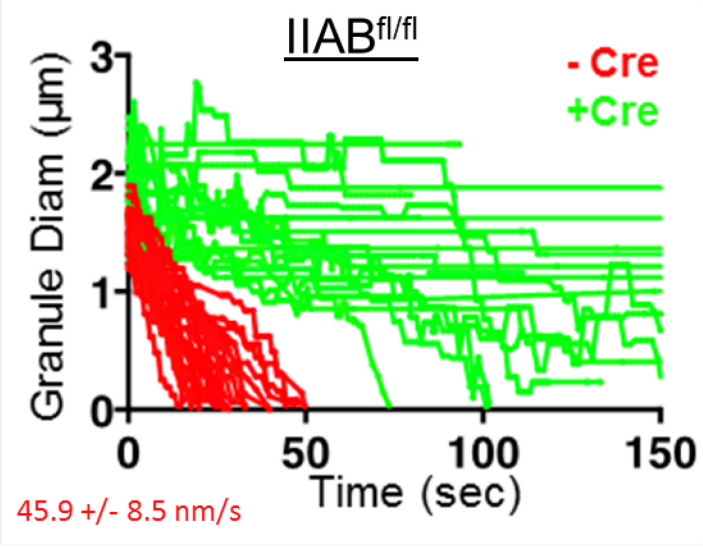

3. **NMIIA$^{mT/mGFPfl/fl+/-Cre}$**

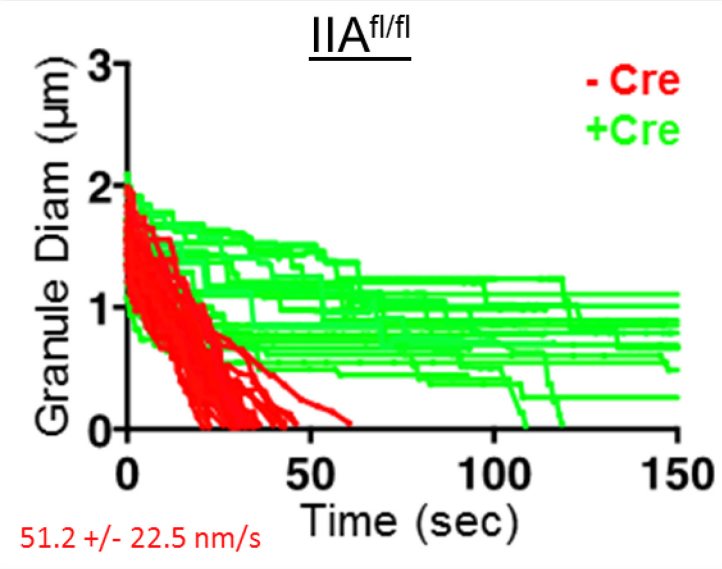

4. **NMIIB$^{mT/mGFPfl/fl+/-Cre}$**

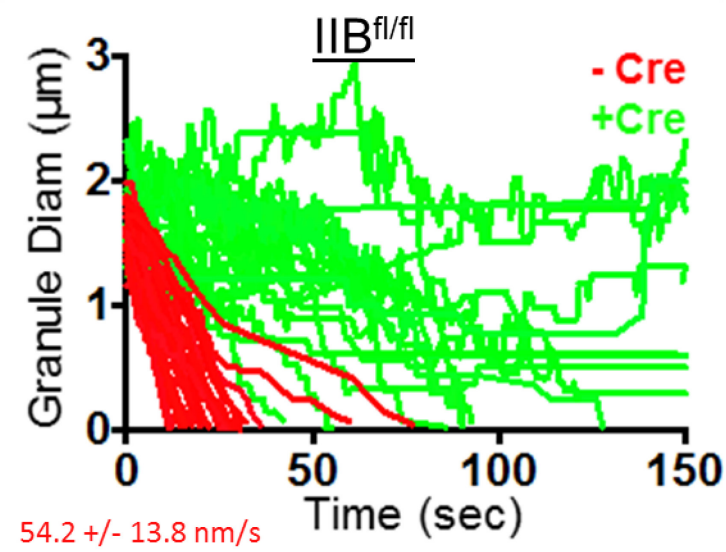

5. **Granule diameters over time for each reporter mouse fitted to the sum of two normal distributions**

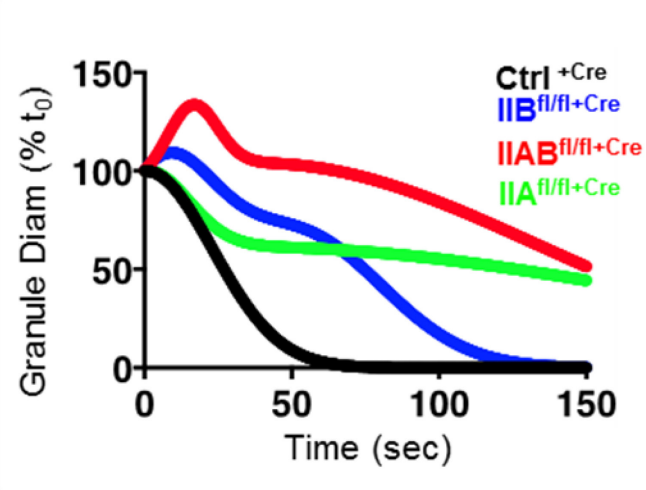

6. **Maximum granule diameters measured for each reporter mouse (statistical significance indicated by the asterisks, showing that NMIIB is necessary to stabilize the granules from expanding)**

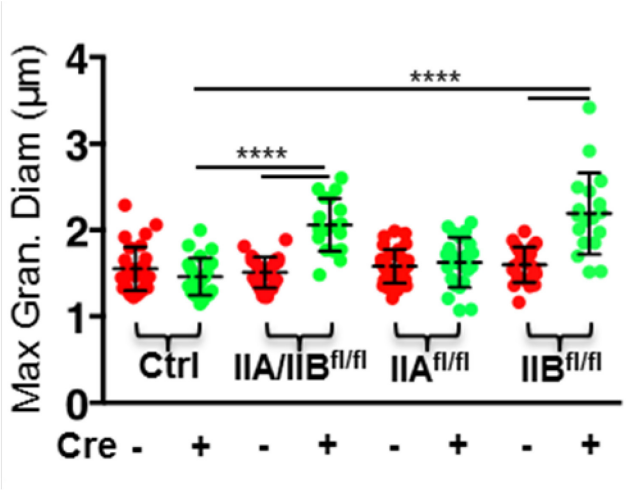

REFERENCES

1. Bohdanowicz, M. and S. Grinstein, *Role of phospholipids in endocytosis, phagocytosis, and macropinocytosis.* Physiol. Rev., 2013. **93**(1): p. 69-106.
2. Dawson, J.C., J.A. Legg, and L.M. Machesky, *Bar domain proteins: a role in tubulation, scission and actin assembly in clathrin-mediated endocytosis.* TRENDS in Cell Biology, 2006. **16**(10): p. 493–498.
3. McMahon, H.T. and E. Boucrot, *Molecular mechanism and physiological functions of clathrin-mediated endocytosis.* Nature Reviews Molecular Cell Biology, 2011. **12**(8): p. 517-533.
4. Daumke, O., A. Roux, and V. Haucke, *BAR domain scaffolds in dynamin-mediated membrane fission.* Cell, 2014. **156**(5): p. 882–892.
5. Mooren, O.L., B.J. Galletta, and J.A. Cooper, *Roles for actin assembly in endocytosis.* Annual Review of Biochemistry, 2012. **81**: p. 661-686.
6. Jahn, R., *Principles of exocytosis and membrane fusion.* Ann. N.Y. Acad. Sci., 2004. **1014**: p. 170–178.
7. Buccione, R., et al., *Regulation of constitutive exocytic transport by membrane receptors. A biochemical and morphometric study.* J Biol Chem., 1996. **271**(7): p. 3523–3533.
8. Porat-Shliom, N., et al., *Multiple roles for the actin cytoskeleton during regulated exocytosis.* Cell Mol Life Sci., 2013. **70**(12): p. 2099–2121.
9. Tsai, C.-H., et al., *Small GTPase Rab37 targets tissue inhibitor of metalloproteinase 1 for exocytosis and thus suppresses tumor metastasis.* Nature Communications, 2014. **5**(4804): p. 1-15.
10. Sollner, T.H., *Regulated exocytosis and SNARE function (Review).* Molecular Membrane Biology, 2003. **20**(3): p. 209 - 220.
11. Reddy, A., E.V. Caler, and N.W. Andrews, *Plasma membrane repair is mediated by Ca(2+)-regulated exocytosis of lysosomes.* Cell, 2001. **106**(2): p. 157–169.
12. Zhao, Y.F., et al., *Long-term inhibition of protein tyrosine kinase impairs electrophysiologic activity and a rapid component of exocytosis in pancreatic B-cells.* J Mol Endocrinol., 2005. **35**(1): p. 49–59.
13. Masedunskas, A., et al., *Role for the actomyosin complex in regulated exocytosis revealed by intravital microscopy.* PNAS, 2011. **108**(33): p. 13552–13557.
14. Catterall, W.A., *Voltage-gated calcium channels.* Cold Spring Harbor Perspectives in Biology, 2011. **7**(7): p. 1-23.
15. Seino, S. and T. Shibasaki, *PKA-dependent and PKA-independent pathways for cAMP- regulated exocytosis.* Physiol Rev., 2005. **85**(4): p. 1303-42.
16. Quissell, D.O., K.A. Barzen, and L.M. Deisher, *Role of cyclic AMP-dependent protein kinase activation in regulating rat submandibular mucin secretion.* Biochim Biophys Acta., 1983. **762**(2): p. 215-20.
17. Stojilkovic, S.S., *Ca (2+)-regulated exocytosis and SNARE function.* TRENDS in Endocrinology and Metabolism, 2005. **16**(3).
18. Pickett, J.A. and M.J. Edwardson, *Compound Exocytosis: mechanisms and functional significance.* Traffic, 2006. **7**(2): p. 109–116.

19. Harata, N.C., A.M. Aravanis, and R.W. Tsien, *Kiss-and-run and full-collapse fusion as modes of exo-endocytosis in neurosecretion.* Journal of Neurochemistry, 2006. **97**(6): p. 1546–1570.
20. Cabeza, J.M., J. Acosta, and E. Alés, *Mechanisms of granule membrane recapture following exocytosis in intact mast cells.* J Biol Chem., 2013. **288**(28): p. 20293-305.
21. Chiang, H.-C., et al., *Post-fusion structural changes and their roles in exocytosis and endocytosis of dense-core vesicles.* Nature communications, 2014. **5**.
22. Hsu, S.-C., et al., *The exocyst complex in polarized exocytosis.* International Review of Cytology, 2004. **233**: p. 243-265.
23. He, B. and W. Guo, *The exocyst complex in polarized exocytosis.* Curr Opin Cell Biol., 2009. **21**(4): p. 537–542.
24. James, D.J. and T.F.J. Martin, *CAPS and Munc13: CATCHRs that SNARE Vesicles.* Front Endocrinol (Lausanne). 2013. **4**: p. 1-11.
25. Flanagan, J.J., I. Mukherjee, and C. Barlowe, *Examination of Sec22 homodimer formation and role in SNARE-dependent membrane fusion.* J Biol Chem., 2015. **290**(17): p. 10657- 66.
26. Breidenbach, M.A. and A.T. Brunger, *New insights into clostridial neurotoxin–SNARE interactions.* TRENDS in Molecular Medicine, 2005. **11**(8): p. 377–381.
27. Hickey, C.M. and W. Wickner, *HOPS initiates vacuole docking by tethering membranes before trans-SNARE complex assembly.* Mol Biol Cell., 2010. **21**(13): p. 2297–2305.
28. Hong, W. and S. Lev, *Tethering the assembly of SNARE complexes.* TRENDS in Cell Biology, 2014. **24**(1): p. 35-43.
29. Rathorea, S.S., et al., *Syntaxin N-terminal peptide motif is an initiation factor for the assembly of the SNARE–Sec1/Munc18 membrane fusion complex.* PNAS, 2010. **107**(52): p. 22399–22406.
30. Bar-On, D., et al., *Imaging the assembly and disassembly kinetics of cis-SNARE complexes on native plasma membranes.* FEBS Letters, 2008. **582**(27): p. 3563–3568.
31. Rizo, J. and T.C. Südhof, *Snares and munc18 in synaptic vesicle fusion.* Nat Rev Neurosci., 2002. **3**(8): p. 641-653.
32. Lai, Y., et al., *Fusion pore formation and expansion induced by Ca2+ and synaptotagmin 1.* PNAS, 2013. **110**(4): p. 1333–1338.
33. Vardjan, N., et al., *Subnanometer fusion pores in spontaneous exocytosis of peptidergic vesicles.* The Journal of Neuroscience, 2007. **27**(17): p. 4737– 4746.
34. Monck, J.R. and J.M. Fernandez, *The Exocytotic Fusion Pore.* J Cell Biol., 1992. **119**(6): p. 1395-1404.
35. Vardjan, N., et al., *Elementary properties of spontaneous fusion of peptidergic vesicles: fusion pore gating.* J Physiol., 2007. **585**(Pt 3): p. 655–661.
36. Alexandr Chanturiya, L.V.C., and Joshua Zimmerberg, *Flickering fusion pores comparable with initial exocytotic pores occur in protein-free phospholipid bilayers.* PNAS, 1997. **94**(26): p. 14423–14428.
37. Dietl, P. and T. Haller, *Persistent fusion pores but transient fusion in alveolar type II cells.* Cell Biol Int., 2000. **24**(11): p. 803-7.

38. Chanturiya, A., L.V. Chernomordik, and J. Zimmerberg, *Flickering fusion pores comparable with initial exocytotic pores occur in protein-free phospholipid bilayers.* PNAS, 1997. **94**(26): p. 14423-14428.
39. Gonzalez-Jamett, A.M., et al., *Dynamin-2 regulates fusion pore expansion and quantal release through a mechanism that involves actin dynamics in neuroendocrine chromaffin cells.* PLoS One, 2013. **8**(8): p. e70638.
40. Bhat, P. and P. Thorn, *Myosin 2 Maintains an open exocytic fusion pore in secretory epithelial cells.* Mol Biol Cell., 2009. **20**(6): p. 1795–1803.
41. Doreian, B.W., T.G. Fulop, and C.B. Smith, *Myosin II activation and actin reorganization regulate the mode of quantal exocytosis in mouse adrenal chromaffin cells.* J Neurosci., 2008. **28**(17): p. 4470-8.
42. Ñeco, P., et al., *Myosin II Contributes to Fusion Pore Expansion during Exocytosis.* J Biol Chem., 2008. **289**(16): p. 10949 –10957.
43. Aoki, R., et al., *Duration of fusion pore opening and the amount of hormone released are regulated by myosin II during kiss-and-run exocytosis.* Biochem J., 2010. **429**(3): p. 497- 504.
44. Berberian K, et al., *F-Actin and Myosin II Accelerate Catecholamine Release from Chromaffin Granules.* J Neurosci., 2009. **29**(3): p. 863-870.
45. Torregrosa-Hetland, C.J., et al., *Association of SNAREs and calcium channels with the borders of cytoskeletal cages organizes the secretory machinery in chromaffin cells.* Cell Mol Neurobiol., 2010. **30**(8): p. 1315-9.
46. Burgoyne, R.D. and G.A.d. Toledo, *Fusion proteins and fusion pores.* EMBO Rep., 2000. **1**(4): p. 304–307.
47. Jahn, R. and R.H. Scheller, *SNAREs--engines for membrane fusion.* Nat Rev Mol Cell Biol., 2006. **7**(9): p. 631-643.
48. Ngatchou, A.N., et al., *Role of the synaptobrevin C terminus in fusion pore formation.* PNAS, 2010. **107**(43): p. 18463–18468.
49. Masedunskas, A., N. Porat-Shliom, and R. Weigert, *Regulated Exocytosis: Novel insights from intravital microscopy.* Traffic, 2012. **13**(5): p. 627-634.
50. Chen, Y.A. and R.H. Scheller, *SNARE-mediated membrane fusion.* Nat Rev Mol Cell Biol., 2001. **2**(2): p. 98-106.
51. Gundelfinger, E.D., M.M. Kessels, and B. Qualmann, *Temporal and spatial coordination of exocytosis and endocytosis.* Nat Rev Mol Cell Biol., 2003. **4**(2): p. 127-39.
52. Kumari, S., S. MG, and S. Mayor, *Endocytosis unplugged: multiple ways to enter the cell.* Cell Res., 2010. **20**(3): p. 256-275.
53. Masedunskas, A., M. Sramkova, and R. Weigert, *Homeostasis of the apical plasma membrane during regulated exocytosis in the salivary glands of live rodents.* Bioarchitecture, 2011. **1**(5): p. 225-229.
54. Sramkova, M., et al., *Expression of plasmid DNA in the salivary gland epithelium: novel approaches to study dynamic cellular processes in live animals.* Am J Physiol Cell Physiol., 2009. **297**(6): p. C1347-1357.
55. Yoneda, M., et al., *Changes in actin network during calcium-induced exocytosis in permeabilized GH3 cells: calcium directly regulates F-actin disassembly.* J Endocrinol., 2000. **166**(3): p. 677–687.
56. Malacombe, M., M.-F. Bader, and S. Gasman, *Exocytosis in neuroendocrine*

cells: New tasks for actin. Biochim Biophys Acta., 2006. **1763**(11): p. 1175–1183.
57. Aunis, D. and M.-F. Bader, *The cytoskeleton as a barrier to exocytosis in secretory cells.* J Exp Biol., 1988. **139**(1): p. 253-266.
58. Miklavc, P., et al., *Actin depolymerisation and crosslinking join forces with myosin II to contract actin coats on fused secretory vesicles.* J Cell Sci., 2015. **128**(6): p. 1193–1203.
59. Burgoyne, R.D. and A. Morgan, *Secretory Granule Exocytosis.* Physiol Rev., 2003. **83**(2): p. 581-632.
60. Tischler, A.S., *Chromaffin cells as models of endocrine cells and neurons.* Ann N Y Acad Sci., 2002. **971**: p. 366-370.
61. Martin, T.F. and R.N. Grishanin, *PC12 cells as a model for studies of regulated secretion in neuronal and endocrine cells.* Methods Cell Biol., 2003. **71**: p. 267-286.
62. Logan, M.R., S.O. Odemuyiwa, and R. Moqbel, *Understanding exocytosis in immune and inflammatory cells: the molecular basis of mediator secretion.* J Allergy Clin Immunol., 2003. **111**(5): p. 923-932.
63. Braun, M., et al., *Exocytotic properties of human pancreatic beta-cells.* Ann N Y Acad Sci., 2009. **1152**: p. 187-193.
64. Yamakuchi, M., et al., *Exocytosis of endothelial cells is regulated by N-ethylmaleimide- sensitive factor.* Methods Mol Biol., 2008. **440**: p. 203-215.
65. Stevens, C.F. and J.H. Williams, *''Kiss and run'' exocytosis at hippocampal synapses.* PNAS, 2000. **97**(23): p. 12828–12833.
66. Kato, A., G.J. Gores, and N.F. LaRusso, *Secretin stimulates exocytosis in isolated bile duct epithelial cells by a cyclic AMP-mediated mechanism.* J Biol Chem., 1992. **267**(22): p. 15523-9.
67. Herzog, V., H. Sies, and F. Miller, *Exocytosis in secretory cells of rat lacrimal gland. Peroxidase release from lobules and isolated cells upon cholinergic stimulation.* J Cell Biol., 1976. **70**(3): p. 692–706.
68. Wu, K., et al., *Molecular mechanisms of lacrimal acinar secretory vesicle exocytosis.* Exp Eye Res., 2006. **83**(1): p. 84-96.
69. Arvan, P. and D.J. Castle, *Phasic release of newly synthesized secretory proteins in the unstimulated rat exocrine pancreas.* J Cell Biol., 1987. **104**(2): p. 243-252.
70. Castle, D.J., *Sorting and secretory pathways in exocrine cells.* American Journal of Respiratory Cell and Molecular Biology, 1990. **2**(2): p. 119-126.
71. Girard, L.R., et al., *Characterization of common salivary protein 1, a product of rat submandibular, sublingual, and parotid glands.* J Cell Biol., 1993. **268**(35): p. 26692- 26601.
72. Skala, M. and N. Ramanujam, *Multiphoton redox ratio imaging for metabolic monitoring in vivo.* Advanced Protocols in Oxidative Stress II, Methods in Molecular Biology, 2010. **594**: p. 155-162.
73. Nemoto, T., et al., *Sequential-replenishment mechanism of exocytosis in pancreatic acini.* Nat Cell Biol., 2001. **3**(3): p. 253-258.
74. Castle, A.M., A.Y. Huang, and D.J. Castle, *The minor regulated pathway, a rapid component of salivary secretion, may provide docking/fusion sites for granule exocytosis at the apical surface of acinar cells.* J Cell Sci., 2002. **115**(Pt 14): p. 2963-73.

75. Proctor, G.B., *Muscarinic receptors and salivary secretion.* J Appl Physiol (1985). 2006. **100**(4): p. 1103-4.
76. Proctor, G.B. and G.H. Carpenter, *Regulation of salivary gland function by autonomic nerves* Auton Neurosci., 2007. **133**(1): p. 3-18.
77. Tobin, G., D. Giglio, and B. Götrick, *Studies of muscarinic receptor subtypes in salivary gland function in anaesthetized rats.* Auton Neurosci., 2002. **100**(1-2): p. 1-9.
78. Holsinger, C.F. and D.T. Bui, *Anatomy, function, and evaluation of the salivary glands.* Salivary Gland Disorders, Springer, 2007: p. 1-16.
79. Proctor, G.B., et al., *Constitutive secretion of immunoglobulin A and other proteins into lumina of unstimulated submandibular glands in anaesthetised rats.* Exp Physiol., 2003. **88**(1): p. 7-12.
80. Garrett, J.R., et al., *Secretory responses in granular ducts and acini of submandibular glands in vivo to parasympathetic or sympathetic nerve stimulation in rats.* Cell Tissue Res., 1991. **264**(1): p. 117-126.
81. Matsuo, R., et al., *Reflex secretion of proteins into submandibular saliva in conscious rats, before and after preganglionic sympathectomy.* J Physiol., 2000. **527**(Pt 1): p. 175- 184.
82. Fleming, N., L. Mellow, and D. Bhullar, *Regulation of the cAMP signal transduction pathway by protein kinase C in rat submandibular cells.* Pflugers Arch., 1992. **421**(1): p. 82-89.
83. Mills, C.L., et al., *Beta-adrenergic mobilization of Ca2+ from an intracellular store in rat submandibular acini.* Biochem J., 1993. **293**(Pt 3): p. 691-695.
84. Masedunskas, A., et al., *Intravital microscopy: a practical guide on imaging intracellular structures in live animals.* Bioarchitecture, 2012. **2**(5): p. 143-157.
85. Holtmaat, A., et al., *Long-term, high-resolution imaging in the mouse neocortex through a chronic cranial window.* Nat Protoc., 2009. **4**(8): p. 1128-1144.
86. Li, J.L., et al., *Intravital multiphoton imaging of immune responses in the mouse ear skin.* Nat Protoc., 2012. **7**(2): p. 221-234.
87. Arnon, T.I., et al., *Visualization of splenic marginal zone B-cell shuttling and follicular B- cell egress.* Nature, 2013. **493**(7434): p. 684-688.
88. Gaertner, M., et al., *Toward a comprehensive interpretation of intravital microscopy images in studies of lung tissue dynamics.* J Biomed Opt., 2015. **20**(6): p. 066009.
89. Masedunskas, A., N. Porat-Shliom, and R. Weigert, *Linking differences in membrane tension with the requirement for a contractile actomyosin scaffold during exocytosis in salivary glands.* Commun Integr Biol., 2012. **5**(1): p. 84–87.
90. Sandoval, R.M. and B.A. Molitoris, *Quantifying endocytosis in vivo using intravital two- photon microscopy.* Methods Mol Biol., 2008. **440**: p. 389-402.
91. Masedunskas, A. and R. Weigert, *Intravital two-photon microscopy for studying the uptake and trafficking of fluorescently conjugated molecules in live rodents.* Traffic, 2008. **9**(10): p. 1801-1810.
92. Dunn, K.W., et al., *Functional studies of the kidney of living animals using multicolor two- photon microscopy.* Am J Physiol Cell Physiol., 2002. **283**(3): p. C905-C916.
93. Dunn, K.W., R.M. Sandoval, and B.A. Molitoris, *Intravital imaging of the kidney*

using multiparameter multiphoton microscopy. Nephron Exp Nephrol., 2003. **94**(1): p. e7-11.
94. Masedunskas, A., et al., *Intravital microscopy reveals differences in the kinetics of endocytic pathways between cell cultures and live animals.* Cells, 2012. **1**(4): p. 1121- 1132.
95. Sramkova, M., A. Masedunskas, and R. Weigert, *Plasmid DNA is internalized from the apical plasma membrane of the salivary gland epithelium in live animals.* Histochem Cell Biol., 2012. **138**(2): p. 201-213.
96. Milberg, O., et al., *Probing the role of the actin cytoskeleton during regulated exocytosis by intravital microscopy.* Methods Mol Biol., 2014. **1174**: p. 407-421.
97. Milberg, O., et al., *Intravital microscopy and its application to study regulated exocytosis in the exocrine glands of live rodents.* Exocytosis Methods, 2014. **83**: p. 147-166.
98. Masedunskas, A., et al., *Intravital microscopy to image membrane trafficking in live rats.* Methods Mol Biol., 2013. **931**: p. 153-167.
99. Cheney, R.E., M.A. Riley, and M.S. Mooseker, *Phylogenetic analysis of the myosin superfamily.* Cell Motil Cytoskeleton, 1993. **24**(4): p. 215-223.
100. Quintero, O.A., et al., *Human Myo19 is a novel myosin that associates with mitochondria.* Curr Biol., 2009. **19**(23): p. 2008-2013.
101. Sellers, J.R., *Myosins: a diverse superfamily.* Biochim Biophys Acta., 2000. **1496**(1): p. 3- 22.
102. Wells, A.L., et al., *Myosin VI is an actin-based motor that moves backwards.* Nature, 1999. **401**(6752): p. 505-508.
103. Inoue, A., et al., *Myosin IXb is a single-headed minus-end-directed processive motor.* Nat Cell Biol., 2002. **4**(4): p. 302-306.
104. Billington, N., et al., *Myosin 18A coassembles with nonmuscle myosin 2 to form mixed bipolar filaments.* Curr Biol., 2015. **25**(7): p. 942-948.
105. Xu, J.-Q., et al., *Myosin filament structure in vertebrate smooth muscle.* J Cell Biol., 1996. **134**(1): p. 53-66.
106. Korn, E.D. and I. J A Hammer, *Myosins of nonmuscle cells.* Ann. Rev. Biophys. Biophys. Chern., 1988. **17**: p. 23-45.
107. Kachur, T.M. and D.B. Pilgrim, *Myosin assembly, maintenance and degradation in muscle: role of the chaperone UNC-45 in myosin thick filament dynamics.* Int. J. Mol. Sci, 2008. **9**: p. 1863-1875.
108. Xu, J.-Q., et al., *Myosin Filament Structure in Vertebrate Smooth Muscle.* J Cell Biol., 1996. **134**(4): p. 53-66.
109. Conti, M.A. and R.S. Adelstein, *Nonmuscle myosin II moves in new directions.* J Cell Sci., 2008. **121**(1): p. 11-18.
110. Gunst, S.J. and W. Zhang, *Actin cytoskeletal dynamics in smooth muscle: a new paradigm for the regulation of smooth muscle contraction.* Am J Physiol Cell Physiol., 2008. **295**(3): p. C576–C587.
111. Billington, N., et al., *Characterization of three full-length human nonmuscle myosin II paralogs.* J Biol Chem., 2013. **288**(46): p. 33398–33410.
112. Laevsky, G. and D.A. Knecht, *Cross-linking of actin filaments by myosin II is a major contributor to cortical integrity and cell motility in restrictive*

environments. J Cell Sci., 2003. **116**(Pt 18): p. 3761-3770.
113. Pinto, I.M., et al., *Actin depolymerization drives actomyosin ring contraction during budding yeast cytokinesis.* Dev Cell., 2012. **22**(6): p. 1247-1260.
114. Heissler, S.M. and D.J. Manstein, *Nonmuscle myosin-2: mix and match.* Cell Mol Life Sci., 2013. **70**(1): p. 1-21.
115. Vicente‐Manzanares, M., et al., *Non-muscle myosin II takes centre stage in cell adhesion and migration.* Nat Rev Mol Cell Biol., 2009. **10**(11): p. 778-790.
116. Shutova, M.S., et al., *Endogenous species of mammalian nonmuscle myosin IIA and IIB include activated monomers and heteropolymers.* Curr Biol., 2014. **24**(17): p. 1958-1968.
117. Pollard, T.D., *Electron microscopy of synthetic myosin filaments.* J Cell Biol., 1975. **67**: p. 93-104.
118. Mitsuhashi, M., et al., *Dynamic assembly properties of nonmuscle myosin II isoforms revealed by combination of fluorescence correlation spectroscopy and fluorescence cross-correlation spectroscopy.* J Biochem., 2011. **149**(3): p. 253-263.
119. Beach, J.R. and T.T. Egelhoff, *Myosin II recruitment during cytokinesis independent of centralspindlin-mediated phosphorylation.* J Biol Chem., 2009. **284**(40): p. 27377-27383.
120. Marini, M., et al., *Non-muscle myosin heavy chain IIA and IIB interact and co-localize in living cells: relevance for MYH9-related disease.* Int J Mol Med., 2006. **17**(5): p. 729-736.
121. Togo, T. and R.A. Steinhardt, *Nonmuscle myosin IIA and IIB have distinct functions in the exocytosis-dependent process of cell membrane repair.* Mol Biol Cell., 2004. **15**(2): p. 688-695.
122. Wang, F., et al., *Kinetic Mechanism of Non-muscle Myosin IIB.* J Biol Chem., 2003. **278**(30): p. 27439-27448.
123. Arora, S., et al., *Role of Nonmuscle Myosin II in Migration of Wharton's Jelly-derived Mesenchymal Stem Cells.* Stem Cells Dev., 2015. **00**(00): p. 1-13.
124. Betapudi, V., *Life without double-headed non-muscle myosin II motor proteins.* Front. Chem., 2014. **2**.
125. Houdusse, A. and H.L. Sweeney, *Myosin motors: missing structures and hidden springs.*Curr Opin Struct Biol., 2001. **11**(2): p. 182–194.
126. Kovács, M., et al., *Load-dependent mechanism of nonmuscle myosin 2.* PNAS, 2007. **104**(24): p. 9994–9999.
127. Kovács, M. and A. Málnási-Csizmadia, *Biophysical Approaches to Understanding the Action of Myosin as a Molecular Machine.* Molecular Biophysics for the Life Sciences, 2013. **6**: p. 341-361.
128. Nagy, A., et al., *Kinetic characterization of nonmuscle myosin IIB at the signle moecule level.* J Biol Chem., 2013. **288**(1): p. 709–722.
129. Cruz, E.M.D.L. and E.M. Ostap, *Kinetic and equilibrium analysis of the myosin ATPase.* Methods Enzymol., 2009. **455**: p. 157-192.
130. Dharan, N. and O. Farago, *Duty-ratio of cooperative molecular motors.* Phys. Rev., 2012. **85**.
131. Tyska, M.J. and D.M. Warshaw, *The Myosin Power Stroke.* Cell Motility and the Cytoskeleton, 2002. **51**: p. 1-15.

132. Norstrom, M.F., P.A. Smithback, and R.S. Rock, *Unconventional processive mechanics of non-muscle myosin IIB.* J Biol Chem., 2010. **285**(34): p. 26326-26334.
133. Kovács, M., et al., *Functional divergence of human cytoplasmic myosin II: Kinetic characterization of the non-muscle IIA isoform.* J Biol Chem., 2003. **278**(40): p. 38132-38140.
134. Troys, M.V., J. Vandekerckhove, and C. Ampe, *Structural modules in actin-binding proteins: towards a new classification.* Biochem Biophys Acta., 1999. **1448**(3): p. 323-348.
135. Dos-Remedios, C.G., et al., *Actin binding proteins: Regulation of cytoskeletal microfilaments.* Physiol Rev., 2003. **83**: p. 433–473.
136. Dominguez, R. and K.C. Holmes, *Actin structure and function.* Annu. Rev. Biophys., 2011.
40: p. 169-186.
137. Fujii, T., et al., *Direct visualization of secondary structures of F-actin by electron cryomicroscopy.* Nature, 2010. **467**: p. 724-729.
138. Holmes, K.C., *Actin in a twist.* Nature, 2009. **457**: p. 389-390.
139. Wanger, M., et al., *The actin treadmill.* Can J Biochem Cell Biol., 1985. **63**(6): p. 414-421.
140. Bugyi, B. and M.-F. Carlier, *Control of Actin Filament Treadmilling in Cell Motility.* Annu Rev Biophys., 2010. **39**: p. 449-470.
141. Mavrakis, M., et al., *Septins promote F-actin ring formation by crosslinking actin filaments into curved bundles.* Nat Cell Biol., 2014. **16**(4): p. 322-334.
142. Semenova, I., et al., *Actin dynamics is essential for myosin-based transport of membrane organelles.* Curr Biol., 2009. **18**(20): p. 1581–1586.
143. Vassilopoulos, S., et al., *Actin scaffolding by clathrin heavy chain is required for skeletal muscle sarcomere organization.* J Cell Biol., 2014. **205**(3): p. 377-393.
144. Mogilner, A. and G. Oster, *Force Generation by Actin Polymerization II: The Elastic Ratchet and Tethered Filaments.* Biophys J., 2003. **84**(3): p. 1591–1605.
145. Goley, E.D. and M.D. Welch, *The ARP2/3 complex: an actin nucleator comes of age.* Nat Rev Mol Cell Biol., 2006. **7**(10): p. 713-726.
146. Moore, P.B., H.E. Huxley, and D.J. DeRosier, *Three-dimensional reconstruction of F-actin, thin filaments and decorated thin filaments.* J Mol Biol., 1970. **50**(2): p. 279-295.
147. Mooseker, M.S. and L.G. Tilney, *Organization of an actin filament-membrane complex. Filament polarity and membrane attachment in the microvilli of intestinal epithelial cells.* J Cell Biol., 1975. **67**(3): p. 725-743.
148. Begg, D.A., R. Rodewald, and L.I. Rebhun, *The visualization of actin filament polarity in thin sections. Evidence for the uniform polarity of membrane-associated filaments.* J Cell Biol., 1978. **79**(3): p. 846-852.
149. Monck, J.R. and J.M. Fernandez, *The exocytic fusion pore.* J Cell Biol., 1992. **119**(6): p. 1395-1404.
150. Nanavati, C., et al., *The exocytotic fusion pore modeled as a lipidic pore.* Biophys J., 1992. **63**(4): p. 1118–1132.
151. Shi, L., et al., *SNARE proteins: one to fuse and three to keep the nascent fusion pore open.* Science, 2012. **335**(6074): p. 1355-1359.

152. Vardjan, N., J. Jorgačevski, and R. Zorec, *Fusion pores, SNAREs, and exocytosis.* Neuroscientist, 2013. **19**(2): p. 160–174.
153. Larina, O., et al., *Dynamic Regulation of the Large Exocytotic Fusion Pore in Pancreatic Acinar Cells.* Mol Biol Cell., 2007. **18**(9): p. 3502–3511.
154. Thurmond, D.C., et al., *Glucose-stimulated insulin secretion is coupled to the interaction of actin with the t-SNARE (target membrane soluble N-ethylmaleimide-sensitive factor attachment protein receptor protein) complex.* Mol. Endocrinol., 2013. **17**(4): p. 732-742.
155. Jewell, J.L., et al., *Filamentous actin regulates insulin exocytosis through direct interaction with Syntaxin 4.* J Biol Chem., 2008. **283**(16): p. 10716-10726.
156. Rondas, D., et al., *Novel mechanistic link between focal adhesion remodeling and glucose-stimulated insulin secretion.* J Biol Chem., 2011. **287**(4): p. 2423-2436.
157. Kalwat, M.A., et al., *Gelsolin associates with the N terminus of syntaxin 4 to regulate insulin granule exocytosis.* Mol Endocrinol., 2012. **26**(1): p. 128-141.
158. Nevins, A.K. and D.C. Thurmond, *A direct interaction between Cdc42 and vesicle- associated membrane protein 2 regulates SNARE-dependent insulin exocytosis.* J Biol Chem., 2005. **280**(3): p. 1944-1952.
159. Berberian, K., et al., *F-actin and myosin II accelerate catecholamine release from chromaffin granules.* J Neurosci., 2009. **29**(3): p. 863-870.
160. Ohyama, A., Y. Komiya, and M. Igarashi, *Globular tail of myosin-V is bound to vamp/synaptobrevin.* Biochem Biophys Res Commun., 2001. **280**(4): p. 988-991.
161. Wang, A., et al., *Nonmuscle myosin II isoform and domain specificity during early mouse development.* PNAS, 2010. **107**(33): p. 14645-14650.
162. Brawley, C.M. and R.S. Rock, *Unconventional myosin traffic in cells reveals a selective actin cytoskeleton.* PNAS, 2009. **106**(24): p. 9685–9690.
163. Joo, E., M.C. Surka, and W.S. Trimble, *Mammalian SEPT2 is required for scaffolding nonmuscle myosin II and its kinases.* Dev Cell., 2007. **13**(5): p. 677-690.
164. Fang, X., et al., *Biphasic targeting and cleavage furrow ingression directed by the tail of a myosin II.* J Cell Biol., 2010. **191**(7): p. 1333-1350.
165. Yamashiro, S., et al., *Citron kinase, a Rho-dependent kinase, induces di-phosphorylation of regulatory light chain of myosin II.* Mol Biol Cell., 2003. **14**(5): p. 1745-1756.
166. Sadian Y, et al., C.G., *The role of Cdc42 and Gic1 in the regulation of septin filament formation and dissociation.* Elife, 2013. **2:e01085**: p. 1-26.
167. Weirich, C.S., J.P. Erzberger, and Y. Barral, *The septin family of GTPases: architecture and dynamics.* Nat Rev Mol Cell Biol., 2008. **9**(6): p. 478-489.
168. Weems, A.D., et al., *Higher-order Septin assembly is driven by GTP-promoted conformational changes: Evidence from unbiased mutational analysis in Saccharomyces cerevisiae.* Genetics, 2014. **196**(3): p. 711-727.
169. Gladfelter, A.S., et al., *Septin ring assembly involves cycles of GTP loading and hydrolysis by Cdc42p.* J Cell Biol., 2002. **156**(2): p. 315–326.
170. Bridges, A.A. and A.S. Gladfelter, *Septin Form and Function at the Cell Cortex.* J Biol Chem., 2015. **290**(28): p. 17173-17180.
171. Zent, E. and A. Wittinghofer, *Human septin isoforms and the GDP-GTP cycle.* Biol Chem., 2014. **395**(2): p. 169-180.

172. Howard, J. and A.A. Hyman, *Dynamics and mechanics of the microtubule plus end.* Nature, 2003. **422**(6933): p. 753-758.
173. Gardner, M.K., et al., *Microtubule Assembly Dynamics: New Insights at the Nanoscale.* Curr Opin Cell Biol., 2008. **20**(1): p. 64-70.
174. Blanchoin, L., et al., *Actin dynamics, architecture, and mechanics in cell motility.* Physiol Rev., 2014. **94**(1): p. 235–263.
175. Krause, M. and A. Gautreau, *Steering cell migration: lamellipodium dynamics and the regulation of directional persistence.* Nat Rev Mol Cell Biol., 2014. **15**(9): p. 577-590.
176. Mostowy, S. and P. Cossart, *Septins: the fourth component of the cytoskeleton.* Nat Rev Mol Cell Biol., 2012. **13**(3): p. 183-194.
177. Joo, E., M.C. Surka, and W.S. Trimble, *Mammalian SEPT2 Is Required for Scaffolding Nonmuscle Myosin II and Its Kinases.* Dev Cell, 2007. **13**(5): p. 677-690.
178. Shindo, A. and J.B. Wallingford, *PCP and septins compartmentalize cortical actomyosin to direct collective cell movement.* Science, 2014. **343**(6171): p. 649–652.
179. Schneider, C., et al., *Septin rings act as a template for myosin higher-order structures and inhibit redundant polarity establishment.* J Cell Sci., 2013. **126**(Pt 15): p. 3390-3400.
180. Kengyel, A., et al., *Nonmuscle myosin IIA with a GFP fused to the N-terminus of the regulatory light chain is regulated normally.* J Muscle Res Cell Motil., 2010. **31**(3): p. 163- 170.
181. Ingaramo, M., et al., *Two-photon excitation improves multifocal structured illumination microscopy in thick scattering tissue.* PNAS, 2014. **111**(14): p. 5254–5259.
182. Muzumdar, M.D., et al., *A global double-fluorescent Cre reporter mouse.* Genesis, 2007. **45**(9): p. 593-605.
183. Riedl, J., et al., *Lifeact: a versatile marker to visualize F-actin.* Nat Methods, 2008. **5**(7): p. 605-607.
184. Riedl, J., et al., *Lifeact mice for studying F-actin dynamics.* Nat Methods, 2010. **7**(3): p. 168-169.
185. Ma, X., et al., *Conditional Ablation of Nonmuscle Myosin II-B Delineates Heart Defects in Adult Mice.* Circ Res., 2010. **105**(11): p. 1102–1109.
186. Crish, J., et al., *Keratin 5-Cre-driven excision of nonmuscle myosin IIA in early embryo trophectoderm leads to placenta defects and embryonic lethality.* Dev Biol., 2013. **382**(1): p. 136–148.
187. Jacobelli, J., et al., *Confinement-optimized three-dimensional T cell amoeboid motility is modulated via myosin IIA–regulated adhesions.* Nat Immunol., 2010. **11**(10): p. 953–961.
188. Sramkova, M., et al., *Polyethylenimine-mediated expression of transgenes in the acinar cells of rats salivary glands in vivo.* Front Cell Dev Biol., 2014. **2**: p. 1-8.
189. Liang, X., et al., *Single step BP/LR combined Gateway reactions.* Biotechniques, 2013. **55**(5): p. 265-268.
190. Marzesco, A.M. and A. Zahraoui, *Assay of Rab13 in regulating epithelial tight junction assembly.* Methods Enzymol., 2005. **403**: p. 182-193.

191. Muzumdar, M.D., et al., *A global double-fluorescent cre reporter mouse.* Genesis, 2007. **45**: p. 593-605.
192. Thévenaz, P., U.E. Ruttimann, and M. Unser, *A Pyramid Approach to Subpixel Registration Based on Intensity.* IEEE Transactions on Image Processing, 1998. **7**(1): p. 27-41.
193. Crish, J., et al., *Keratin 5-Cre-driven excision of nonmuscle myosin IIA in early embryo trophectoderm leads to placenta defects and embryonic lethality.* Dev Biol, 2013. **382**(1): p. 136-48.
194. Liu, K.C. and R.E. Cheney, *Myosins in cell junctions.* Bioarchitecture, 2012. **2**(5): p. 158- 170.
195. Bao, J., et al., *Replacement of nonmuscle myosin II-B with II-A rescues brain but not cardiac defects in mice.* J Biol Chem., 2007. **282**(30): p. 22102-22111.
196. Zhang, Y., et al., *Mouse models of MYH9-related disease: mutations in nonmuscle myosin II-A.* Blood, 2012. **119**(1): p. 238-250.
197. Chizmadzhev, Y.A., et al., *Lipid flow through fusion pores connecting membranes of different tensions.* Biophys J., 1999. **76**(6): p. 2951–2965.
198. Lorenz, M. and K.C. Holmes, *The actin-myosin interface.* PNAS, 2010. **107**(28): p. 12529– 12534.
199. Duimel-Peeters, et al., *A system review of the efficacy of topical skin application of dimethyl sulfoxide on wound healing and as an anti-inflammatory.* Wounds, 2003. **15**(11): p. 361-370.
200. Wiggan, O.N., et al., *ADF/cofilin regulates actomyosin assembly through competitive inhibition of myosin II binding to F-actin.* Dev Cell., 2012. **22**(3): p. 530-543.
201. Hatch, V., et al., *Myosin light chain kinase binding to a unique site on F-actin revealed by three-dimensional image reconstruction.* J Cell Biol., 2001. **154**(3): p. 611-617.
202. Yu, W., et al., *Synergism of protein kinase A, protein kinase C, and myosin light-chain kinase in the secretory cascade of the pancreatic beta-cell.* Diabetes, 2000. **49**(6): p. 945- 952.
203. Chen, Y., et al., *F-actin and myosin II binding domains in supervillin.* J Biol Chem., 2003. **278**(46): p. 46094-46106.
204. Kee, Y.-S., et al., *A mechanosensory system governs myosin II accumulation in dividing cells.* Mol Biol Cell., 2012. **23**(8): p. 1510-1523.
205. Sharma, S., et al., *An siRNA screen for NFAT activation identifies septins as coordinators of store-operated Ca2+ entry.* Nature, 2013. **499**(7457): p. 238-242.
206. Volceanov, L., et al., *Septins arrange F-actin-containing fibers on the Chlamydia trachomatis inclusion and are required for normal release of the inclusion by extrusion.* MBio., 2014. **5**(5): p. e01802-e01814.
207. Connolly, D., et al., *Septin 9 isoform expression, localization and epigenetic changes during human and mouse breast cancer progression.* Breast Cancer Res., 2011. **13**(4): p. R76.
208. Angelis, D., et al., *In silico docking of forchlorfenuron (FCF) to septins suggests that FCF interferes with GTP binding.* PLoS One, 2014. **9**(5): p. e96390.
209. DeMay, B.S., et al., *Cellular requirements for the small molecule forchlorfenuron to stabilize the septin cytoskeleton.* Cytoskeleton (Hoboken), 2010. **67**(6): p. 383-

399.
210. Hu, Q., J.W. Nelson, and E.T. Spiliotis, *Forchlorfenuron alters mammalian septin assembly, organization, and dynamics.* J Biol Chem., 2008. **283**(43): p. 29563-29571.
211. Kinoshita, M., et al., *Self- and Actin-Templated Assembly of Mammalian Septins.* Dev Cell., 2002. **3**(6): p. 791-802.
212. Carvalho, A., A. Desai, and K. Oegema, *Structural memory in the contractile ring makes the duration of cytokinesis independent of cell size.* Cell, 2009. **137**(5): p. 926-937.